Monitoring Cell and Tissue Damage During Ablation by High-Intensity Focussed Ultrasound

Sacha D. Nandlall

St. Anne's College

University of Oxford

A thesis submitted to the Department of Engineering Science for the degree of *Doctor of Philosophy*.

24 August 2011

To my family, who are my dearest friends;

and to those friends as dear to me as family.

Abstract

High Intensity Focussed Ultrasound (HIFU) ablation is a promising technology for the non-invasive, targeted treatment of certain types of cancer. The technique functions by subjecting tumours to a cytotoxic level of intense, localised heating, while leaving the surrounding tissue unharmed. However, a number of limitations in the available HIFU treatment monitoring methods are currently hampering the effectiveness and clinical adoption of the therapy.

This work aims to develop improved metrics of HIFU-induced biological damage that are specifically suited to monitoring and controlling HIFU ablation. Firstly, an optical method that enables straightforward quantification of thermal damage in protein-embedding hydrogels is developed. Secondly, hydrogels embedded with different cell lines are used to assess the performance of common temperature-based metrics of cell death across a range of HIFU-relevant conditions. Finally, a novel, passive acoustic detector designed for the real-time monitoring of HIFU-induced tissue damage is proposed. The detector is shown to predict lesioning with over 80% accuracy in regimes that are very likely to create lesions (60 J of acoustic energy or more), with an error rate of less than 6% for exposures that are too short to cause lesioning (up to 1 s long). The proposed detector could therefore provide a low-cost means of effectively monitoring clinical HIFU treatments passively and in real time.

Summary

High Intensity Focussed Ultrasound (HIFU) ablation is a promising technology for the non-invasive, targeted treatment of certain types of cancer. The technique functions by subjecting tumours to a cytotoxic level of intense, localised heating, while leaving the surrounding tissue unharmed. However, a number of limitations in the available HIFU treatment monitoring methods are currently hampering the effectiveness and clinical adoption of the therapy.

This work aims to develop improved metrics of HIFU-induced biological damage that are specifically suited to monitoring and controlling HIFU ablation. An optical method that enables straightforward quantification of thermal damage in protein-embedding hydrogels is first developed. The optical metric of damage is shown to be biologically relevant by comparing its value to the damage sustained by cancer cells across a range of temperature profiles. However, even in this simple biological model, the amount of protein damage is found to be dependent on the maximum temperature reached as well as the rate of heating.

The previous finding implies that the reaction kinetics describing heat-induced damage can change depending on the temperature. This motivates a more detailed performance assessment of the available models for quantifying heat-induced cell death, many of which are thermometry-based but have only been verified for mild hyperthermia (i.e. temperatures up to approximately 54 °C). Using hydrogels embedded with different cell lines, the performance of the most widely used model of heat-induced cell death—Cumulative Equivalent Minutes at 43 °C ($CEM_{43\,°C}$)—is assessed objectively across a range of HIFU-relevant conditions. It is shown that,

although the $CEM_{43\,°C}$ model can be made to work in a specific temperature range and for a specific cell line, the amount of cell death caused by a given temperature profile can vary across cell lines in general. Moreover, it is also demonstrated that the mechanically induced cell death neglected by the $CEM_{43\,°C}$ model can greatly undermine its accuracy in certain regimes, such as those that cause high levels of inertial cavitation.

The results just described show that damage models based solely on temperature are unable to provide a complete description of HIFU-induced damage in tissue, which can be comprised of multiple cell lines in the case of metastatic cancers. However, amongst the other available metrics of tissue damage that are independent of cell type, many require interlacing with the HIFU pulse, do not operate in real time, or rely on costly equipment. This work therefore concludes with the development of a novel, passive acoustic technique designed for monitoring HIFU-induced tissue damage in real time. Over 200 exposures were performed in freshly excised ox livers across a range of insonation durations and acoustic intensities. The results indicate that the successful formation of HIFU lesions in *ex vivo* ox liver is highly correlated with the presence of pronounced dips in the magnitude of the acoustic emissions at the HIFU focus at integer multiples of the insonation frequency. A detector based on this observation predicted lesioning with over 80% accuracy in regimes that were very likely to create lesions (60 J of acoustic energy or more), and had an error rate of less than 6% for exposures that were too short to cause lesioning (up to 1 s long). The overall sensitivity and specificity of the detector were 75.6% and 74.2%, respectively. The proposed detector could therefore provide a low-cost means of effectively monitoring clinical HIFU treatments passively and in real time.

Acknowledgments

It has been a privilege to work with Prof. Constantin-C. Coussios, whose extraordinary supervision, enlightened mentorship, and (it has to be said) incredible patience over the course of my degree have provided me with many inspiring examples to follow at the dawn of my own career. I don't think I'll ever quite be able to convey just how grateful I am to him for taking a chance on the freshly minted undergraduate I was in 2007. Thanks to the opportunity he granted me, I've learned and experienced so much since then—both professionally and personally—that 2007 almost seems like a whole lifetime ago.

Throughout my time in Oxford, I also benefitted from the guidance and mentorship of several other academics. Two I would particularly like to thank are Drs. Manish Arora and Heiko Schiffter. They, along with my supervisor, consistently demonstrated tireless energy, rigorous professionalism, heartfelt enthusiasm, as well as profound knowledge and insight. All were valuable role models to me, and I wish each of them continued success as well as many more rewarding years ahead.

Nearly all of the experimental work in this thesis has been carried out with invaluable help from others, in many cases from fields outside my own. In particular, I must thank Dr. Sebastian Vonhoff—at the time based in the Friedrich-Alexander University of Erlangen-Nuremberg—who, along with Dr. Schiffter, was a key collaborator in generating the protein structural analysis results that form the cornerstone of Chapter 4 of this work. I am very grateful as well to Dr. Miriam Bazán-Peregrino, who taught me just about everything I now know about working with cells; she was instrumental in carrying out the cell viability experiments described in Chapter 4,

and also in developing the cell phantoms employed in Chapter 5. Additionally, Steven Mo very kindly provided me with invaluable assistance—as well as an extra pair of hands—in carrying out the experiments described in Chapter 5. Finally, I performed much of the work in Chapter 6 in close collaboration with Edward Jackson, who was a final-year undergraduate in the Department of Engineering Science at the time. His patience during our challenging work with animal tissue, his impressive acuity and reasoning, as well as his overall dedication all made our productivity as a team far greater than the sum of our parts.

I would also like to thank all of my other colleagues in the Biomedical Ultrasonics and Biotherapy Laboratory, each of whom has contributed to my research in some way or another. They are also to be congratulated for putting up with my various antics around the lab, as well as providing help and advice whenever I needed it. In particular, I owe a great deal to workshop technicians James Fisk, Roger Lewis, and David Salisbury, whose services were invaluable in taking many of my experimental designs from concept to prototype.

Outside of my laboratory, I would like to thank Prof. Sir Richard Peto of Oxford's Nuffield Department of Clinical Medicine, as well as Prof. William O'Brien of the University of Illinois at Urbana-Champaign, for providing me with some of the background information used in Chapters 1 and 3 of this thesis. As well, I am indebted to my former undergraduate research project supervisors at McGill University, Prof. Henrietta Galiana and Dr. Alexis Motto. Both of them inspired me to pursue a career path in biomedical engineering, in addition to giving me my earliest lessons on the fundamentals of doing original research.

I also gratefully acknowledge the financial support I have received for my project, which has come from various organisations. These include the National Science and Engineering Research Council of Canada (NSERC), through a two-year Postgraduate Scholarship; the Engineering and Physical Sciences Research Council of the United Kingdom (EPSRC), through various grants to our laboratory; St.

Anne's College (part of the University of Oxford), through their Graduate Development Scholarship; and the Maple Leaf Trust, through their Canadian Centennial Scholarship. I am deeply honoured that each of these organisations deemed my research—and me—to be worthy of their support.

On a more personal note, I would like to thank my good friends on both sides of the Atlantic and all across the world, especially (in alphabetical order) Adam Bertrand, Miklós Gyöngy, Filip Havreljuk, Ridhi Kantelal, Victor Legros, Antoine Marcoux, Valérie Packwood-Vignet, Jean-François "Jeff" Roy, George Standen, and Azumi Watabe. During my studies in Oxford, the gift of their close friendship made the good times great, and the hard times bearable. *Merci beaucoup, mes amis, pour votre fraternité et votre chaleureuse compagnie.*

Lastly, and most emphatically of all, I would like to express the immense love and gratitude I have for my family: my mother, Valerie Ramsumeer; my father, Dennis Nandlall; and my brother, Ian Nandlall. Above all else, it is their unconditional love and unwavering support over the years that have made everything I have accomplished possible. This thesis is dedicated to them, and I hope that in some small way, it bears witness of just how much they mean to me.

Contents

Abstract iii

Summary iv

Acknowledgments vi

List of Figures xiv

List of Tables xv

1 Cancer and the Role of HIFU 1

1.1 Basics of HIFU Therapy 1

1.2 Cancer Pathology and Epidemiology 4

1.3 Cancer Treatment 6

1.4 The Potential Role of HIFU Ablation in Cancer Therapy 9

2 Biomedical Acoustics 12

2.1 Elementary Concepts and Linear Acoustic Theory 12

2.2 Nonlinear Acoustic Phenomena 32

2.3 Design and Operation of Acoustic Transducers 41

2.4 Summary 45

3 Monitoring Thermal and Mechanical Damage in Biological Media 47

3.1 General Considerations 47

3.2 Protein Denaturation 50

3.3 Cell Death 61

3.4 Tissue Necrosis 75
3.5 Objectives and Contributions of This Work 88

4 Optical Measurement of Damage in Protein-Embedding Hydrogels 93

4.1 Motivation and Objectives 94
4.2 Experimental Methods 95
4.3 Results 105
4.4 Discussion 115
4.5 Conclusions 119

5 Determination of Cytotoxic Thermal Dose During HIFU Ablation 121

5.1 Motivation and Objectives 122
5.2 Experimental Methods 123
5.3 Results and Discussion 134
5.4 Conclusions 135

6 Real-Time Passive Acoustic Monitoring of HIFU-Induced Tissue Damage 137

6.1 Motivation and Objectives 138
6.2 Experimental Methods 139
6.3 Results and Discussion 152
6.4 Conclusions 164

7 Conclusions and Future Work 166

7.1 Summary of Key Findings 166
7.2 Future Work 168

A List of Publications 172

A.1 Peer-Reviewed Journal Articles 172
A.2 Peer-Reviewed Abstracts 173

B Table of Acoustic Properties **175**

C Mathematical Definition of T_n Spatial Descriptors **176**

C.1 A Formal Definition of T_n Descriptors 176

C.2 Derivation of a Simplified Formula for T_0 178

C.3 Derivation of a Simplified Formula for T_{100} 181

C.4 T_n Descriptors of Sampled Distributions 183

References **189**

List of Figures

1.1 An illustration of solid tumour ablation using HIFU 2
1.2 A commercially available HIFU treatment system 3
1.3 The six classical hallmarks of cancer 5

2.1 Illustration of the longitudinal and transverse wave propagation modes 17
2.2 Speed of sound in pure water from 0 °C to 95 °C 25
2.3 Cavitation threshold in water as a function of initial bubble radius and frequency 37
2.4 Illustrations of the focal zone and beam profiles of focussed transducers 42

3.1 The four canonical levels of protein structure 53
3.2 Opaque "lesions" of thermally denatured proteins in BSA hydrogel 55
3.3 An illustration of the SEC method 58
3.4 Setup for FTS and its infrared version, FTIR 60
3.5 The evolution of the stiffness of bovine muscle during heating and subsequent cooling 84
3.6 Appearance of hyperechogenic regions on 2-D diagnostic ultrasound images of a cancer tumour exposed to HIFU 86

4.1 Experimental setup for measuring heat-induced changes in the opacity of BSA polyacrylamide hydrogel 102
4.2 Time-lapse photographs and corresponding greyscale intensity histograms of BSA polyacrylamide hydrogel in a 78 °C water bath 103

4.3 Optical transmittance at 350 nm of 3.5% (w/v) BSA solutions exposed to various temperatures for 30 minutes 106
4.4 SEC chromatograms for 3.5% (w/v) BSA solutions heated to 25 °C, 70 °C, and 90 °C for 30 minutes 107
4.5 Relative amount of BSA monomers and aggregates in 3.5% (w/v) BSA solutions exposed to various temperatures for 30 minutes . . . 108
4.6 Examples of FTIR spectra and second derivatives of these spectra in 2% (w/v) BSA solutions heated to 25 °C, 70 °C, and 95 °C for 30 minutes 110
4.7 Relative secondary structure distribution of BSA in 3.5% (w/v) solutions heated to various temperatures for 30 minutes 111
4.8 ZR75.1 cell viability and opacity of BSA polyacrylamide hydrogel after 1 minute of heating at various target temperatures from 37 °C to 90 °C 113
4.9 Normalised mean optical transmittance of two BSA hydrogel slices heated to 70 °C and 85 °C 114
4.10 Steady-state mean optical transmittance of the heated BSA hydrogel slices after heating to various target temperatures 114
4.11 Photographs of the BSA hydrogel slices in Figure 4.9 after heating . 115
4.12 Light transmission in BSA polyacrylamide hydrogel as a function of time and target temperature 119

5.1 Photograph of one of the holders used for casting the cell-embedding gels 124
5.2 Block diagram of the HIFU ablation monitoring setup 126
5.3 Illustration of the HIFU data acquisition protocol 132
5.4 Fluorescence intensity maps of calcein AM and propidium iodide in cell phantoms 133
5.5 Plot of objectively measured, thermally induced cell death versus $CEM_{43\,°C}$ values for different cancer cell lines 135

6.1 Photographs of the holders used in the HIFU tissue ablation experiment 140
6.2 An example of a lesion grid generated during the HIFU tissue ablation experiment 142
6.3 Examples of the correlation between the formation of lesions and the appearance of harmonic dips 144
6.4 Illustration of the operation of the harmonic dip detection algorithm 145
6.5 Scatter plot of the sensitivity and specificity of the harmonic dip detector across all 212 exposures for each parameter value combination in Table 6.1 150
6.6 Average lesion volume as a function of exposure time and exposure energy 153
6.7 Performance of the harmonic dip detector versus exposure time and exposure energy 156

List of Tables

2.1 Orders of magnitude of various acoustic parameters in this work . . 30

3.1 Summary of the efficacy of the treatment monitoring methods discussed in Chapter 3 89

5.1 Calculation of the −3 dB focal volume of the detector transducer . . 129

6.1 Parameter selection process for the harmonic dip detector 149

6.2 Performance of the harmonic dip detector across all 212 exposures for the three optimal analyses labelled in Figure 6.5 152

6.3 Performance comparison between the harmonic dip detector (*ex vivo* ox liver) and hyperecho monitoring data (*in vivo* rabbit liver) . . . 155

Chapter 1

Cancer and the Role of HIFU

This chapter introduces High-Intensity Focussed Ultrasound (HIFU) ablation and discusses its potential role in treating cancer. An overview of the HIFU ablation technique is first provided, followed by a short summary of the pathology, epidemiology, and risk factors of cancer. Existing cancer therapies such as chemotherapy, surgery, and radiotherapy are then discussed, along with the side effects associated with each treatment. Finally, this chapter examines the potential role of HIFU ablation within the set of currently available cancer therapies.

1.1 Basics of HIFU Therapy

Although ultrasound has long been employed to perform medical diagnoses, it is also now emerging as a promising, innovative technology for the non-invasive treatment of cancer [1–3]. By focussing a high-intensity beam of ultrasound, it is possible to heat an area of tissue about the size of a grain of rice at a rapid rate while leaving the surrounding tissue undamaged, as illustrated in Figure 1.1. In as little as a few seconds, the cells in the target region undergo coagulative necrosis, a type of cell

death that is caused by hypoxia (i.e. a lack of oxygen) and which can occur when blood flow to the cells is severely restricted [4, 5]. This technique, which is called thermal ablation, makes it possible for High-Intensity Focussed Ultrasound (HIFU) to destroy deep-seated, solid tumours in soft tissue, such as those in the pancreas, liver, or kidneys [1, 6–8]. HIFU therapy is currently in use throughout the world, although still in early phase clinical trials in many areas. A number of commercially produced HIFU devices are already on the market [5, 7, 9], such as the JC HIFU system shown in Figure 1.2.

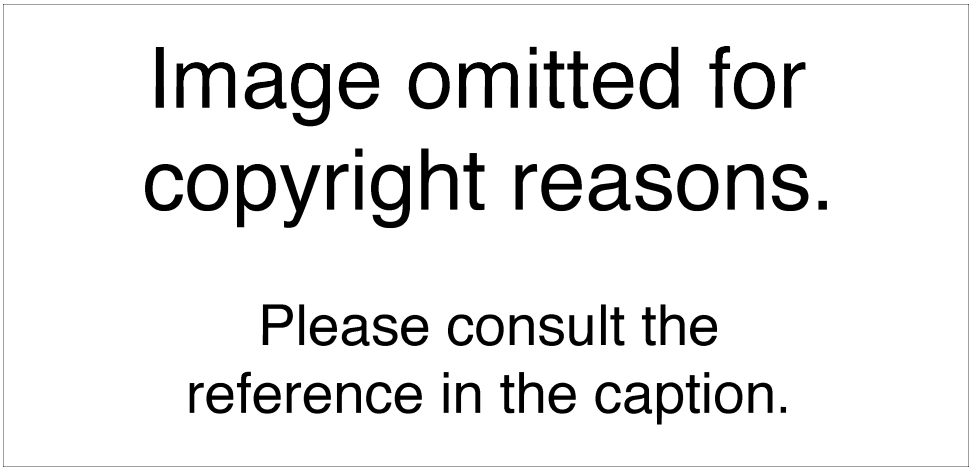

Figure 1.1: *An illustration of how High-Intensity Focussed Ultrasound (HIFU) may be used to destroy a solid cancer tumour non-invasively, in this case within the liver. Here the "transducer" indicates the source of the HIFU beam and the "ablated tumour volume" indicates the region of tissue that has been destroyed using HIFU-generated heat. Reproduced from Kennedy [1].*

As a cancer treatment, HIFU can be used either on its own or as an adjuvant to other therapeutic modalities. However, as a standalone treatment, HIFU possesses a number of advantages compared to other therapies: the equipment required to administer it is relatively inexpensive, it can be aimed with sufficient spatial resolution so as to target only malignant tissue, and it does not require invasive surgery nor entail the side effects that arise from such procedures. On the other hand, the

Figure 1.2: *The JC HIFU system, produced by the HAIFU Technology Company (Chongquing, People's Republic of China), is an example of a commercially produced therapeutic ultrasound system that finds use in operating theatres and clinical research facilities worldwide [6, 7]. The actual ultrasound-generating equipment is located beneath the hole in the patient's cot, and only occupies a relatively small portion of the machine's total footprint. Reproduced from company literature [9].*

performance and clinical adoption of HIFU therapy are currently being hindered by a number of difficulties, many of which originate with the need for effective, inexpensive treatment monitoring tools [1, 2, 10–13].

This work seeks to address some of the monitoring-related limitations of HIFU therapy and thereby improve its effectiveness as well as accelerate its clinical adoption. To begin with, the remainder of this chapter is devoted to an overview of the medical perspective, including a general description of how cancer operates, what therapies are currently available to treat it, and where the niche of HIFU therapy lies in this array of therapeutic options. Chapter 2 then describes HIFU from an engineering perspective by discussing the acoustical concepts and theory associated with ultrasound propagation in biological media. The medical and engineering per-

spectives are both featured in Chapter 3, which provides a review of the currently available techniques that have been developed to monitor HIFU therapy. Chapter 3 also clarifies the current clinical needs in this area by illustrating how the shortcomings in the available HIFU treatment monitoring techniques serve to hinder the effectiveness and clinical adoption of HIFU ablation. Finally, the solutions that this work proposes to address current shortcomings in HIFU treatment monitoring are outlined at the end of Chapter 3.

1.2 Cancer Pathology and Epidemiology

Cancer is in fact not a single disease, but rather a name for a group of diseases that share the ability to invade the body and cause uncontrolled cellular growth. These diseases also possess the ability to develop not only where they first appear (primary cancers), but also to spread throughout other regions of the body. In the latter case, the cancer is termed secondary, and is said to have undergone metastasis. It is this capability that makes cancer so dangerous: if left untreated, it can grow and spread throughout the body.

Figure 1.3 summarises the main characteristics ("hallmarks") of cancer, according to Hanahan and Weinberg [14]. In time, cancerous tissue loses its original morphology and function, with new cells growing at a faster rate than is needed to replace dying ones. In most cancers, the malignant cancerous cells eventually group together and form tumours (though this is not always the case, with leukemia being one well-known exception). The cancer may also proceed to invade other tissues, bone marrow, or the bloodstream. The end result is that the cancerous cells slowly

starve healthy tissues of the nutrients and resources they require, which eventually leads to death.

Figure 1.3: *The six classical hallmarks of cancer. Reproduced from Hanahan and Weinberg [14].*

Since modern times, and especially as average life expectancy has increased, cancer has become a leading cause of mortality worldwide. The World Health Organisation estimates that 13% of all deaths are caused by cancer, a figure that translated to 7.6 million fatalities worldwide in 2007 according to the American Cancer Society. These figures are projected to increase over the next two decades [15]. According to Cancer Research UK, in 2004 and within the UK alone, there were upwards of 7000 cases of primary kidney cancer, some 2800 cases of primary liver cancer, and more than 12 000 cases of secondary colorectal carcinoma confined to the liver. Morbidity for primary kidney cancer was more than 50%. Globally, liver cancers represented approximately 9% of all cancers in 2002, and were responsible for 598 000 deaths in

that year [16]. Pancreatic and kidney cancer accounted for respectively for 227 000 and 102 000 deaths worldwide, with the mortality rate for the former being upwards of 98%. These statistics demonstrate the pressing need for effective, low-cost cancer treatment techniques. The next section therefore describes some of the most established therapies that are currently used clinically to treat cancer.

1.3 Cancer Treatment

Progress in medical oncology has given rise to various therapies that can delay the onset of cancer, or even eradicate certain types of it. The following list describes the most common and established ones. Many of these treatments are often combined with each other for maximum effect.

Chemotherapy involves killing cells using cytotoxic chemicals. Most chemotherapy agents function by impeding cell division in some way, while others work by causing cells to undergo apoptosis, or programmed cell death. Unfortunately, most of these drugs are incapable of distinguishing between normal and cancerous cells. Research into what differentiates these two cell types is still ongoing. In general, chemotherapy drugs cause many unwanted and often severe side effects, since they also kill healthy cells and cannot be restricted to targeting only the malignant ones. For example, a common side effect of chemotherapy drugs is hair loss; this is because the cells responsible for hair growth are also fast-dividing like cancer cells are, and are thus also affected by the impeded cell division caused by the chemotherapy drug. Other organs that can be adversely affected by the inhibition of cell division include those

of the gut (the stomach, the intestines, etc.), as well as the heart, the liver, and the kidneys.

Hormonal therapy consists of manipulating the endocrine system, which is a subset of organs responsible for producing hormones, or substances that perform signalling functions outside cells. Hormonal therapy can involve administering drugs that reduce the quantity of a particular hormone or block its activity, increasing the concentration of a specific hormone in a patient, or even removing certain organs in the endocrine system via surgery. This cancer therapy finds particular use in tissues that are especially responsive to hormones even in their normal state, including the breast and the prostate.

Surgery involves excising tumours or tumour-containing organs from the patient. Surgery is an effective means of treatment for certain types of cancer, particularly those manifesting themselves as solid tumours. However, because most surgical procedures are highly invasive, surgery can require recovery times of the order of weeks, as well as cause side effects such as infection, scarring, hemorrhaging, and loss of function in the treated area. Moreover, reaching the tumour can sometimes be difficult if it lies buried within critical structures in the body.

Radiotherapy uses ionising radiation to damage cellular DNA through ionisation, which consists of removing electrons from the atoms comprising the DNA. The therapy is delivered using multiple shaped radiation beams, placed at different angles such that they intersect at the tumour and deliver a higher dose there. The therapy itself is painless, although there may be side effects

induced during the treatment or in the months and years that follow. These can include skin damage, infertility, hair loss, as well as damage to healthy tissue surrounding the tumour; furthermore, the radiation itself can also cause cancer in sufficiently high doses. These side effects, although severe in some instances, are generally predictable depending on the applied dose. Radiation dosimetry is fairly precise and establishes quantitative dose thresholds for various treatment scenarios, depending on the type of cancer involved as well as whether the therapy is intended to be curative or palliative [17].

Radiofrequency ablation uses a high-frequency electric probe to treat tissue. The probe damages the cells in its immediate area by converting the electrical energy into heat at its tip. This technique can be applied through the skin or during open surgery, and has found particular use in treating liver and kidney tumours up to 4 cm in diameter [1].

Cryoablation consists of using a special probe to damage the tissue by alternately freezing it and thawing it. The concept is similar to radiofrequency ablation, except that the probe works by forming a ball of ice at its tip, with the help of liquid nitrogen or argon gas. This induces cell death by changing the ambient pH and rupturing cellular membranes, as well as by damaging the local vasculature [4]. The areas of application of this therapy are similar to those noted for radiofrequency ablation [1].

Laser ablation involves placing needles through the skin such that the needle tips are positioned inside the cancerous tissue. Laser fibers can then be inserted

through these needles and used to heat the malignant tissue, which is again similar in concept to radiofrequency ablation.

Electroporation consists of using an externally applied electric field to increase the permeability of cell membranes. The electric field typically consists of short, high-voltage pulses that are applied via contact electrodes. The increase in cell membrane permeability is reversible if the amplitude, duration, and frequency of the pulses are kept sufficiently low; however, at higher settings, cells may become permanently damaged. Studies have demonstrated that irreversible electroporation can be used to perform focussed ablation of cancerous tissue without the need for heat or chemotherapeutic agents [18, 19].

The last five techniques in this list are generally described as minimally invasive, and are typically guided using either ultrasound or Magnetic Resonance Imaging (MRI) [1]. The next section will discuss the potential role and unique advantages of HIFU therapy in light of the therapeutic options just listed.

1.4 The Potential Role of HIFU Ablation in Cancer Therapy

As mentioned previously in Section 1.1, HIFU uses focussed, high-intensity beam of ultrasound to heat and destroy a target area of tissue in a relatively short span of time. From this perspective, it is similar in concept to radiotherapy, with one important difference: therapeutic ultrasound is not ionising radiation. Instead, as will be explained in Chapter 2, HIFU works by propagating a pressure wave through the tissue, which is then converted into heat due to absorption by the medium. By focussing the ultrasound tightly enough, the cells in the focal area will be heated to

the point of coagulative necrosis, but no lasting damage will occur outside the focal area. Hence, ultrasound therapy entails practically no side effects, with most studies reporting complications no more severe than relatively minor skin burns [6, 17, 20].

As a tumour removal method, ultrasound also shares some similarities with surgery, in that the goal is to physically destroy or remove the tumour, in the former case via thermal ablation and in the latter by direct excision. A fundamental difference between these two therapies is that in HIFU, the necrosed tissue is left *in situ*, whereas it is physically removed in the case of surgery. This confers an advantage to HIFU from an immunological standpoint, because leaving the necrosed tissue *in situ* has been shown to stimulate the immune response more than excising it [20, 21].

Finally, of all the techniques listed in the last section except for radiotherapy, HIFU is the only one that is truly non-invasive. HIFU can be used to reach tumours that are difficult or practically impossible to reach with surgery, such as those in the liver, kidney, prostate, breast, or pancreas [1, 2, 22]. The non-invasive nature of HIFU also means that it does not cause the side effects and long recovery times associated with surgery and other invasive methods.

In summary, HIFU is particularly applicable as an adjuvant to any of the therapeutic modalities listed the last section, and also as a non-invasive, virtually side effect-free treatment for deep-seated, solid tumours, particularly in cases where surgery or radiotherapy might normally be employed. This said, it would be incorrect to view HIFU therapy as a panacea, because the technique also has a number of limitations in its current form [1, 10], including several related to treatment monitoring. These limitations are particularly important because, like other ablative cancer

therapies, HIFU does not distinguish between healthy and cancerous cells, and hence effective treatment monitoring is critical to ensuring that the correct tissue is ablated. However, fully understanding the limitations of HIFU treatment monitoring as well as the possible ways of addressing them requires a deeper understanding of the science behind ultrasound therapy. To this end, the next chapter examines HIFU from an engineering perspective by discussing the acoustical concepts and theory that underlie the technique.

Chapter

2

Biomedical Acoustics

Acoustics is a cross-disciplinary field that deals with the theory and applications of sound, ultrasound, and infrasound, which are acoustic waves that lie respectively within, above, and below the frequency range of human hearing. This chapter provides an overview of those elements of acoustical theory and practice that are relevant to HIFU ablation. Basic acoustic concepts and linear acoustic theory are first discussed, followed by descriptions of nonlinear acoustical phenomena. This chapter concludes by summarising the design and operation of acoustic transducers, which are the devices used to generate and monitor acoustic waves.

2.1 Elementary Concepts and Linear Acoustic Theory

2.1.1 Acoustic Waves

Sound, ultrasound, and infrasound are all types of acoustic waves, with ultrasound being defined as any acoustic wave whose frequency content lies above the threshold of human hearing. This threshold varies between individuals, but is typically taken to be 20 kHz for the purposes of this definition [23, 24].

Acoustic waves are comprised of mechanical pressure fluctuations that propagate through a substance, which is referred to as the "medium" of the wave. During wave motion, each of the disturbed particles in the medium transmits wave energy to its neighbours through intermolecular forces or collisions; however, the displacement of the individual particles is usually small compared to the overall extent of the wave. For this reason, it is often possible to treat the medium as a continuum instead of the collection of discrete particles that it actually is. This approximation greatly simplifies the analysis of acoustic wave propagation and makes it possible to define point-wise values for quantities that would normally only be spatially averaged (for example, the mass density). A caveat of continuum analysis is that the results it produces will only make sense when the length scales of interest are large enough to render the effects of individual particles negligible; however, it will be shown later in Section 2.1.8 that this is the case for all situations of interest in this work.

The mechanical nature of acoustic waves means that matter is required to propagate them: unlike other types of waves such as electromagnetic radiation, acoustic waves cannot propagate in a vacuum. The two material properties that determine how well a given substance can support acoustic waves are its elasticity and its inertia. The former property originates from attractive forces between the particles that comprise the medium, while the latter arises from the fact that each of these particles has a nonzero mass. The manner in which these two properties combine to allow acoustic wave propagation is described succinctly by Insana and Brown [25] as follows: "*elasticity implies that any deviation from the equilibrium state of the [medium] will tend to be corrected; inertia implies that the correction will tend to*

overshoot, producing the need for a correction in the opposite direction and hence allowing for the possibility of propagating phenomena."

2.1.2 Quantifying the Elasticity and Inertia of a Medium

From a quantitative perspective, the effect of inertia can be represented by the mass density of the medium (ρ, in units of mass per unit volume). Meanwhile, the influence of elasticity can be characterised using the elastic modulus (generically denoted as E), which is defined as the amount of applied pressure (the stress) required to produce a given relative change in the length or size of the medium (the strain). Since strain is a dimensionless quantity, the elastic modulus has units of pressure. One example of a simple elastic system is a spring, in which stress is proportional to strain as per Hooke's law.

In practice, the relationship between stress and strain in most materials is complex, and often cannot be described adequately with a single, constant elastic modulus. For the purposes of this work, two real-world behaviours that can further influence the elastic response of a material are of particular interest. The first is viscosity, which arises from the fact that stress-induced deformation does not take place instantly in a real substance. This phenomenon can be thought of analogously to friction or drag, and can be characterised by the coefficient of viscosity (expressed in units of pressure multiplied by time). In elastic materials, viscosity implies that the elastic response of the material depends not just on the amount of strain, but also on the rate of strain. A simple, one-dimensional viscous system is a dashpot, in which stress is proportional to the strain rate. Substances which exhibit both vis-

cosity and elasticity are said to be viscoelastic. One way of modelling such materials is the Kelvin-Voigt scheme, which represents the material using a dashpot (the viscous component) connected in parallel with a spring (the elastic component) [26]. While this simple model of viscoelasticity suffices in many cases [27], there are also instances in which its predictions are not adequate; one such instance will be discussed in Section 2.1.7. More complex models of viscoelastic behaviour have been proposed for such situations: for example, the fractional-order parametric model employed by Kelly and McGough [28] has been found to yield better results than the Kelvin-Voigt scheme in rubbery or glassy substances [29].

The second real-world behaviour that can affect the elastic response of a substance is anisotropy, which is a consequence of the spatial asymmetry that is present in many materials. Anisotropy implies that the elastic response of a substance depends on the direction in which the stress is being applied; in the case of an acoustic wave, this corresponds to the axis along which the particles are oscillating. As will be explained shortly, anisotropic materials can be accommodated by adopting different definitions for the elastic modulus and the coefficient of viscosity, depending on the direction of wave oscillation.

In addition to being highly material-specific, the mass density, elastic modulus, and viscosity of a given substance are all influenced by local environmental conditions such as temperature. Notably, these values can also be affected by the amount of heat flow that takes place during wave propagation. From a thermodynamic perspective, if the flow of heat is completely unhindered—such that the surroundings of a given point effectively act as an infinite reservoir of heat—the temperature at

that point will remain constant, and the process is said to be isothermal. On the other hand, if no heat flow takes place, the process is said to be adiabatic; if, in addition to this, the process is thermodynamically reversible, it can be shown that no net change in entropy occurs (isentropic conditions). Real behaviour is usually somewhere in between these extremes; however, for the purposes of this work, it will be sufficient to treat the processes involved in acoustic wave propagation as adiabatic and reversible (and thus isentropic). Later in Section 2.1.8, this assumption will be justified on the grounds that the timescales of interest in this work are short enough to make this approximation reasonable.

2.1.3 Longitudinal and Transverse Waves

In general, there exist many different propagation modes by which mechanical waves can carry acoustic energy, although most substances can only support a subset of these modes. Two important propagation modes encountered in biomedical ultrasound are longitudinal and transverse waves, which are also respectively referred to as compressive waves and shear waves. Figure 2.1 illustrates waves travelling in each of these modes. In longitudinal wave propagation (Figure 2.1a), the axis of oscillation coincides with the direction of wave travel. In the case of an acoustic pressure wave, the regions in which the wave is positive experience compression, while the negative regions are said to be undergoing rarefaction. On the other hand, in transverse waves (Figure 2.1b), the axis of oscillation is perpendicular to the direction of wave travel. The points where the highest positive displacement occurs thus correspond to wave peaks, while those at which the largest negative displacement takes place are referred to as troughs.

(a) *Longitudinal wave propagation. Here, each bar can thought of as representing a single particle (or a fixed number of particles), and all particles are oscillating horizontally. Hence, regions with higher densities of bars correspond to higher pressure values.*

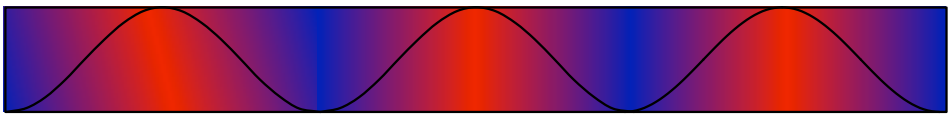

(b) *Transverse wave propagation. Here, the particles are oscillating vertically, and the pressure value is simply indicated by the height of the trace (as on a conventional xy graph).*

Figure 2.1: *Illustration of the longitudinal (compressional) and transverse (shear) wave propagation modes, pictured as "snapshots" at a single point in time. In these examples, the waves are travelling horizontally (left or right).*

In describing the propagation of longitudinal waves, the appropriate choice of elastic modulus is the bulk modulus (denoted B), while viscous effects can be quantified using the bulk viscosity (denoted η_b) [30]. The bulk modulus of a substance is defined according to the equation

$$B = \left(-V\frac{\partial p}{\partial V}\right)_{\delta s=0} = \left(-\frac{\partial p}{\partial V/V}\right)_{\delta s=0} \tag{2.1}$$

where p is the applied pressure, V is the volume over which that pressure is being applied, and the subscript $\delta s = 0$ indicates that isentropic conditions are assumed. The rightmost expression, although not technically correct notation, provides an intuitive interpretation of the bulk modulus as the change in pressure ∂p required to produce a given relative change in volume $\partial V/V$. The negative sign is present to make the overall quantity positive, since applying more pressure ($\partial p > 0$) will reduce the volume ($\partial V < 0$), and likewise decreasing the pressure will allow the

volume to increase. Sometimes, the inverse of the bulk modulus is quoted instead; this is referred to as the compressibility, and is defined as $\kappa = 1/B$.

In the case of transverse wave propagation, the elastic modulus of interest is the shear modulus (denoted G), while viscous effects can be represented using the coefficient of shear viscosity (denoted η); the latter is often simply referred to as "the viscosity" without further qualification. Shear viscosity is a property exhibited by fluids, which are substances that deform continuously (i.e. "flow") when subjected to shear stress. This definition encompasses gases (fluids that expand to fill their container) and liquids (fluids that assume the shape of their container but do not expand to fill it), but stands in contrast to many solids (most of which do not deform elastically under shear stress). Shear viscosity can be thought of as a fluid's resistance to flow, and manifests itself in everyday experience as the "thickness" of the fluid (for example, water is less viscous than oil or paint). The higher the shear viscosity of a fluid, the more capable it will be of resisting shear stress, and hence the better it will be at supporting transverse wave propagation. This is an important fact to bear in mind in the context of HIFU ablation, because the viscosity of biological tissue increases as it undergoes permanent thermal damage [31–34]. Notably, this phenomenon occurs during the cooking of protein-based foodstuffs such as meat or eggs, which stiffen as they are cooked (it will be possible to describe this process in more precise terms after Section 3.2, which discusses heat-induced damage in proteins). The correlation between the viscosity and the amount of thermally induced tissue damage can therefore be exploited to monitor HIFU ablation, in particular through shear wave elastography (discussed in Section 3.4.5, page 85).

This correlation may also be involved in a completely new monitoring technique called harmonic dip detection, which will be developed in Chapter 6.

While solid substances and fluids with a high (shear) viscosity are capable of sustaining both longitudinal and transverse waves, low-viscosity fluids such as air and water simply deform under shear stress, and hence do not support shear wave propagation over distances longer than tens of microns. Since these fluids are omnipresent in biological organisms and their living environments, all audible sound and most biomedical ultrasound waves are generated and propagated as longitudinal waves. This includes HIFU, which must propagate in water and water-based tissues. Hence, from this point forward, it will be assumed that the mode of ultrasound propagation is longitudinal, except where otherwise stated. This said, transducers that generate shear waves are also available, and under certain conditions, shear waves can even be generated using some of the energy from the main longitudinal wave.

2.1.4 The Wave Equation

The wave equation provides a first-order description of acoustic wave propagation. It may be derived from more fundamental laws, which can include conservation of mass, the thermodynamic equation of state, as well as conservation of linear momentum (typically stated as a variant of Newton's second law). A law governing conservation of energy can also be included, although in this work it is not necessary because the wave propagation process is treated as isentropic.

The wave equation is a central result in linear acoustic theory, which is predicated on one further assumption in addition to those already mentioned. In linear acoustic analysis, the total value of a changing quantity is expressed as the sum of its equilibrium value (the constant value it would have if the wave disturbance were not present) and a time-varying "perturbation" that corresponds to the effect of the wave disturbance. For example, the acoustic pressure can be written as $p_{\text{tot}} = p_0 + p$ using this scheme, where p_0 is the equilibrium value, p is the perturbation, and p_{tot} is the total value. Linear acoustics assumes that the perturbation is "small" relative to the equilibrium value (e.g. $p \ll p_0$ in the case of pressure).

One starting point for deriving the wave equation is to note that any thermodynamic quantity (pressure, mass density, and entropy in this case) can be expressed as a function of the others via an equation of state [35]. Hence, under isentropic conditions, the acoustic pressure varies as a function of the total mass density only. Performing a Taylor series expansion of the pressure perturbation $p = p_{\text{tot}} - p_0$ as a function of the mass density perturbation $\rho = \rho_{\text{tot}} - \rho_0$ gives

$$p = \left(\frac{\partial p}{\partial \rho}\right)_{\substack{\rho=\rho_0 \\ \delta s=0}} \cdot \rho + \frac{1}{2} \cdot \left(\frac{\partial^2 p}{\partial \rho^2}\right)_{\substack{\rho=\rho_0 \\ \delta s=0}} \cdot \rho^2 + O(\rho^3). \tag{2.2}$$

In linear analysis, the second- and higher-order terms on the right-hand side of this formula are neglected, resulting in the following relationship between acoustic pressure and mass density:

$$p \approx \left(\frac{\partial p}{\partial \rho}\right)_{\substack{\rho=\rho_0 \\ \delta s=0}} \cdot \rho. \tag{2.3}$$

A similar first-order analysis may be applied to combinations of the equations for conservation of mass and conservation of linear momentum, as described elsewhere [23, 24, 35, 36]. By combining the results of this analysis with Equation 2.3, the wave equation in solids, liquids, and gases may be derived. In all of these substances, the end result can be expressed as

$$\nabla^2 p = \frac{1}{c^2}\frac{\partial^2 p}{\partial t^2} \tag{2.4}$$

where c is a constant whose value can be assumed to be positive without loss of generality (since only its square appears in the equation).

The general solution of the wave equation was first derived by d'Alembert; quoting the one-dimensional case for simplicity, it can be expressed as

$$p(x,t) = f_+(x - ct) + f_-(x + ct) \tag{2.5}$$

where f_+ and f_- are any two functions. Based on the form of the arguments of f_+ and f_-, it can be seen that these two functions respectively describe a forward-propagating wave (i.e. a wave moving towards positive x) and a backward-propagating wave (moving towards negative x), both travelling at a speed of c.

In the case of a wave that is periodic in both space and time, it is usually convenient to normalise the position and time variables by their periods. One way of doing this is to replace the function argument $(x \pm ct)$ with $(x/\lambda \pm t/T)$, where λ and T are respectively the spatial and temporal periods of the wave; the former is also referred to as the wavelength. Alternatively, the function argument can

also be expressed as $(\lambda^{-1}x \pm ft)$, where λ^{-1} is called the wavenumber—i.e. the spatial frequency of the wave—and $f = 1/T$ is the temporal frequency (often simply referred to as "the frequency"). Finally, in the case of a sinusoidal wave, the function argument is usually normalised to one cycle of the sinusoid by inserting a factor of 2π. Doing this yields the form $(kx \pm \omega t)$, where $k = 2\pi/\lambda$ is the angular wavenumber (in other texts, this is sometimes simply called "the wavenumber" instead of λ^{-1}) and $\omega = 2\pi f = 2\pi/T$ is the angular frequency. From these definitions, it can be seen that the following relation must hold:

$$c = \frac{\lambda}{T} = f\lambda = \frac{\omega}{k}. \tag{2.6}$$

In the general solution of the wave equation stated in Equation 2.5, the precise forms of the functions f_+ and f_- are dictated by initial and boundary conditions. Since the wave equation is linear, the frequency content of its solution will match that of its input, up to a scaling factor. In the case of HIFU, the forcing function is usually sinusoidal; hence, in linear regimes, so too is the propagating wave.

Two sinusoidal solutions to the wave equation are of particular interest for the purposes of this work. One is a plane wave of amplitude P and phase φ, which can be expressed mathematically as

$$p(x,t) = P\sin(\omega t \pm kx + \varphi). \tag{2.7}$$

This solution is significant because many periodic waveforms of practical interest may be expressed as a linear combination of plane waves using a truncated Fourier

series, up to an arbitrary accuracy. By linearity, such a superposition of plane waves will also satisfy the wave equation. In the context of this work, it can generally be assumed that HIFU is generated and propagated as plane waves (or at least waves that are very similar to planar ones), except where otherwise indicated.

The other solution of interest corresponds to a radially decaying spherical wave propagating away from a point source at the origin. In three dimensions, the radius r is given by $r = \sqrt{x^2 + y^2 + z^2}$. Hence, the source is at $r = 0$, and for $r > 0$ the emitted wave is described by

$$p(r, t) = \frac{P \sin(\omega t - kr + \varphi)}{r} \tag{2.8}$$

where P and φ again represent the amplitude and the phase, respectively. This solution is significant because any other wavefront can be viewed as consisting of an infinitely dense collection of point sources, according to Huygens' principle [35]. Unlike plane waves, spherical waves display geometric spreading, in that the wave energy spreads out over a larger volume as time passes.

2.1.5 The Speed of Sound

In acoustics, the speed c of the wave is referred to as the "speed of sound" (this term is used even when the acoustic wave in question is not in the audible range of frequencies). In solids, liquids, and gases, it can be shown that

$$c = \sqrt{\left(\frac{\partial p}{\partial \rho}\right)_{\substack{\rho=\rho_0 \\ \delta s=0}}} = \sqrt{\frac{E}{\rho_{\text{tot}}}} \tag{2.9}$$

where $\rho_{\text{tot}} = \rho_0 + \rho$ is the total mass density and E is relevant elastic modulus (for example, the bulk modulus B for a longitudinal wave, or the shear modulus G in the case of a transverse wave) [35, 36].

Equation 2.9 quantifies the manner in which elasticity and inertia affect acoustic wave propagation, and demonstrates that acoustic waves propagate fastest in stiff, low-density media. Furthermore, this formula shows that c is a function of two other material-specific properties; hence, the speed of sound can be regarded as a material-specific property in its own right, and its value is influenced by the same factors that affect the elastic modulus and the mass density (e.g. the ambient temperature; see Section 2.1.2).

The speed of sound in pure water between 0 °C and 95 °C is plotted in Figure 2.2 using the empirically derived formula by Marczak [37], which yields results accurate to within 0.2 m/s in this temperature range. The graph shows that the relationship between speed of sound and temperature is not always one-to-one. As will be discussed further in Section 3.4.5 (page 85), this complicates efforts to monitor the temperature of water-based substances (including many biological tissues) by tracking changes in their sound propagation speeds.

Appendix B lists the speeds of sound in various other substances, including all media exposed to ultrasound in this work. The water-based composition of the substances listed in Appendix B is reflected in the fact that their speeds of sound are all within 5% of the value for pure water.

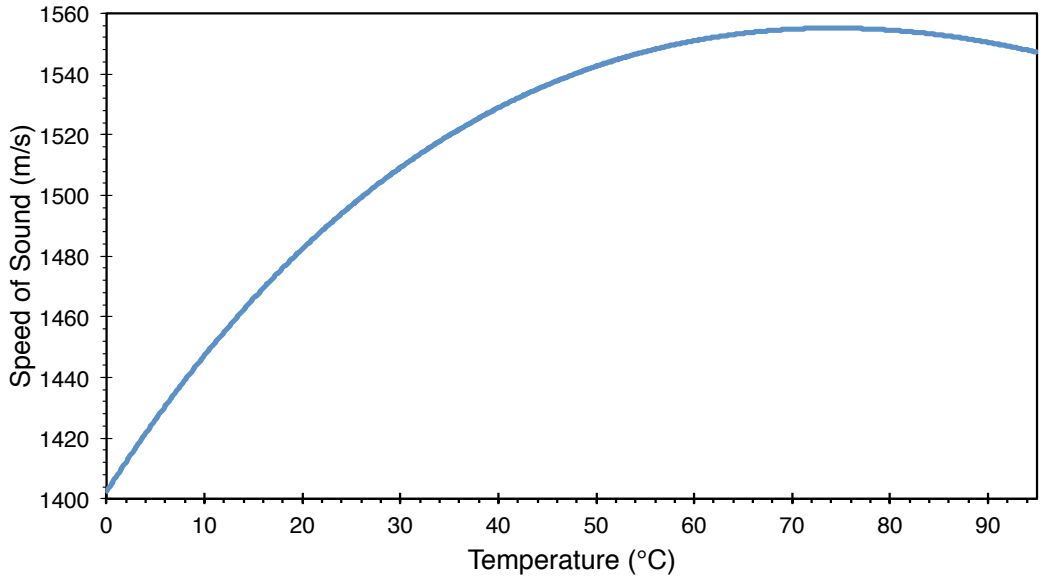

Figure 2.2: *Plot of the speed of sound in pure water from 0°C to 95°C, based on the equation by Marczak [37]. The formula is accurate to within 0.2 m/s in this temperature range.*

2.1.6 Wave Propagation at Boundaries

Thus far, the analysis presented in this chapter has implicitly assumed that wave propagation is taking place in a single, homogeneous medium with the same elasticity and mass density throughout. However, if a wave crosses into another medium that has different elastic or inertial characteristics, its behaviour at the boundary between these media must also be analysed. Typically, not all of the wave energy will be transmitted across such boundaries, because the mismatch between the two media will cause a portion of the wave energy to be reflected. Mismatched boundaries can occur throughout inhomogeneous media, including biological tissue.

In linear regimes, wave behaviour at a boundary is governed by the acoustic impedances of the substances on both sides of it. The acoustic impedance is denoted Z and can in general be a complex number; its value is material-specific and also

depends on the form of the propagating wave. In the special case of a plane wave, the acoustic impedance is a real number and is equivalent to the characteristic impedance of the medium, which can be calculated using the formula

$$Z = \rho_{\text{tot}} c. \tag{2.10}$$

Appendix B lists the characteristic impedances of various substances, including all media exposed to ultrasound in this work.

The manner in which the acoustic impedance affects wave propagation from a medium with impedance Z_1 to a medium with impedance Z_2 can be quantified using the amplitude reflection and transmission coefficients at the boundary. If the incident wave has an amplitude of P_{incident} and strikes the boundary surface perpendicularly, these coefficients are given by

$$\frac{P_{\text{reflected}}}{P_{\text{incident}}} = \frac{Z_2 - Z_1}{Z_2 + Z_1} \tag{2.11}$$

and

$$\frac{P_{\text{transmitted}}}{P_{\text{incident}}} = \frac{2Z_2}{Z_2 + Z_1} \tag{2.12}$$

where $P_{\text{reflected}}$ and $P_{\text{transmitted}}$ are the amplitudes of the reflected and transmitted waves, respectively. If either coefficient is not purely real (or is negative), the phase of the wave will also be shifted by that of the coefficient.

As Z_1 approaches Z_2, it can be seen from Equations 2.11 and 2.12 that the reflection and transmission coefficients respectively approach zero and unity. Hence,

reflection losses will be minimal at a boundary between two media whose acoustic impedances are closely matched. As shown by the values in Appendix B, this will usually be the case for the substances employed in this work: since all of them are water-based, their plane wave acoustic impedances are also well matched to that of pure water. However, this is not always the case in living organisms: for example, the acoustic impedances of bone and air are often very different from that of the surrounding tissue. For this reason, HIFU is unsuitable at this time for treating tumours in organs such as the brain, lung, and bowel. Moreover, even if the tissue containing the tumour allows ultrasound to pass with minimal reflections at its interface, it may still be difficult to ablate the tumour with HIFU if the target window is blocked by air-filled cavities or by bones such as the ribcage. Although research is ongoing into ways of mitigating this issue—for example, by using time-reversal focussing techniques [38]—it is likely that this intrinsic limitation will always be present to some degree in HIFU therapy.

2.1.7 Attenuation

Attenuation is an important feature of many media, and manifests itself as an exponential decrease in the amplitude of the wave as it travels through the medium. Although attenuation can arise from a combination of multiple nonlinear effects, in this work its dominant underlying mechanism is viscous absorption. This mechanism is of particular interest for HIFU ablation because it is responsible for the conversion of acoustic energy into heat [23, 39, 40]. Other mechanisms of wave attenuation include scattering [25, 36] and thermal conduction [35, 41]. At ablation-relevant pressure amplitudes, the effect of the former is typically insignificant compared to

viscous absorption; meanwhile, the latter can be neglected for individual acoustic cycles by virtue of the assumption of adiabatic wave propagation, which will be justified in Section 2.1.8.

For the plane wave described in Equation 2.7 (page 22), the effect of attenuation can be modelled by replacing the constant amplitude P with a term $Pe^{-\alpha x}$, where α is a material-dependent quantity called the attenuation coefficient. If the wave is travelling in a liquid and has a frequency below about 1 THz (a limit which is more than sufficient for the present work), the value of the attenuation coefficient can be calculated using the formula

$$\alpha(f) = \frac{2\pi^2}{\rho_{\text{tot}} V^3} \left(\frac{4}{3}\eta + \eta_{\text{b}} \right) f^2 \tag{2.13}$$

where η and η_{b} are, respectively, the shear and bulk coefficients of viscosity defined in Section 2.1.3 [30]. This result is an extension of Stokes' law to compressible fluids (the incompressible case originally derived by Stokes can be obtained by substituting $\eta_{\text{b}} = 0$ in this formula, i.e. by setting the bulk viscosity to zero).

Equation 2.13 is not accurate in soft tissues, which can be difficult to model analytically owing to their variable composition and the fact that they contain both solids and fluids. Instead, the following empirical relationship has been observed to hold in tissue:

$$\alpha(f) = \alpha_0 \left(\frac{f}{f_0} \right)^b = a f^b \tag{2.14}$$

where α_0 is a known value of attenuation at frequency f_0 [42] and $a = \alpha_0/(f_0)^b$. Appendix B lists the attenuation coefficient at 1 MHz for various substances, including

all those exposed to ultrasound in this work. The value of the power law exponent b is typically between 1 and 1.5: for example, b is approximately 1.1 in human liver, while its value in spleen is about 1.3 [28, 43]. It has also been observed that fatty tissues generally have higher exponent values: in fat itself, b is about 1.5, while in fatty liver it can range from 1.25 to 1.4 [44].

With the exception of the case $b = 2$, the empirical relationship between attenuation and frequency described in Equation 2.14 cannot be reconciled with the commonly used Kelvin-Voigt model of viscoelasticity (previously introduced in Section 2.1.2 as a parallel spring and dashpot) [27]. However, Kelly and McGough [28] have used the fractional-order parametric model of viscoelasticity (also previously mentioned in Section 2.1.2) to develop a model that successfully predicts the power law exponents for various biological media, including human liver tissue. This model also provides a better physical interpretation of the power law exponent b. For example, the case $b = 2$ can be shown to simplify to a single dashpot, which corresponds to a viscous liquid medium and would thus be expected to agree with Equation 2.13. Meanwhile, the fact that $1 < b \leq 1.5$ for many soft tissues can be interpreted as these tissues being more elastic than they are viscous. This interpretation also explains why b is generally higher in fatty tissue, as the extra fat would contribute additional viscous microstructure compared to lean tissue.

2.1.8 Limitations of Linear Acoustic Theory

As mentioned throughout this section, the acoustic theory described so far contains a number of assumptions whose applicability to this work must be assessed. This can

be accomplished by examining the typical orders of magnitude of various acoustic parameters under the conditions relevant to this work. This list is compiled in Table 2.1, based on the speeds of sound in Appendix B as well as the frequency, maximum acoustic power, and maximum pressure amplitude for the HIFU transducer used in this work (see Section 5.2.3, page 125). The orders of magnitude for the remaining quantities in Table 2.1 can be computed using Equation 2.6.

Quantity	Order of Magnitude
Speed of sound (c)	10^3 m/s = 1 km/s
Frequency (f and ω)	10^6 Hz = 1 MHz
Wavelength (λ)	10^{-3} m = 1 mm
Period (T)	10^{-6} s = 1 μs
Pressure amplitude (P)	10^6 Pa = 1 MPa
Power	10^2 W = 100 W

Table 2.1: *Orders of magnitude of various acoustic parameters in this work.*

Using the data in Table 2.1, the validity of the assumptions made so far is assessed in the following list.

Continuum Approximation: The assumption that the medium can be treated as a continuum only becomes problematic when the wavelength λ approaches the scale of the constituent particles of the medium (e.g. the mean free path in gases). However, in this work, the continuum assumption is justified because the wavelengths of interest are on the order of millimetres, which is multiple orders of magnitude greater than the scale of individual particles.

Adiabatic Process: At acoustic powers on the order of hundreds of watts, the amount of heat energy transferred to the medium over the course of a HIFU

exposure lasting a few seconds long will be in the range of hundreds of joules. However, given that the wave period is microseconds long, the amount of energy deposited in a single cycle will only be on the order of $10^{-4}\,\mathrm{J} = 100\,\mu\mathrm{J}$, and very little of this heat will have the chance to diffuse across an appreciable distance in such a short time. Hence, the approximation that HIFU wave propagation is a quasi-adiabatic process is acceptable for this work.

Constant Elastic Modulus and Mass Density: The assumption of a constant elastic modulus and mass density can also be justified with an argument similar to the one made for the previous assumption: although these values may change over the course of a seconds-long HIFU exposure, they will remain relatively constant during a single acoustic cycle lasting a few microseconds.

Small Pressure Perturbations: Linear acoustic theory assumes that the pressure perturbations caused by the acoustic wave are small relative to the equilibrium value. However, the pressure perturbations caused by a HIFU wave can be on the order of megapascals, which exceeds the atmospheric pressure of 101.3 kPa by a factor of 10 and is high enough to provoke a nonlinear response in many of the media used in this work (a quantitative justification of this assertion will be provided shortly in Section 2.2.1). Hence, the assumption of small pressure perturbations does not hold in HIFU ablation.

In summary, the only problematic assumption made so far is that of a linear regime. The next section therefore discusses nonlinear acoustics, and will clarify how the theory developed so far changes when the assumption of small perturbations no longer holds.

2.2 Nonlinear Acoustic Phenomena

This section provides an overview of selected topics in nonlinear acoustics. Detailed treatments of nonlinear acoustics may be found in the textbook by Hamilton and Blackstock [41], as well as the one by Morse and Ingard [35].

2.2.1 Quantifying the Degree of Nonlinearity

As mentioned previously, nonlinear acoustic phenomena only become important when the pressure perturbations become sufficiently large relative to the equilibrium value. The definition of "sufficiently large" depends on how nonlinear the medium of propagation is. Two metrics that quantify the degree of acoustic nonlinearity of a substance are its "B/A" value (pronounced "B-over-A," meaning "B divided by A") and its coefficient of nonlinearity (denoted β). These two quantities are related by the formula

$$B/A = \frac{\beta - 1}{2}. \tag{2.15}$$

Both B/A and β are material-specific properties. Their values are related to the coefficient of the second-order term in the Taylor series expansion for the pressure perturbation p (given earlier in Equation 2.2, page 20) [43, 45]:

$$B = (\rho_0)^2 \cdot \left(\frac{\partial^2 p}{\partial \rho^2}\right)_{\substack{\rho=\rho_0 \\ \delta s=0}} \tag{2.16}$$

and

$$A = \rho_0 \cdot \left(\frac{\partial p}{\partial \rho}\right)_{\substack{\rho=\rho_0 \\ \delta s=0}}. \tag{2.17}$$

As mentioned previously in Section 2.1.4 (page 19), second-order terms are neglected in linear analysis; hence, linear acoustic theory effectively assumes that $B = 0$, which implies that $B/A = 0$ and $\beta = 1$. Of course, a more complete characterisation of the nonlinearity of a medium might also involve the coefficients of the third- and higher-order terms in the Taylor series expansion of Equation 2.2, depending on the required level of accuracy.

In pure water, B/A is approximately 5.2, while its reported range for human liver tissue is 7.6 ± 0.8 [41, 46]. For pressures in the megapascal range—such as those encountered in HIFU ablation—these values are high enough to permit the occurrence of the nonlinear phenomena described in the remainder of this section [45].

2.2.2 Nonlinear Wave Propagation

Given that the wave equation derived in Section 2.1.4 does not apply in nonlinear regimes, several models of nonlinear acoustic wave propagation have been developed. These include the Khoklov-Zabolotskaya-Kuznetsov (KZK) equation [47, 48], which applies to directional, axisymmetric sound beams; the Westervelt equation, which is equivalent to the KZK equation [42]; the Burgers equation, which is a simplified version of the Westervelt equation [41]; and the fractional wave equation, which can be paired with the fractional-order parametric model of viscoelasticity that was discussed previously in Section 2.1.2 (page 14) [28]. A significant limitation of the first three equations (KZK, Westervelt, and Burgers) is their shared assumption that the attenuation coefficient of the medium varies as the square of frequency. As

stated earlier in Section 2.1.7 (page 27), this is the case in liquids (Equation 2.13) but not in soft tissues (Equation 2.14).

In nonlinear regimes, the pressure difference between the compressive and rarefactional regions of the wave can be large enough to alter the local bulk modulus significantly, which in turn affects the local speed of sound as per Equation 2.9 (page 23). Moreover, as the local particle velocity rises, the compressive parts of the wave will begin to travel faster than the parts undergoing rarefaction. Over a sufficiently long propagation distance, both of these effects will combine to distort an originally sinusoidal pressure wave into a shocked, sawtooth shape [45, 46, 49]. The points where abrupt changes in pressure occur (the "teeth" of the saw) are then referred to as shock fronts. The distance required for complete distortion of a sinusoid into a sawtooth wave is termed the shock formation distance; for a plane wave, it is given by

$$x_{\text{shock}} = \frac{1}{\beta k M} \tag{2.18}$$

where β is the coefficient of nonlinearity of the medium, k is the angular wavenumber of the original sinusoid, and M is the Mach number (defined as the ratio of the peak particle speed v to the speed of sound c in the medium, i.e. $M = v/c$) [50]. In the frequency domain, the distorted sawtooth wave will now contain some of its power at integer multiples of the frequency of the original sinusoid. This phenomenon illustrates that the frequency content of an acoustic wave can change under nonlinear propagation, unlike the linear regime described in Section 2.1.4 (page 19). Moreover, as will be shown in the next section, cavitating microbubbles can also perform extensive spectral redistribution of the energy in an acoustic wave.

2.2.3 Cavitation

Acoustic cavitation is perhaps one of the most complex nonlinear acoustic behaviours of all. Detailed treatments of this topic may be found in the textbooks by Leighton [36] and by Brennen [51], as well as in the review paper by Lauterborn and Kurz [52].

Cavitation refers to the phenomenon of tiny gas-filled bubbles (cavities) forming in a liquid when the local pressure falls below the vapour pressure. Hence, acoustic waves can induce cavitation if the rarefactional pressure amplitude is sufficiently high, as it can be in the case of HIFU. Three distinct phases of cavitation can be identified: nucleation, i.e. the creation of the bubble; bubble growth and oscillation, often in response to an external forcing function; and finally the collapse or dissolution of the bubble.

In the absence of pre-existing cavitation nuclei in the liquid, it can be shown that a rarefactional pressure of approximately 10 MPa is required to nucleate the angstrom-sized bubbles typically encountered in physiologically relevant conditions [24]. However, cavitation has been observed *in vivo* at rarefactional pressures as low as 1 MPa or 2 MPa, which suggests that stable nuclei are already present in many tissues [53]. The nature and origins of these nuclei are not fully understood, although numerous hypotheses have been put forth [54, 55]. Some proposed explanations for their existence include the presence of trapped air in micron-sized crevices found on the surfaces of impurities in the liquid [56], as well as an accumulation of organic

impurities on the walls of existing bubbles that prevents them from dissolving away [57].

Regardless of the nature and origin of any pre-existing nuclei, the quality and quantity of cavitation nuclei will naturally vary throughout any given liquid (barring any external intervention, such as seeding the medium with artificially generated nucleation agents). Hence, below the 10 MPa threshold mentioned earlier, the occurrence of cavitation is always probabilistic. This said, the probability of cavitation occurring will always increase with rarefaction pressure, and in many cases the concept of a "cavitation threshold"—i.e. the lowest rarefaction pressure at which cavitation is almost certain to occur—nevertheless makes sense. If an existing bubble is in hydrostatic equilibrium with the liquid around it, the pressure that it must overcome to grow and cavitate is referred to as the Blake threshold [58]. The cavitation threshold has also been shown to exhibit hysteresis, in that its value can be influenced by the pressures that have been previously applied to the liquid [59]. Finally, the cavitation threshold generally depends on both the acoustic frequency as well as the size of existing bubbles, as demonstrated by Apfel and Holland [60, 61] and illustrated in Figure 2.3 (reproduced from their paper). However, it should be noted that the Apfel and Holland result is only derived for pure water that is subjected to a single cycle of acoustic excitation. The underlying derivation also assumes that all sizes of nuclei are present, which is usually not the case in practice.

Once cavitation has started, the cavitating bubble will usually grow up to a certain point; after this, it can display a number of complex dynamic behaviours, depending on its local environmental conditions (e.g. the temperature) as well as the

Figure 2.3: *The cavitation threshold for a single-cycle acoustic wave in pure water as a function of initial bubble radius, at insonation frequencies of 1 MHz, 5 MHz, and 10 MHz. Here, all sizes of nuclei are assumed to present, and the nuclei themselves are assumed to consist of air bubbles that are initially at a temperature of 300 K. It can be seen that raising the applied pressure allows a broader size range of nuclei to cavitate. Reproduced from Apfel and Holland [60].*

external forces that it is subjected to (in HIFU ablation, the main forcing function is the HIFU wave). Several models have been developed to describe single-bubble dynamics under various conditions. One elementary model is the Rayleigh-Plesset equation, which is effectively a force balance equation expressed in terms of the displacement, velocity, and acceleration of the bubble wall [36, 51]. However, the Rayleigh-Plesset equation assumes that the medium is incompressible, and is therefore only valid for small-amplitude oscillations [62]. Another model by Keller and Miksis [27, 63] provides a further extension to the Rayleigh-Plesset equation that incorporates compressibility, and is thus capable of describing large-amplitude bubble oscillations. The ways in which bubble dynamics are affected by a time-varying temperature—which is assumed constant in many models, but does not remain

so during thermal ablation—have also been examined by Webb et al. [64]. Finally, bubble behaviour becomes even more complex when physical boundaries are present or when multiple bubbles are involved, because the oscillations of one bubble can influence the behaviour of its neighbours. Analyses have been developed for multi-bubble problems that display certain types of symmetry, as well as clouds containing a large number of randomly distributed bubbles [36].

Cavitation can also be described in qualitative terms, and can generally be classified phenomenologically as either stable or inertial, although many types of intermediate behaviour are also possible [36]. Stable cavitation refers to the prolonged, repeated oscillation of a bubble about its equilibrium radius over many acoustic cycles. On the other hand, inertial cavitation is characterised by a sudden, violent collapse of the bubble owing to the inertia of the surrounding liquid, generally over a single acoustic cycle [36, 51]. Inertial cavitation is particularly relevant in the context of thermal ablation, because the violent collapse of the bubble re-radiates energy across a broad spectrum of frequencies. As shown by Equations 2.13 and 2.14 of Section 2.1.7 (page 28), wave energy at higher frequencies is more readily attenuated and converted into heat. Hence, under the right conditions, instigating inertial cavitation during HIFU therapy can increase the rate of tissue heating by as much as 30-fold, thereby decreasing treatment time and improving the overall procedure [53]. Additionally, inertial cavitation can also cause mechanical damage to cells and tissue, notably by causing high-speed microjets to form in the liquid [51]. However, there are also many challenges in using inertial cavitation to enhance HIFU ablation, one of which is that cavitating bubbles can also shield the focal

zone by scattering incoming ultrasound. This phenomenon arises because of the large impedance mismatch at the bubble wall between the liquid outside the bubble and the gas inside it (see the earlier discussion in Section 2.1.6, page 25 regarding reflection and transmission coefficients at boundaries). Bubble shielding can cause unwanted cavitation in the pre-focal path, which has in turn been known to result in large "tadpole-shaped" lesions instead of controlled "cigar-shaped" ones. Another complication is that the cavitating bubbles themselves are generally difficult to control, although recent research by Hockham et al. [65] has demonstrated promise in addressing this issue.

Various theoretical criteria have been proposed for identifying inertially cavitating bubbles, including: a maximum bubble radius at least two times larger than the initial radius; a bubble wall velocity greater than the speed of sound in air (343.2 m/s); and a maximum internal temperature of at least 5000 K being achieved during collapse [36, 51]. However, for the purposes of this work, a far more practical method of classifying cavitation is to analyse the spectral content of the acoustic emissions from the bubbles themselves [59, 66]. In the case of stable cavitation, the periodic bubble oscillations characteristic of this mode will manifest themselves as increased acoustic noise in the harmonics (integer multiples of the HIFU frequency), subharmonics (integer fractions of the HIFU frequency), and ultraharmonics (harmonics of subharmonics). Meanwhile, the sharp collapse that characterises inertial cavitation in the time domain will translate in the frequency domain to increased broadband noise across the entire spectrum. Examples of spectra with prominent harmonics can be found in Figures 5.3c and 5.3d (page 132) of Section 5.2.3; the lat-

ter figure also shows increased broadband noise starting at a time of approximately 3.4 s.

The bubble emissions required for classifying cavitation in the manner just mentioned can be instigated either by listening for scattering of the HIFU wave itself (passive cavitation detection), or by sending out a pulse and monitoring the resulting echoes (active cavitation detection). In both cases, the returned emissions arise from the same mechanism responsible for bubble shielding, i.e. scattering of the acoustic wave by the bubbles as a result of the large impedance mismatch at their walls. However, passive detection has the advantage that it can be performed while the HIFU is on; active detection does not allow this, because the low-intensity pulse required to generate the echoes would simply be lost in the high-intensity therapeutic waveform. On the other hand, active cavitation detection offers the possibility of determining the axial position of the cavitating bubbles by measuring the time between sending the pulse and receiving the echo; no such information can be obtained in passive mode. Recent work by Kennedy et al. [67] has demonstrated the possibility of obtaining the best of both approaches by using quasi-continuous HIFU. In this approach, passive detection is performed while the HIFU is on, while the timing information required for positioning is obtained by using the start of the (short) periods during which HIFU is off as the reference point. For this reason, quasi-continuous HIFU will be employed throughout this work; the relevant parameter choices (e.g. duty cycle, pulse length) will be discussed later in Section 5.2.3 (page 125).

2.3 Design and Operation of Acoustic Transducers

Having established the main principles underlying the propagation of HIFU waves in biological media, the design and operation of the transducers used to create and measure acoustic pressure will now be discussed. Acoustic transducers typically make use of piezoelectric materials to either generate acoustic waves by converting electrical input energy into mechanical energy, or detect acoustic signals passively by performing the reverse conversion and using the mechanical energy from the wave itself to generate a voltage.

Transducers can either be unfocussed or focussed; in the case of the latter type, the geometry of the active surface is designed so that most of their wave energy ends up being concentrated in a specific region located a certain distance away from the transducer. The focal zone of a focussed transducer is usually defined as its $-3\,\mathrm{dB}$ region, or the region of space in which the beam power is no less than approximately half of its maximum value. The transducers used in the present work employ spherical focussing, which is illustrated in Figures 1.1 (page 2) and 2.4a. For these transducers, the $-3\,\mathrm{dB}$ region is shaped like a prolate spheroid.

The beam profile of focussed transducers can be examined in the axial direction—i.e. along an axis passing through the centre of the transducer and oriented normally to the radiating surface—as illustrated in Figure 2.4b. In this direction, the beam profile can be separated into near-field and far-field regions; the latter is where the focal zone shown in Figure 2.4a is located. In the far-field region, the beam amplitude initially increases up to the focal length and gradually decays thereafter.

(a) *Element diameter (D) and axial focal zone dimensions (start, Z_B; length, F_Z; and end, Z_E) in a spherically focussed transducer.*

(b) *Near and far field axial regions in a focussed transducer, with transverse beam profiles also indicated.*

Figure 2.4: *Illustrations of the focal zone and beam profiles of focussed transducers. Reproduced from technical notes by Olympus NDT [68].*

The distance at which the far-field region begins in a spherically focussed transducer is given by

$$N = \frac{D^2}{4\lambda} = \frac{D^2 f}{4c}. \tag{2.19}$$

where D is the diameter of the radiating element, depicted in Figure 2.4a [68, 69]. Using this quantity, the length F_Z of the focal zone can be calculated using the formula

$$F_Z = \frac{4F^2}{2N + F} \tag{2.20}$$

where F, the focal length, is the axial distance at which the beam amplitude is highest. This is a design parameter for most transducers, and falls midway between Z_B and Z_E in Figure 2.4a.

On the other hand, in a plane taken transversely through the focus—i.e. parallel to the radiating surface of the transducer—the beam profile will be approximately Gaussian in shape, with the maximum value occurring along the axis as illustrated

in Figure 2.4b. Sidelobes will also exist outside of the main focal region, although they will not be a major concern at the pressure amplitudes employed in this work. It can be shown that the $-3\,\mathrm{dB}$ beam diameter in a focussed transducer is given by $mF\lambda/D$, where m is a constant whose value depends on the distribution of energy across the radiating surface of the transducer [70]. For spherically focussed transducers, m is approximately 1.02 [68, 70], which yields in a $-3\,\mathrm{dB}$ beam diameter of

$$\mathrm{BD}_{\text{-3dB}} = \frac{1.02F\lambda}{D} = \frac{1.02Fc}{fD}. \tag{2.21}$$

Using this quantity, the transverse area of the focal zone can be found using the formula for a circle:

$$A_{\text{focus}} = \frac{\pi(\mathrm{BD}_{\text{-3dB}})^2}{4}. \tag{2.22}$$

The focal volume is given by the formula for a spheroid:

$$V_{\text{focus}} = \frac{\pi(\mathrm{BD}_{\text{-3dB}})^2 F_Z}{6}. \tag{2.23}$$

In many applications, including HIFU ablation, it is of interest to determine the acoustic power flux being generated by the transducer, i.e. the amount of acoustic power being generated per unit of transverse area. This quantity is known as the acoustic intensity. However, as mentioned previously, the power output of a focussed transducer is distributed non-uniformly across both space (because the beam profile varies throughout the focal zone) and time (because the wave amplitude at a given location in space changes as the wave propagates). Different methods of accounting for these variations can be used depending on the application, with each leading to

a different intensity metric. In this work, the quantity of greatest interest is the total amount of power deposited at the focus; hence the spatial-peak, time-averaged acoustic intensity (denoted I_{SPTA}) is the most relevant intensity metric for present purposes. In the case of a plane wave of amplitude P (see Equation 2.7, page 22), I_{SPTA} can be calculated using the formula

$$I_{\mathrm{SPTA}} = \frac{P^2}{2Z} = \frac{P^2}{2\rho_{\mathrm{tot}}c} \tag{2.24}$$

where the acoustic impedance for plane waves has been substituted from Equation 2.10 (page 26). Other intensity metrics include spatial-peak, temporal-peak intensity (I_{SPTP}) and spatial-average, temporal-average intensity (I_{SATA}). In the latter case, the spatial averaging is typically performed over the entire $-3\,\mathrm{dB}$ focal volume, although conventions sometimes vary in this regard. For the purposes of this work, it will be sufficient to note that I_{SATA} is always less than I_{SPTA}, independent of the convention chosen.

Lastly, the acoustic energy delivered during each exposure—henceforth referred to as the exposure energy—can be computed using the formula

$$E = I_{\mathrm{SPTA}} \cdot A_{\mathrm{focus}} \cdot t_{\mathrm{total}} \tag{2.25}$$

where t_{total} is the exposure duration. From a practical perspective, Equation 2.25 demonstrates that the key treatment parameters are exposure time (t_{total}), acoustic intensity (I_{SPTA}), and exposure energy (E). Any two of these three parameters may

be set independently, whereupon the value of the third is fixed by the aforementioned formula.

2.4 Summary

This chapter provided an overview of the acoustics of HIFU ablation. Acoustic waves were defined as mechanical pressure fluctuations that propagate through a medium (i.e. a substance that has elasticity and inertia). Two modes of acoustic wave propagation were described: the longitudinal or compressive mode, in which the wave oscillates along its axis of travel; and the transverse or shear mode, in which the wave oscillations are perpendicular to the axis of travel.

If the pressure fluctuations caused by an acoustic wave are sufficiently small, the propagation of the wave can be described using the linear wave equation (see Equation 2.4, page 21), which predicts that the wave will travel at a constant, medium-dependent speed referred to as the "speed of sound." However, several other factors not accounted for by the linear wave equation can also affect acoustic wave propagation, including viscosity, anisotropy, attenuation, and the presence of boundaries. Furthermore, if the medium of propagation exhibits a high degree of nonlinearity and if the pressure fluctuations are sufficiently large, nonlinear effects such as shock formation and acoustic cavitation may occur.

Finally, the design and operation of spherically focussed acoustic transducers was discussed. These transducers are designed such that the wave energy they generate ends up being concentrated within a prolate spheroid known as the focal zone. When using focussed transducers to perform HIFU ablation, the primary metrics of interest

include the acoustic intensity (the acoustic power generated per unit of transverse focal area; see Equation 2.24, page 44) and the acoustic energy (see Equation 2.25, page 44).

In the next chapter of this work, the medical and engineering background described thus far is used to review the existing methods of HIFU treatment monitoring. Multiple shortcomings in these methods will become apparent; the solutions that this work develops to address them will be outlined at the end of the next chapter.

Chapter

3

Monitoring Thermal and Mechanical Damage in Biological Media

This chapter provides a review of the techniques that are currently available for measuring thermal and mechanical damage in proteins, cells, and tissue. The effectiveness and the clinical adoption of HIFU ablation are hindered by limitations in these techniques. This chapter therefore concludes by outlining the solutions proposed in the present work for addressing current shortcomings in HIFU monitoring.

3.1 General Considerations

Detailed reviews of ablation monitoring may be found in the works of Goldberg et al. [71] and Rivens et al. [11]. However, before discussing the various ablation monitoring techniques that have been developed, it is important to define what is encompassed by the term "treatment monitoring." The definition employed in this

work follows the ones used by the two works previously mentioned, and is quoted next.

> Definition 3.1 (Treatment Monitoring)
>
> Treatment monitoring is "the process through which therapeutic effects are viewed during a procedure" [71], and includes an assessment of treatment safety and efficacy [11].

In Definition 3.1, safety implies that any treatment monitoring technique should promptly issue an alert whenever unwanted, adverse effects are on the verge of occurring outside of the focal area. Meanwhile, the notion of treatment efficacy is itself defined by a number of criteria, the most important of which are described in the following list.

1. **Real-Time Feedback:** An effective treatment monitoring method must indicate the amount of damage delivered as soon as possible, and ideally within a delay that is short enough to prevent overtreatment from occurring before action can be taken by the operator. Real-time methods allow for this, while also providing greater assurance to the operator that the treatment is progressing as intended. This is particularly important in the case of HIFU, where the non-invasiveness of the technique means that those administering the procedure must rely exclusively on instrument data to monitor the progress of the treatment. It should be noted that some of the methods presented in this chapter—particularly those dependent on diagnostic, pulse-echo ultrasound—can be applied in "quasi-real time" if the HIFU is switched off for sufficiently

long periods at regular intervals during ablation. However, this technique necessarily reduces the amount of power that can be delivered to the tissue, and in many cases these methods still cannot be regarded as truly real-time.

2. **Verified Accuracy:** Treatment monitoring methods should be verified to yield accurate results across the entire range of conditions that can be encountered during therapy. This is usually achieved by validating the method against an accepted "gold standard," examples of which will be provided throughout this chapter. Typically, gold standard methods are known to produce highly accurate results but do not meet the other criteria in this list, and are therefore unsuitable for clinical use themselves. The accuracy of a method can also be further justified by ascertaining the physical mechanisms that allow the method to yield valid results. However, this is sometimes difficult to do—particularly in complex systems such as cells and tissues—and should in any case always be accompanied by validation against a gold standard if one exists. Accurate monitoring methods should also provide some form of spatial localisation, which allows the operator to confirm that damage has occurred only at the intended location. In image-based monitoring techniques, this requirement implies that the spatial resolution of the images must be sufficiently high.

3. **Convenience:** Passive monitoring techniques that provide clear visual feedback typically score well with respect to convenience; on the other hand, monitoring techniques that require long processing times or impose a high burden on those administering the treatment are less likely to be adopted clinically. The

quality of the implementation—for example, the design of any user interfaces—can also influence the clinical adoption of a treatment monitoring method, sometimes independently of the efficacy of the method itself.

4. **Low Cost:** In the case of HIFU, the cost of the equipment required for performing the therapy itself is typically in the thousands of dollars. This compares favourably with the fixed costs associated with the other cancer therapies listed in Section 1.3 (page 6). Hence, monitoring techniques that cost orders of magnitude more than this amount will reduce the number of clinics that can afford the required equipment, and thereby prevent HIFU therapy from being used to its full potential.

Throughout this chapter, the safety and efficacy of each monitoring technique will be assessed using the aforementioned criteria. Although each criterion in this list is important, it will become apparent that very few of the available monitoring techniques—and none of the ones that are used clinically—meet all of the criteria for safe and effective monitoring. The shortcomings of the available methods will be summarised in Section 3.5, and will provide the motivation for the experiments described in the subsequent chapters of this work.

3.2 Protein Denaturation

3.2.1 Overview

Before discussing ablation-induced damage in cells and tissue, it is worth examining the biological effects of heat at an even smaller scale: that of protein molecules. In

the next section, it will shown that heat-induced protein damage plays a critical role in cell death and tissue necrosis at ablation-relevant temperatures. Hence, it is useful to understand the behaviour of proteins under thermal stress, since this behaviour may in turn provide insight into the dynamics of more complex systems such as cells and biological tissues.

Proteins are found in many of the known living organisms, and are themselves integral components of cells and tissues. All proteins are comprised of compounds known as amino acids, which are connected sequentially in a chain of 30 or more. In every protein-containing organism, the same set of 22 amino acids is used to build many different protein molecules. Proteins serve a number of important biological functions, several of which are listed next.

Structural proteins give rigidity and stiffness to biological materials. Examples include keratin (hair and nails) as well as collagen and elastin (connective tissue).

Enzymes are proteins that help catalyse many important biochemical reactions.

Antibodies are proteins generated by the immune system. Their main function is to neutralise toxins and other antigens by binding to them.

Messenger proteins allow signals from one cell to be transmitted to other cells in different parts of the body. Examples include insulin and glucagon.

Membrane proteins act as receptors for signalling molecules by providing them with binding sites.

Transmembrane proteins change the permeability of cell membranes to permit the flow of small molecules and ions into and out of cells (e.g. the ion channels for sodium and potassium).

Transport proteins bind to small molecules and transport them to other locations. Examples include hemoglobin (oxygen transport) and serum albumin.

The most distinctive feature of all protein macromolecules is the 3-D geometric structure that they possess. This structure varies depending on the sequence of amino acids that constitute the protein, and is kept in place by various hydrogen bonds between different parts of the amino acid chain [72]. It is the structure of a protein that plays the greatest role in determining its biological function, as well as its ability to carry out that function effectively. For example, enzymes, antibodies, and transport proteins must all have a specific shape to bind to their targets. Exposing a protein molecule to external sources of stress—such as heat—can disrupt its three-dimensional structure; this phenomenon is called denaturation, and typically results in the protein losing its biological functionality [73]. In many cases, denaturation is a reversible process, and the protein molecule will revert to its original structure once the external stressor has been removed. However, high levels of sustained stress can cause the hydrophobic regions of the protein to be exposed, thereby forcing the proteins to aggregate and causing irreversible denaturation [74].

For the purpose of describing protein structure, four canonical structural levels have been defined; these are illustrated in Figure 3.1. The most fundamental level is the primary structure, which consists of the specific sequence of amino acids that form the protein molecule. Next are the secondary and tertiary structural levels,

which refer to the three-dimensional shapes formed locally by segments of amino acids within the protein molecule (secondary) or between the secondary structure motifs themselves (tertiary). Finally, in proteins that are comprised of multiple amino acid chains, the positioning of these chains relative to one another is called the quaternary structure. In the case of thermally induced stress at HIFU-relevant temperatures (i.e. up to 100 °C), the protein structure may change at the secondary level and higher, but the primary structure usually remains intact [73]. This is evidenced by the fact that the same amino acid chains present in human proteins can also be found in organisms that live in high-temperature environments.

Figure 3.1: *The four canonical levels of protein structure. Reproduced from Berg et al. [72].*

In summary, protein denaturation at ablation-relevant temperatures arises from changes in the structure of the protein molecules at the secondary level and above. The remainder of this section therefore provides an overview of methods that can be used to obtain information on protein structure—and hence denaturation—during or following heating.

3.2.2 Optically Measured Damage in Protein-Embedding Hydrogels

Protein-embedding hydrogels are commonly used as tissue-mimicking materials in laboratory "bench-top" testing of hyperthermia and thermal ablation [75–80]. In these materials, proteins such as Bovine Serum Albumin (BSA) or egg albumin are dissolved in water and then set in a transparent gel matrix such as agar, polyacrylamide, or calcium alginate. These protein-embedding hydrogels have the desirable property of visibly changing in opacity when the embedded proteins denature after being heated, as shown in Figure 3.2. Moreover, although the proteins embedded in the gel remain dissolved in water, their movement is restricted by the gel matrix; hence, the gels preserve the spatial location of the thermally induced damage that caused the protein denaturation. This can be seen in the localised "lesions" of denatured protein in Figure 3.2.

The opacity of protein-embedding hydrogels is straightforward to measure using an optical sensor (e.g. a camera) and elementary image processing techniques [81], and has the major advantage that it can be monitored in real time [79]. Opacity-based damage monitoring therefore meets Criteria 1 (real-time feedback), 3 (convenience), and 4 (low cost) for effective treatment monitoring (see Section 3.1, page 47). However, Criterion 2 (verified accuracy) is not entirely satisfied, because two issues remain to be addressed if gel opacity is to be used as a quantitative, biologically relevant measure of thermal damage. Firstly, the biological relevance of this metric would need to be established across a range of temperature profiles relevant to modern hyperthermia and thermal ablation therapies. This could be accomplished

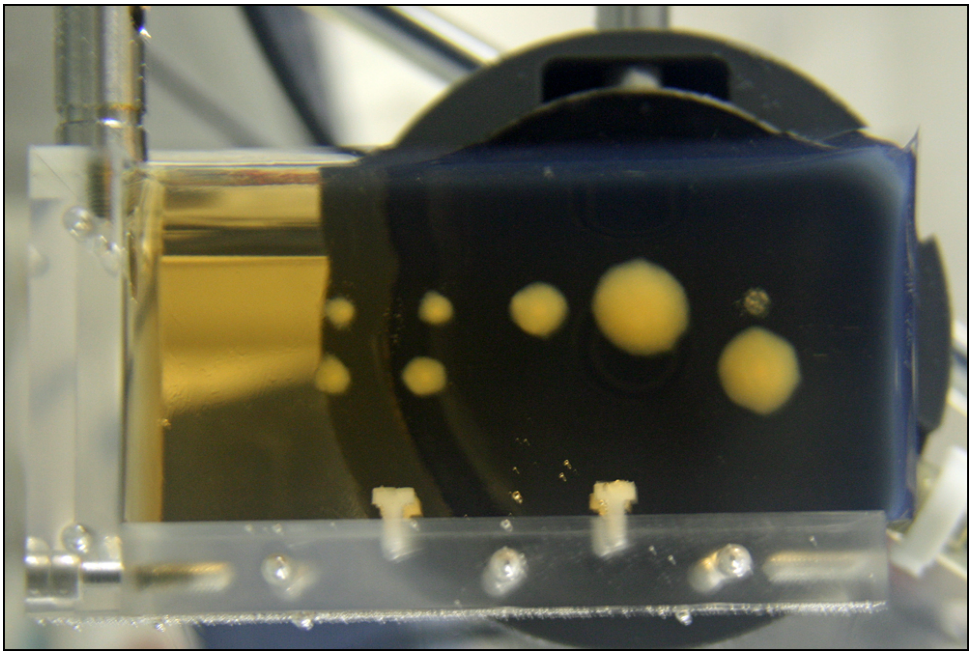

Figure 3.2: *An illustration of the change in the opacity of a polyacrylamide hydrogel with embedded Bovine Serum Albumin (BSA) following heat-induced damage. The opaque "lesions" of thermally denatured proteins were created by exposure to HIFU, which was generated by the transducer shown in the background.*

by comparing the opacity value with the degree of thermally induced damage sustained by a more biologically relevant system for the same amount of heating, such as a suspension of cells. Secondly, the physical mechanisms underlying the optical metric of damage would need to be investigated in order to clarify the link between heat-induced structural changes in the protein molecules and the macroscopically visible change in gel opacity. As will be seen later, both of these issues are addressed with the experimental work described in Chapter 4.

3.2.3 Structural Analysis of Aqueous Proteins

Many analytic techniques exist for assessing the structure of proteins dissolved in water, including Ultraviolet/Visible Spectroscopy (UV/VIS), Dynamic Light Scattering (DLS), Size Exclusion Chromatography (SEC), and Fourier Transform In-

frared Spectroscopy (FTIR). All of these methods measure structural properties directly, and thus have a relatively high degree of accuracy (Criterion 2 in Section 3.1). However, the equipment required to apply these techniques is highly specialised and can be costly; in addition, these methods only work if the proteins are dissolved in water (i.e. if they are in aqueous form). These methods therefore do not meet the remaining criteria in Section 3.1, but are well suited to providing "gold standard" measurements of protein denaturation.

Ultraviolet/Visible Spectroscopy

UV/VIS spectroscopy is a technique for measuring the number of insoluble protein aggregates by observing their effect on optical transmittance at a suitable wavelength of light. The sample is placed in a transparent cuvette, and a single-wavelength beam of light of some known intensity is shone through it. The intensity of the beam is then measured on the other side of the cuvette (i.e. after having passed through the sample).

UV/VIS exploits that fact that the insoluble particles in the sample will scatter the incident light, which therefore does not make its way to the detector; this is known as turbidity analysis. The wavelength of the incident light beam may lie anywhere in the ultraviolet or visible spectrum (which gives the technique its name), although for best results, resonant peaks in the absorption spectra of the dissolved molecules should be avoided.

Dynamic Light Scattering

DLS can be used to determine the size distribution of dissolved particles such as protein aggregates. Like UV/VIS, the technique relies on the scattering of incident light to detect the particles. In DLS, intensity fluctuations in the scattered light over time are used to infer the time taken for the scatterer to move through the liquid; this, in turn, provides information on the size of the scatterer. As with UV/VIS, for best results the wavelength of the light should not lie near resonant peaks in the absorption spectra of the dissolved particles.

Size Exclusion Chromatography

The SEC technique is illustrated in Figure 3.3 and can be used to measure the quantity of soluble protein aggregates. SEC is a variant of a method known as High Performance Liquid Chromatography (HPLC) [82]. In HPLC, a constant pressure is used to pump the liquid sample through a column that consists of a tube filled with specially designed packing material. In SEC, the packing material is porous, and is designed such that smaller particles will flow through more of the pores, thereby taking more time to pass through the column. By placing an appropriate detector—typically a UV/VIS spectrometer—at the output of the column, the number of particles exiting the column can be measured over time. The graph so obtained is called a chromatogram; an example plot is shown in Figure 4.4 (page 107).

Since the amount of time required for a particle to pass through an SEC column varies inversely with its size, SEC chromatograms can be used to obtain the size distribution of monomers (unaggregated protein) and soluble protein aggregates in

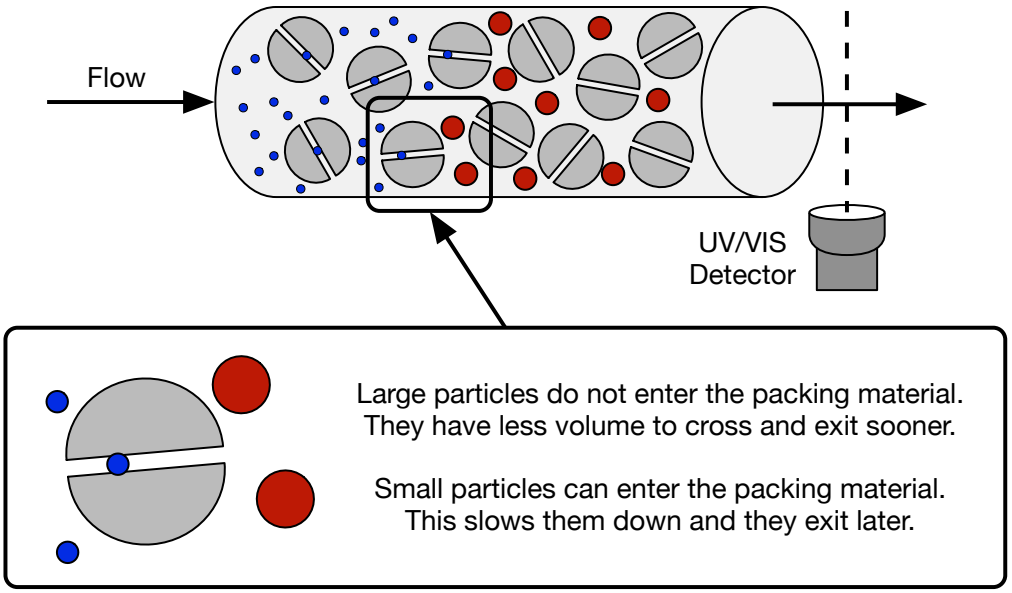

Figure 3.3: *An illustration of the method of Size Exclusion Chromatography (SEC).*

a sample [82]. To accomplish this, the setup must be calibrated with high-purity substances of known sizes; these are referred to as molecular weight standards. Calibration allows various column exit times in the chromatogram to be associated with sizes instead. The number of particles at a given exit time (and hence of a given size) can then be calculated by comparing the areas under the peaks in the chromatogram. However, this calculation is only reliable if the peaks are sufficiently well separated: otherwise, the areas corresponding to consecutive peaks will overlap, and it may be difficult to determine which peak the overlapping area should be associated with. It is possible to increase the separation between peaks by lowering the HPLC pump pressure, which "stretches" the time axis by making all particles take longer to traverse the column. However, this strategy only works up to a certain point, because in practice a minimum amount of pressure is required to ensure steady flow through the system.

Fourier Transform Infrared Spectroscopy

FTIR can be used to measure the relative amount of different secondary structure motifs present in the protein sample. FTIR is a complex technique with many applications, and is only summarised here; more extensive information may be found in the work of Arrondo et al. [83].

FTIR is a specialised version of a more general method called Fourier Transform Spectroscopy (FTS), which uses the setup shown in Figure 3.4. This apparatus is essentially a slightly modified version of an instrument known as a Michelson interferometer. In FTS, light from a coherent source is split into two beams, each of which travels along its own path before being recombined and passed through a sample of the material to be characterised. Depending on the difference between the lengths of the paths travelled by the two split beams, the beams will interfere with each other to various degrees when recombined, resulting in light of a certain temporal coherence. In a standard Michelson interferometer, the mirrors that reflect the split beams are fixed, but in FTS, one of the mirrors may be translated along the axis of travel of the split beam. Moving this mirror changes the difference in the path lengths, which in turn alters the temporal coherence of the light that penetrates the sample. It is then possible to reconstruct the absorption spectrum of the sample measuring the temporal coherence of the received light for many different time delays. FTS possesses a number of advantages compared to standard spectroscopic methods, including a considerably higher signal-to-noise ratio [83].

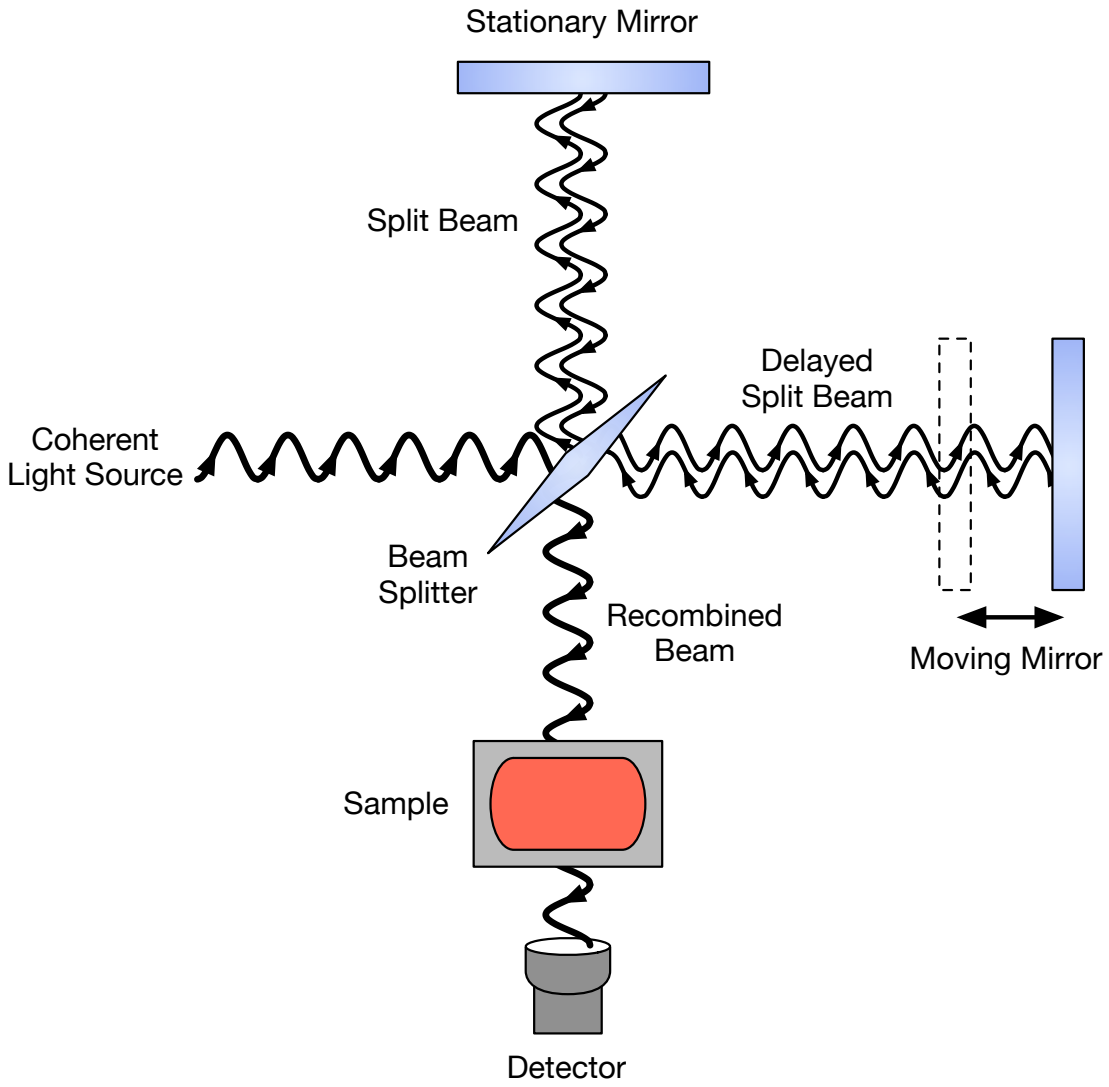

Figure 3.4: *Setup for Fourier Transform Spectroscopy (FTS), of which Fourier Transform Infrared Spectroscopy (FTIR) is a variant. The device is similar to a Michelson interferometer, but incorporates a variable delay in one of the split beam paths because of the moving mirror. In this diagram, the light originates from the coherent source on the left, after which it splits and propagates along the upper and right paths. The split beams then recombine and travel along the lower path, which passes through the sample and into the detector.*

FTIR simply consists of using an infrared light source in an FTS setup to obtain the infrared spectrum of the sample. For the purposes of this work, the most interesting set of frequencies in the infrared range lie in a region known as the Amide I band, which spans wavenumbers from $1700\,\mathrm{cm}^{-1}$ to $1600\,\mathrm{cm}^{-1}$. In this band, the high signal-to-noise ratio of the FTIR technique makes it possible to measure the resonant frequencies of the bonds between certain key pairs of atoms in the proteins. This information can then be used to distinguish the type of secondary structure that these atoms are a part of. Hence, by using FTIR to analyse protein samples subjected to different levels of heating, it is possible to determine what changes occur in the secondary structure of the proteins following their denaturation.

3.3 Cell Death

3.3.1 Overview

The proteins described in the previous section are one of the main constituents of cells, which are themselves the fundamental unit of many living organisms. Notably, cells are one of the main components of biological tissue, along with vasculature (blood vessels) and the extracellular matrix. As discussed earlier in Section 1.2 (page 4), all cancers begin at the cellular level with cells that display the hallmarks shown in Figure 1.3 (page 5). Hence, one way of monitoring thermal ablation is to measure the amount of cell death that has taken place. For the purposes of this section, it will be assumed that the cells are *in vitro*; the *in vivo* case will be considered in Section 3.4, which discusses the monitoring of tissue necrosis.

Detailed reviews of the biochemical response of cells to heat may be found in the works of Hildebrandt et al. [84] as well as He and Bischof [4]. At the subcellular level, no single subcellular system or organelle has been identified as the main target of heating. Cotran et al. [85] state that following four systems are particularly vulnerable to the effects of heat:

- The cell membrane and the associated organelles that synthesise it (including the Golgi apparatuses, the ribosomes, and the endoplasmic reticulum);
- The genetic apparatus, which is primarily located in the nucleus of the cell;
- The aerobic respiration system (e.g. the mitochondria); and
- Enzymes and structural proteins (see the discussion in the previous section).

At the molecular level, the primary constituents of cells (apart from water) are proteins, lipids, DNA, and RNA. However, the structure of the latter two substances is unaffected below 85 °C, while the phase transitions for the major lipids take place below 40 °C [4]. Hence, at ablation-relevant temperatures, heat-induced denaturation of cellular proteins—the dynamics of which were discussed in the previous section—likely plays a significant role in causing cell death [86]. The experimental evidence available to date also supports this hypothesis: for example, Lepock et al. [87] as well as Burgman and Konings [88] have observed that protein denaturation occurs in mammalian cells during hyperthermia, and it is also known that proteins play a critical role in determining the heat shock response of cells [89, 90]. Nevertheless, the other molecular components of cells may also play important roles in the biochemical pathways that lead to heat-induced cell death. Notably, the stability of

proteins that are embedded in lipids—such as the membrane proteins mentioned in the previous section—is strongly influenced by the lipids that surround them, even if the lipids themselves are not affected by the heating [4].

In summary, the biochemistry of thermally induced cell death is complex and not completely understood. Hence, developing methods for monitoring and measuring cell death necessarily involves making some simplifying assumptions, which in turn means that these methods will only yield accurate results if these assumptions are satisfied. The remainder of this section discusses two general approaches for measuring cell death, as well as the assumptions that each approach makes. The first is cell viability assaying, which can be used to obtain gold standard measurements of cell survival but is unsuitable for real-time ablation monitoring. The second approach is thermal dosimetry, which is currently the most popular method of quantifying cell death during or following thermal ablation, but is also subject to a number of important shortcomings and limitations.

3.3.2 Cell Viability Assays

Assays are substances that can be used to test for a specific feature in a biological sample. The assays of particular interest to this work are those that test cell viability. Many different cell viability assays are available; each typically uses a series of specific biochemical reactions to test for the presence or absence of a specific property that is characteristic of either live or dead cells. The three assays that will be employed in this work (specifically, in Chapters 4 and 5) are described in the following list.

MTS dye reacts with the phenazine methosulfate (PMS) enzyme to produce a formazan dye with an absorbance maximum at 490 nm; this dye can therefore be detected using UV/VIS spectroscopy (see Section 3.2.3, page 55). Since the PMS enzyme is only present in living cells, MTS assays provide a measure of cell viability.

Calcein AM (calcein acetoxymethyl ester) is a molecule that can be transported across cell membranes. If the cell is viable, esterases within the cell will remove the acetoxymethyl group from any calcein AM molecule that has entered. The remainder of the assay molecule is then trapped inside the cell and fluoresces at green wavelengths of light (peak emissions at approximately 515 nm) if excited at or near 495 nm. Since the esterases that allow this process to happen are only present in living cells, calcein AM also provides a measure of cell viability.

Propidium iodide is excluded from living cells and generally cannot cross cell membranes; however, if the cell is dead and its membrane has been lysed (i.e. opened), the molecule will enter the cell and bind with the DNA in its nucleus, as well as with any RNA that is present. The bound assay molecules will then fluoresce at red wavelengths (around 620 nm) if excited at approximately 490 nm. This makes propidium iodide well suited to detecting cells that have died from mechanical damage. As mentioned previously in Section 2.2.3 (page 35), one known mechanism of cell membrane lysis during HIFU ablation is the formation of microjets from inertially cavitating bubbles; since this damage is mechanical in nature, it can be detected with a propidium iodide assay.

The last two assays (calcein AM and propidium iodide) may be detected using a fluorescence microscope. A detailed review of fluorescence microscopy may be found in the paper by Lichtman and Conchello [91], but is not necessary for the purposes of this work.

In many assays—including the three just listed—the biochemical mechanisms that underlie the assay are well understood, and hence the results obtained are highly accurate. On the other hand, certain assays can be fairly costly; moreover, assays cannot be used *in vivo*, and even for *in vitro* models, they cannot be applied in real time. Cell viability assays can therefore be used as gold standard measures of cell death, but are not suitable for ablation monitoring per the criteria in Section 3.1.

3.3.3 Thermal Dosimetry

The Definition of Thermal Dose

One of the simplest ways of providing a physical description of a hyperthermic exposure is to specify the temperature profile as a function of time. Thermal dosimetry is based on this idea, and aims to quantify heat-induced damage to cells based on knowledge of the temperature profile that the cells have been subjected to.

Detailed reviews of thermal dosimetry may be found in the papers by Dewhirst et al. [92] and by Dewey [93]. Early proposed definitions for thermal dose include degree-minutes (the integral of temperature over time) [94] as well as the amount of heat energy deposited [95–99]. However, neither of these definitions produces thermal dose values that agree well with experiments, and in some cases these metrics

have been shown to yield identical dose values for temperature profiles that cause dramatically different levels of cell death [93]. To overcome these difficulties, thermal dose is instead defined based on the time required to produce a biological "isoeffect" at a given reference temperature [84, 92, 100], as stated in the next definition.

> Definition 3.2 (Thermal Isoeffective Dose)
>
> Suppose that a substance is heated according to a certain temperature profile, which may vary throughout both time and space. Then the thermal isoeffective dose associated with that temperature profile at a given, constant reference temperature is the amount of time for which the substance would have to be maintained at the reference temperature in order to sustain the same amount of damage caused by the original temperature profile.

This definition specifies that thermal dose is measured in units of time at a specified reference temperature. In the literature, thermal dose values are commonly quoted in minutes, and the reference temperature is usually taken to be 43 °C after a seminal study by Sapareto and Dewey [94] that will be described shortly.

Although Definition 3.2 circumvents many of the difficulties inherent in earlier measures of thermal dose, it does not provide a practical method for computing the thermal dose associated with an arbitrary temperature profile. The only method suggested by the definition is to determine the equivalent dose by finding, via trial-and-error, the amount of time for which the sample must be held at the reference temperature in order to sustain an equivalent amount of damage. Since this method of determining the isoeffective dose is clearly impractical, multiple frameworks for

calculating the isoeffective dose associated with temporally and spatially varying temperature profiles have been developed [101]. The most important and commonly used frameworks are described next.

Time-Varying Temperature Profiles

Of the various thermal dose models available for calculating the damage delivered to a population of cells (denoted Ω), many are derived from chemical kinetics or empirical laws. One starting point of this type is the Eyring equation, which is based on statistical thermodynamics and can be expressed by the first-order rate law

$$\Omega_{\text{Eyring}}(t) = \frac{k_{\text{B}}}{h} \int_0^t T(\tau) e^{-\frac{\Delta G}{R_{\text{gas}} T(\tau)}} \, \mathrm{d}\tau \tag{3.1}$$

where t is the elapsed time since the start of the treatment, k_{B} is Boltzmann's constant, h is Planck's constant, ΔG is the Gibbs free energy, R_{gas} is the ideal gas constant, and T is the absolute temperature as a function of time (assumed to exceed the normal body temperature of 37 °C) [102]. The Eyring equation may be simplified further by assuming that there is a single chemical reaction responsible for causing the damage Ω. Denoting the activation energy of this reaction by E_a [103], it can be shown that Equation 3.1 reduces to an Arrhenius law under this assumption [92, 102]. This Arrhenius equation has the form

$$\Omega_{\text{Arrhenius}}(t) = A \int_0^t e^{-\frac{E_a}{R_{\text{gas}} T(\tau)}} \, \mathrm{d}\tau \tag{3.2}$$

where A is a constant of proportionality.

The Arrhenius model in Equation 3.2 has been employed by some practitioners of therapeutic ultrasound; notably, Lizzi et al. [104] used it to calculate HIFU-induced damage in ocular tissue. However, the most popular method of computing thermal dose in HIFU thermal ablation is based on a variant of the Arrhenius model popularised by Sapareto and Dewey [94]. Starting from the Arrhenius relationship in Equation 3.2, Dewey et al. [101] postulated that for most biological systems, two thermal doses corresponding to a time of t_1 at reference temperature of T_1 and a time of t_2 at reference temperature of T_2 are equivalent if they satisfy the criterion

$$t_2 = t_1 R^{\frac{T_2 - T_1}{1\,\mathrm{K}}} \tag{3.3}$$

where the placeholder variable R is given by

$$R = e^{-\frac{E_a \cdot 1\,\mathrm{K}}{R_{\mathrm{gas}} T_1 T_2}}. \tag{3.4}$$

Based on these equations, Sapareto and Dewey formulated a damage model which has come to be known as Cumulative Equivalent Minutes (CEM) [92, 93]. In this model, the isoeffective dose at a reference temperature of T_{ref} may be computed using the formula

$$\Omega_{\mathrm{CEM}}(t) = \mathrm{CEM}_{T_{\mathrm{ref}}}(t) = \int_0^t R(T(\tau))^{\frac{T_{\mathrm{ref}} - T(\tau)}{1\,\mathrm{K}}}\,\mathrm{d}\tau \tag{3.5}$$

where the placeholder function R is now given by a modified version of Equation 3.4:

$$R(T) = e^{-\frac{E_a \cdot 1\,\mathrm{K}}{R_{\mathrm{gas}} T (T + 1\,\mathrm{K})}}. \tag{3.6}$$

The choice of reference temperature is arbitrary, but is commonly taken to be 43 °C as in the original study by Sapareto and Dewey [94].

Although the activation energy E_a in Equation 3.6 (as well as in Equations 3.2 and 3.4) is cell-dependent, it is common practice in the literature [5, 32, 84, 92, 105–111] to simply use the following piecewise approximation of R when calculating CEM values:

$$R(T) \approx \begin{cases} 0.5 & \text{if } T \geq 43\,^{\circ}\mathrm{C}; \\ 0.25 & \text{if } 37\,^{\circ}\mathrm{C} \leq T < 43\,^{\circ}\mathrm{C}; \\ 0 & \text{otherwise.} \end{cases} \tag{3.7}$$

This approximation was first employed by Sapareto and Dewey [94] in the same paper that formulated the CEM model for the first time. For that study, the use of Equation 3.7 was justified because it does not induce much error from 37 °C to 46 °C, which is the range of temperatures that the authors were interested in. However, the validity of this approximation has not been verified above 54 °C [94, 112]. Furthermore, even below this temperature, some studies report values of R ranging from 0.4 to 0.8, depending on the cell line [101]. This is expected because the value of the activation energy (E_a) is cell-dependent and therefore influences the value of R. Hence, the potentially unwarranted use of the approximation in Equation 3.7 at ablation-relevant temperatures—which can lie well above the highest verified

temperature of 54 °C—casts significant doubts on the validity of the thermal dose values reported in many studies, including several of the ones mentioned previously (references [5, 32, 84, 92, 105–111]).

Although kinetic models such as the Arrhenius one are currently the most widespread method of modelling cell death during HIFU ablation, several alternative thermal dose models based on statistical principles have been proposed. For example, Moussa et al. [113] introduced the concept of cellular "susceptibility" to heat-induced damage and postulated that the number of cells with a certain level of susceptibility follows a Gaussian distribution. Jung [114] developed an Arrhenius-like model by assuming that thermal damage in cells is governed by a two-step process that can be modelled with a Poisson distribution. Recently, Feng et al. [112] developed a two-state model of heat-induced cell death in which the damage function takes the form

$$\Omega_{\text{2-state}}(t) = \frac{1 + \tanh(\Phi(t))}{2} = \frac{e^{2\Phi(t)}}{1 + e^{2\Phi(t)}} \tag{3.8}$$

where t is the total heating time and Φ is an unknown function. Based on experiments with *in vitro* RWPE-1 and PC3 cells (normal and cancerous human prostate cells, respectively), Feng et al. found that the two-state model yielded better predictions of cell death than the Arrhenius model if the function Φ took the form

$$\Phi(t) = \frac{C_1}{T(t)} + C_2 t + C_3 \tag{3.9}$$

where C_1, C_2, and C_3 are constant parameters whose values depend on the cell line. The authors validated this model for temperatures of up to 60 °C. However, in spite of these encouraging results, none of the statistical models of thermal dose have as yet displaced the more commonly used kinetic models such as CEM.

Spatially Varying Temperature Profiles

The thermal dose models described previously all assume a temperature distribution that is constant throughout the ablated region. One method of accounting for spatial variation in the temperature profile is to calculate the thermal dose at each sample point and average the results over the ablated volume. However, this approach has the weakness that cancerous cells could survive in areas that received a low thermal dose, even if the average thermal dose delivered to the entire ablated region were relatively high. Hence, the more common method used in the literature is to consider a percentile of the temperature distribution over the ablated volume. This results in a metric called a T_n spatial temperature descriptor, which is defined next.

> Definition 3.3 (T_n Spatial Temperature Descriptors)
>
> Let n be a number from 0 to 100 inclusively. The value of the T_n spatial temperature descriptor is the highest temperature met or exceeded in at least n% of the ablated volume.

As an example, if the region being ablated has a T_{90} temperature of 65 °C, this means that at least 90 % of the volume has a temperature of 65 °C or higher. In the literature, the T_{90} metric is most often used, although the T_{50} and T_{100} metrics

are sometimes seen as well [115]. Hence, the most popular metric of thermal dose is currently $\mathrm{CEM}_{43\,^\circ\mathrm{C}}\ T_{90}$.

While Definition 3.3 is intuitively appealing, it should be noted that it is not mathematically rigorous and does not provide a solid basis for working with T_n descriptors in all thermal dose calculations. To remedy this, a more rigorous definition of T_n descriptors is developed in Appendix C using measure theory.

Limitations of Thermal Dosimetry

Although thermal dosimetry—and particularly $\mathrm{CEM}_{43\,^\circ\mathrm{C}}\ T_{90}$—is currently the most widely used method of quantifying HIFU-induced cell death [5, 32, 84, 92, 105–111], many weaknesses exist with this technique; the most important of these are detailed in the following list.

Lack of validation at ablation-relevant temperatures. During HIFU exposures, temperatures of up to 100 °C can be achieved in the focal region. However, the widely employed $\mathrm{CEM}_{43\,^\circ\mathrm{C}}$ metric (with the approximate formula for R in Equation 3.7) has only been validated for temperatures up to 54 °C. The situation with other thermal dose metrics mentioned earlier is also similar: for example, the two-state model has only been validated up to 60 °C, while the commonly used values of activation energy in the Arrhenius model may also change at higher temperatures if a different chemical reaction comes to dominate the damage process [31, 102, 116]. This lack of validation potentially undermines the accuracy of the aforementioned thermal dose metrics, and is challenging to address because of the difficulty in obtaining an object-

ive measure of HIFU-induced cell death following high-temperature ablation. The experimental work described in Chapter 5 aims to address this problem.

Different damage thresholds *in vivo* and *in vitro*. Past work has shown that the threshold of heat-induced cell death is often lower *in vivo* than it is *in vitro* [117]. This difference makes it difficult to determine the appropriate thermal dose thresholds for tissue ablation without doing *in vivo* testing. The lower threshold *in vivo* may be caused by the fact that in tissue, the deposited heat will also damage blood vessels, which will in turn severely restrict blood flow to the nearby cells and deprive them of nutrients and oxygen [4, 84]. This does not occur *in vitro*, since cells cultivated outside of tissue are usually surrounded by a growth medium of some kind, instead of depending on a fresh supply of blood for nutrition and respiration.

Does not account for thermotolerance. Analogously to the manner in which vaccines confer disease immunity, cells can also gain thermotolerance if pre-exposed to short bursts of heating [84, 94]. An example of this phenomenon is the generation of heat shock proteins (HSPs) when a cell is exposed to mild thermal stress [4, 84, 89, 90]. None of the thermal dose models mentioned previously accounts for thermotolerance. In HIFU ablation, this problem can be circumvented if the required thermal dose is delivered in a single exposure that is sufficiently long, in which case the temperature will increase monotonically and thermotolerance will not have a chance to develop.

Variation of thermal damage thresholds across cell lines. In general, different cell lines can have dramatically different tolerances to heat [112]. This

means that any thermal dose model must contain at least one adjustable parameter, which is not the case when the $\mathrm{CEM}_{43\,^{\circ}\mathrm{C}}$ metric is used with a fixed value of R (as in Equation 3.7). The dependence of thermal dose on the cell line is also problematic in the case of metastatic cancer, because the tumour may be formed from a different cell line than the surrounding tissue, or may even comprise multiple cell lines. Hence, if the treatment plan calls for ablating both the tumour as well as a safety margin of normal tissue around it, the appropriate thermal dose thresholds may differ considerably in each of these two regions.

Does not account for mechanical effects. By its very definition, thermal dose does not account for non-thermal damage to cells, such as the mechanical damage that can be caused by inertial cavitation (as discussed in Section 2.2.3, page 35). Perhaps the most extreme example of a HIFU ablation technique for which thermal dose would be an inadequate damage descriptor is histotripsy, in which high peak negative pressures are used to cause inertial cavitation and break the target tissue into small, subcellular debris without causing any thermal damage [118]. This limitation will also be illustrated by the experimental work described in Chapter 5.

Dependence on thermometry. Again by definition, thermal dose requires knowledge of the temperature history of the heated sample. Hence, a monitoring approach based on thermal dosimetry can only satisfy the effectiveness criteria in Section 3.1 if the method used to monitor temperature also meets these criteria. This is usually not a problem *in vitro*, where often inserting a

thermocouple into the heated sample is an expedient way of obtaining thermometry during heating. However, as will be discussed in Section 3.4.3, obtaining thermometry *in vivo* is a much more difficult task, and currently none of the methods available for doing so meet all of the criteria in Section 3.1.

While the first three limitations in this list could potentially be addressed with more research and better thermal dose models, the last three items listed will always be inherent limitations of thermal dosimetry. For this reason, alternative measures of heat-induced damage have been developed for tissue; these are described in the next section.

3.4 Tissue Necrosis

3.4.1 Overview

Since HIFU ablation ultimately seeks to ablate solid tumours in organs such as the liver, kidney, and pancreas, soft tissue is by far the most relevant medium to develop HIFU treatment monitoring approaches for. As mentioned previously, soft tissue is mainly composed of cells, vasculature, and the extracellular matrix. Compared to proteins and cells, biological tissue presents several additional challenges with respect to treatment monitoring, not least of which is the significant variability between tissues from different individuals, tissues from different organs, and even different parts of the same piece of tissue. The mechanisms by which HIFU causes damage in tissue are also more complex; detailed reviews of these are available in the works by Barnett et al. [119], Bailey et al. [10], and Baker et al. [120]. On the other hand, the extra components in soft tissue provide additional indicators

of HIFU-induced damage that may be exploited for monitoring purposes. As will be shown throughout this section, many of these indicators are based on changes in various mechanical properties of tissue, such as viscoelasticity and speed of sound.

A detailed review of the methods available for monitoring tissue damage during or following HIFU ablation may be found in the work of Rivens et al. [11]. Early proposed metrics of HIFU-induced damage include total energy deposition [95–99, 121] (see Equation 2.25, page 44) as well as the "mechanical index" proposed by Apfel and Holland [60] (defined as P^2/f, where P is the peak negative pressure and f is the HIFU frequency). Currently, most of the available techniques for monitoring HIFU ablation in tissue may be classified into three general categories: firstly, methods based on thermal dosimetry, for which the additional challenge is obtaining real-time thermometry; secondly, direct physical indicators such as histology and blanching; and finally, techniques based on acoustics [12]. This section discusses each of these categories in turn. However, prior to this, an overview of the theory and modelling of heat deposition in tissue is provided next.

3.4.2 Modelling Heat Deposition in Tissue

The dynamics of heat deposition in tissue are governed by the various sources and loss mechanisms of thermal energy at the treatment site. Not surprisingly, the main source of thermal energy during HIFU ablation is the acoustic energy in the HIFU wave itself: other sources of thermal energy, such as the heat generated by metabolic processes, are usually negligible in comparison. If the HIFU wave is assumed to be planar (as in Equation 2.7, page 22), it can be shown that the acoustic power

transferred to the tissue per unit volume is

$$Q_{\text{acoustic}} = 2\alpha I \tag{3.10}$$

where α the local attenuation coefficient (see Section 2.1.7, page 27) and I is the local, time-averaged acoustic intensity (see Section 2.3, page 41) [35, 36]. Equation 3.10 assumes that the dominant mechanism of acoustic wave attenuation is viscous absorption; as stated earlier in Section 2.1.7, this is usually the case at the pressure amplitudes encountered in HIFU ablation.

Meanwhile, the two most important mechanisms by which thermal energy is lost from the treatment site are heat conduction and blood perfusion (via convection in the latter case). Heat conduction losses arise from the second law of thermodynamics, which states that heat will spontaneously flow from a hotter body to a colder one when the two are placed in contact; for this reason, heat will tend to flow away from the treatment site during ablation. The losses caused by heat conduction can be obtained using the Fourier heating law, which may be stated as

$$Q_{\text{conduction}} = -K_{\text{tissue}} \nabla^2 T \tag{3.11}$$

where K_{tissue} is the thermal conductivity of the tissue (SI units of W m^{-1} °C^{-1}). On the other hand, modelling the effect of blood perfusion is complicated by the variation in vasculature between different tissues or even between two parts of the same tissue. Many bioheat transfer models have therefore been developed to account for the effect of blood perfusion [4]. In hyperthermia and HIFU, the most widely

used model is the one proposed by Pennes [122]:

$$Q_{\text{perfusion}} = w\rho_{\text{blood}}C_{\text{blood}}(T - T_{\text{normal}}) \tag{3.12}$$

where w is the blood perfusion rate (i.e. the volume of circulating blood per volume of tissue per unit time), ρ_{blood} is the mass density of the blood, C_{blood} is the specific heat of the blood (SI units of J kg^{-1} $^{\circ}\text{C}^{-1}$), and T_{normal} is the blood temperature outside of the heated area (i.e. the blood temperature in the arteries; typically 37 °C). The thermal losses caused by blood perfusion are usually higher in cancer tumours than in normal tissue because of the additional vasculature present in the former [14].

By combining all of the information mentioned so far, a governing equation for the dynamics of heat deposition in tissue can be obtained. Specifically, this can be done by observing that the thermal energy absorbed by the tissue at the treatment site is simply the difference between the deposited energy and the lost energy:

$$Q_{\text{absorbed}} = Q_{\text{gained}} - Q_{\text{lost}} = Q_{\text{acoustic}} - Q_{\text{conduction}} - Q_{\text{perfusion}}. \tag{3.13}$$

The rate at which the temperature of the tissue rises over time as a result of the energy it has absorbed is given by the well-known formula

$$Q_{\text{absorbed}} = \rho_{\text{tissue}}C_{\text{tissue}}\frac{\partial T}{\partial t} \tag{3.14}$$

where ρ_{tissue} and C_{tissue} are respectively the mass density and specific heat of the tissue (compare also to Equation 3.12). Substituting Equations 3.10, 3.11, 3.12, and 3.14 into Equation 3.13 yields the following governing equation for heat deposition in tissue:

$$\rho_{\text{tissue}} C_{\text{tissue}} \frac{\partial T}{\partial t} = K_{\text{tissue}} \nabla^2 T - w \rho_{\text{blood}} C_{\text{blood}} (T - T_{\text{normal}}) + 2\alpha I_{\text{SPTA}}. \tag{3.15}$$

This equation is often solved numerically [105, 107], although in some cases analytical solutions can also be obtained [123–125].

Equation 3.15 is typically used in simulations or theoretical work to obtain the temperature profile throughout the medium. However, in clinical scenarios, the temperature profile—if it is required—must be monitored throughout the treatment. To this end, methods of measuring tissue temperature during HIFU ablation are discussed next.

3.4.3 Thermometry and Thermal Dosimetry

Since the goal of HIFU ablation is primarily to kill cancer cells, the methods of thermal dosimetry described previously in Section 3.3.3 (page 65) are also applicable to tissue. However, whereas the required thermometry is usually relatively simple to obtain *in vitro*, temperature measurements *in vivo* present a greater challenge because of the noninvasive nature of HIFU. The three main categories of available temperature monitoring methods are discussed briefly in this section. More detailed discussions of HIFU thermometry may be found in the works by Rivens et al. [11] as well as Arthur et al. [126].

Invasive Thermometry

Several devices are available for measuring temperature invasively. The most common are small-wire thermocouples (e.g. fine-wire and thin-film needles); other instruments include fibre-optic probes and thermistors. Unfortunately, although many of these devices offer real-time, accurate thermometry at a relatively low cost, their invasive nature negates the main advantage of using a non-invasive therapeutic modality such as HIFU. Moreover, even in situations where invasiveness is not an issue (e.g. in the controlled laboratory testing of *in vitro* and *ex vivo* media), small-wire thermocouples can present additional problems when used to monitor temperature during a HIFU exposure. These include measurement bias due to viscous heating around the thermocouple (caused by relative motion between the surrounding tissue and the wire, since the latter has a higher density than the former). Additionally, in the case of cavitation-enhanced heating (discussed earlier in Section 2.2.3, page 35), the thermocouple needle—as well as the track it creates when inserted—can act as bubble nucleation sites and thereby cause an increase in cavitation activity that would not otherwise occur. Finally, thermocouples can only measure temperature in a relatively small portion of the treated area, resulting in poor spatial sampling of the temperature distribution.

Acoustic Thermometry

Several temperature measurement methods based on pulse-echo ultrasound have been proposed, including echo-shift thermometry [127, 128] and spectral-shift estimation [129]. However, all of these methods have the disadvantage of not being

real time because of their reliance on diagnostic ultrasound. Furthermore, even small displacements in the tissue—for example, those caused by breathing or the heartbeat—can also affect the return time of the echoes and thereby limit the accuracy of the estimated temperature [130]. An additional difficulty with this monitoring method is that, as discussed previously in Section 2.1.5 (page 23), the relationship between speed of sound and temperature is not one-to-one over the entire range of temperatures relevant to HIFU ablation.

MR Thermometry

Magnetic Resonance Imaging (MRI) is a monitoring technique that is versatile and non-invasive. MRI can be used to perform various kinds of monitoring, including contrast imaging, thermometry (described here), and shear-wave elastography (described later in Section 3.4.5).

The underlying physical mechanisms of MRI are complex and are beyond the scope of this work; a detailed explanation of the technique is therefore left to other references, such as the paper by Cline et al. [131]. The essence of the MRI technique consists of detecting the net magnetic field of unpaired protons—usually the nuclei of hydrogen atoms—by aligning their spins to an externally applied magnetic field and observing the relaxation time when the field is switched off. Imaging parameters include the strength of the applied magnetic field, the imaging sequence (e.g. spin echo, fast spin echo), and the image weighting (the most popular functions are designated T_1 and T_2).

Although MR thermometry is currently the gold standard for clinical HIFU treatment monitoring [6, 11, 13, 108, 132, 133], the technology has a number of

important limitations. Chief among these is the high cost of the MRI devices, which are typically priced at millions of dollars each. Moreover, despite this considerable investment, the physics of the technique also gives rise to a fundamental trade-off between the spatial and temporal resolutions of the images (i.e. between accuracy and real-time monitoring). Although the limitations imposed by this trade-off are acceptable for some applications, and despite the fact that technological progress has increased the upper bound on spatiotemporal resolution over the years, MRI still does not satisfy both the real-time and accuracy criteria mentioned in Section 3.3.3 for many HIFU ablation scenarios [11].

Summary of *in Vivo* Thermometry Techniques

As discussed throughout this section, none of the currently available methods of obtaining thermometry meets all of the criteria for effective monitoring listed in Section 3.1 (page 47). Furthermore, even if completely effective temperature monitoring were possible *in vivo*, the additional limitations of thermal dosimetry discussed earlier in Section 3.3.3 would also still need to be overcome. For these reasons, methods that rely on mechanical indicators of tissue damage instead of thermal ones have been proposed. The remainder of this section provides an overview of these monitoring techniques.

3.4.4 Direct Physical Indicators of Tissue Damage

Histology and Cryosectioning

Histology and cryosectioning involve examining thin slices of tissue under a microscope, typically with the help of a staining agent to highlight particular structural

features of interest (for example, hematoxylin and eosin to highlight cell nuclei) [134]. However, histological procedures are invasive, time-consuming, and often yield results that are qualitative rather than quantitative. Moreover, these techniques do not allow damage to be monitored in real time, and require relatively specialised equipment for freezing and staining the tissue.

Stiffness Change and Conventional Elastography

As mentioned previously in Section 2.1.3 (page 16), the stiffness of biological tissue increases as it undergoes permanent thermal damage; in everyday experience, this phenomenon manifests itself during the cooking of protein-based foodstuffs such as meat or eggs. Protein denaturation is widely held to be the primary cause of this stiffening [20], although the underlying mechanism is not completely understood.

The change in tissue stiffness during heating was quantified in a study by Wu et al. [135]. Using MR elastography (a technique that will be described shortly), the authors monitored the shear modulus G (defined previously in Section 2.1.3, page 16) in bovine muscle tissue during heating from 20 °C to 75 °C and subsequent cooling back to 20 °C (Figure 3.5a). The resulting measurements are shown in Figure 3.5b; three regions may be identified on the graph. In Region I, the stiffness decreases as temperature increases, which is thought to correspond to reversible protein denaturation. A transition then occurs at approximately 60 °C, beyond which the tissue stiffens with increased heating; this part of the curve is labelled "Region II," and is thought to correspond to irreversible protein denaturation, aggregation, as well as cell death. Finally, as the tissue is cooled in Region III, the stiffness continues to increase, and the tissue remains stiffer than its original state even after it has

returned to its normal temperature. Stiffness changes that occur in Regions I and III were found to be reversible, while any increase in stiffness within Region II was found to be permanent.

(a) *The temperature profile that the muscle was subjected to.*

(b) *Shear modulus over time during heating according to the temperature profile in Figure 3.5a. The curved arrow in the centre of the plot indicates time.*

Figure 3.5: *The evolution of the stiffness of bovine muscle during heating from 20°C to 75°C and subsequent cooling back to 20°C. Reproduced from Wu et al. [135].*

One relatively simple way of assessing tissue stiffness is to apply an external, compressive force and measure the amount of shear deformation that takes place as a result. The compressive force may be generated using a variety of methods, such as manually applied pressure (palpation), a motor-controlled plate (as in mammograms), as well as ultrasound and MRI (by tracking the displacement of features on the 2-D images). Unfortunately, this simple technique—known as conventional elastography—is not real-time, accurate, or convenient to use during HIFU ablation. However, vibroacoustography and shear-wave elastography allow for more quantitative measurements of tissue elasticity to be obtained non-invasively at the treatment

site; this is accomplished by using ultrasound to generate a localised, compressive force in the area of interest. Vibroacoustography and shear-wave elastography will be discussed later in Section 3.4.5.

Blanching

Another indicator of heat-induced tissue damage is the change in its colour that takes place with irreversible denaturation [81, 136]. This phenomenon is called "blanching," and also manifests itself during the cooking of meat and other protein-based foodstuffs; an example is illustrated in Figure 6.2 (page 142). The exact mechanism underlying blanching is not well understood, but is likely to be similar to the one that underlies the change in opacity of protein-embedding hydrogels (see Section 3.2.2, page 54 as well as Chapter 4).

3.4.5 Acoustic Methods

Hyperecho Monitoring

In hyperecho monitoring, diagnostic ultrasound is used to obtain 2-D images of the targeted tissue after each HIFU exposure. The target area is deemed to have been sufficiently treated when hyperechogenic regions ("bright-ups") appear on the images [2, 137–139], as shown in Figure 3.6.

Although hyperecho monitoring is one of the two techniques that are currently used clinically (the other being thermal dose monitoring using MR thermometry) [6, 140], it has the drawback of not being truly real time. This is because it is not possible to distinguish low-intensity diagnostic signals while simultaneously applying high-intensity therapeutic ultrasound, which means that the HIFU must be switched

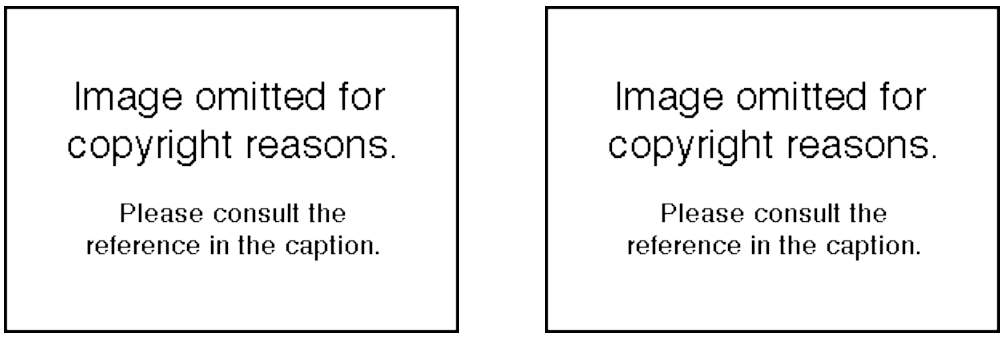

(a) *Before treatment (no hyperecho).* (b) *After treatment (with hyperecho).*

Figure 3.6: *Appearance of hyperechogenic regions in 2-D diagnostic ultrasound images of a cancer tumour exposed to HIFU. Reproduced from Wu et al. [6].*

off during imaging. Moreover, it has been shown that the hyperechogenic regions are in fact caused by the thermally driven formation of large bubbles, most likely as a result of tissue boiling [48, 53, 139]. Studies have found that acoustic cavitation usually occurs before boiling does [138, 141], and that by the time the stable vapour bubbles associated with this boiling appear, damage may have already occurred in parts of the tissue that are located closer to the HIFU source and outside the confines of the intended target area [142]. Hence, the hyperecho monitoring technique relies on overtreating the tissue, which not only lengthens treatment time, but may also adversely affect healthy tissue in the process and thereby compromise treatment safety.

Measurement of Acoustic Properties

In addition to speed of sound, many other acoustic properties of tissue change when it is irreversibly damaged. These include the attenuation coefficient (see Section 2.1.7, page 27), the amount of backscatter from pulse-echo ultrasound, and the coefficient of nonlinearity (see Section 2.2.1, page 32) [13, 31, 143, 144]. However, as with hyperecho monitoring, none of these properties can be tracked in real time since

diagnostic ultrasound is required to measure them. Moreover, questions regarding the accuracy and sensitivity of these measurements remain, although the attenuation coefficient in particular has shown some promise with respect to accuracy and sensitivity [11].

Vibroacoustography and Shear-Wave Elastography

As discussed previously in Section 3.4.4, elastography consists of measuring the amount of shear deformation that takes place in a medium as a result of an applied compressive force. In conventional elastography, this force is applied externally to a relatively large portion of the surrounding tissue; however, using ultrasound, it is possible to generate the compressive force locally and non-invasively, and hence obtain a local measure of the resulting tissue displacement. As mentioned earlier in Section 2.1.2 (page 14), dividing the applied stress by the resulting strain yields the elastic modulus, making it possible to obtain a localised measurement of tissue stiffness.

Two promising techniques that allow localised elastography are Acoustic Radiation Force Impulse imaging (ARFI) [145] and Harmonic Motion Imaging (HMI) [110]. In the former technique, the axial acoustic pressure over time takes the form of a square wave, while in the latter case the applied stress is sinusoidal; hence, both ARFI and HMI are types of vibroacoustography. Real-time versions of these methods are also possible if the HIFU signal is modulated with the functions just mentioned (a square wave for ARFI and a sinusoid for HMI), although doing this reduces the power in the HIFU wave compared to the normal case without modulation. Maleke and Konofagou [110] have implemented amplitude-modulated HMI

and have named the real-time version of the technique HMIFU (HMI for Focussed Ultrasound). Although no studies exist that demonstrate real-time ARFI, a setup similar to the one for HMIFU could be used to implement it.

While vibroacoustography is convenient, inexpensive, and can be implemented in real time, the resulting stiffness maps are currently more qualitative than quantitative and also have limited spatial resolution [146]. However, it is also possible to use the longitudinal ultrasound waves to generate shear waves in the region of interest, as described earlier in Section 2.1.3 (page 16). By monitoring these shear waves, it is possible to infer the shear modulus G and viscosity η in real time using the method described by Vappou et al. [146] as well as Chen et al. [147]. Shear-wave versions of ARFI and HMI are currently being developed, in addition to a technique known as Supersonic Shear Imaging (SSI) [148]. However, while shear wave elastography offers the possibility of real-time, accurate, and convenient monitoring, the ultra-fast imaging devices needed to obtain the required framerates are relatively expensive at present (typically around one hundred thousand dollars). This cost range is an improvement over MRI devices, but is still high enough to potentially limit the clinical adoption of the technology in the near future.

3.5 Objectives and Contributions of This Work

In this chapter, methods for monitoring thermal and mechanical damage in proteins, cells, and tissue were discussed. Each of these methods was assessed according to the criteria described in Section 3.1; the results of this assessment are summarised in Table 3.1. It should be noted that in some specific applications, performance marked

as inadequate in this table may actually be satisfactory: for example, during prostate ablation, MR thermometry devices can acquire adequate temperature measurements in near real time because a high spatial resolution is not necessary. However, the summary assessment in Table 3.1 is intended to cover a broad range of scenarios involving HIFU-induced heating.

		Method	Real-Time	Accurate	Convenient	Low-Cost
Proteins (*in vitro*)		Hydrogel opacity	✓	?	✓	✓
		Structural analysis (UV/VIS, DLS, SEC, FTIR)	✗	✓	✗	✗
Cells (*in vitro*)		Assays	✗	✓	✗	✗
		Thermal dose (Arrhenius, CEM, two-state)	✓	?	✓	✓
Tissue (*in vivo* and *ex vivo*)	Thermal Dosimetry	Invasive thermometry	✓	✓	✗	✓
		Ultrasound thermometry	✗	✗	✓	✓
		MR thermometry	Trade-off (one but not both)		✓	✗
	Direct Physical Indicators	Histology	✗	✓	✗	✗
		Stiffness change and conventional elastography	✗	✗	✗	✓
		Blanching	✗	✓	✗	✓
	Acoustic Methods	Hyperecho	✗	✗	✗	✓
		Acoustic property tracking	✗	✗	✓	✓
		Vibroacoustography and radiation force elastography	✗	✗	✓	✓
		Shear-wave elastography	✓	✓	✓	✗

Table 3.1: *Summary of the efficacy of the treatment monitoring methods discussed in this chapter, based on the criteria described in Section 3.1 (page 47). See the relevant parts of Sections 3.2 through 3.4 for a detailed justification of each rating.*

In the case of protein-embedding hydrogels, Table 3.1 shows that hydrogel opacity could potentially provide effective monitoring of HIFU-induced damage. However, the underlying physical mechanisms and biological relevance of this metric are not fully understood, and hence the accuracy of the optical metric is unclear.

Similarly, thermal dosimetry is also lacking validation at ablation-relevant temperatures (above 54 °C), but would also provide an effective means of monitoring HIFU-induced damage in cells if validated. Finally, with respect to monitoring HIFU-induced damage in tissue, Table 3.1 shows that none of the available techniques provides completely effective monitoring. Furthermore, only a limited number of these monitoring techniques can be operated during HIFU exposure and without the need for interlacing with the HIFU pulse. Recent advances—including enhancements in MRI thermometry [11, 108] as well as improvements in shear wave elastography [110, 148, 149]—show promise for advancing the state of real-time HIFU treatment monitoring. Nevertheless, there remains an unmet clinical need in this area [1, 12, 13], and any successful monitoring approach is likely to involve multiple detectors working in concert rather than a single one operating on its own.

All of the aforementioned limitations in HIFU treatment monitoring hamper the effectiveness and clinical adoption of HIFU ablation. Currently, approximately 5 hours are required to ablate a 30 cm^3 liver tumour using HIFU, but only 2 hours are needed to resect this tumour with invasive surgery. The development of effective monitoring techniques is essential to helping to close this gap. This work therefore seeks to address many of the limitations of HIFU treatment monitoring mentioned throughout this chapter, thereby enabling it to be used in more clinics and with greater effectiveness. Specifically, the primary objective of this work is as follows:

Develop improved metrics of HIFU-induced biological damage that are specifically suited to monitoring and controlling HIFU ablation.

In Chapter 4, an optical method that enables the straightforward quantification of thermal damage in protein-embedding hydrogels is developed. Protein analytic techniques are used to establish the physical mechanisms that link heat-induced protein damage at the microscopic scale to a bulk change in opacity at the macroscopic scale. The optical metric of damage is also shown to be biologically relevant by comparing its value to the degree of damage sustained by cancer cells across a range of HIFU-relevant temperature profiles. However, even in this simple model, the amount of protein damage is found to be dependent on the maximum temperature reached as well as the rate of heating.

The findings of Chapter 4 imply that the reaction kinetics describing heat-induced damage in biological systems can be temperature-dependent. However, many of the available models for quantifying heat-induced cell death have only been verified for mild hyperthermia (i.e. temperatures up to approximately 54 °C). This motivates the experiments described in Chapter 5, in which hydrogels embedded with different cancer cell lines are used to obtain an objective assessment of the performance of multiple temperature-based models of cell death across a range of HIFU-relevant conditions. It is shown that, although these models can be made to work in a specific temperature range and for a specific cell line, the amount of cell death caused by a given temperature profile varies across cell lines in general. Moreover, it is also confirmed that the mechanically induced cell death neglected by these models can greatly undermine their accuracy in certain regimes, such as those that cause high levels of inertial cavitation.

The results of Chapter 5 show that damage models based solely on temperature are unable to provide a complete description of HIFU-induced damage in tissue, which can be comprised of multiple cell lines in the case of metastatic cancers. Moreover, amongst the other available metrics of tissue damage that are independent of cell line, many do not operate in real time or require interlacing with the HIFU pulse, as discussed earlier in Section 3.4. Hence, Chapter 6 focuses on the development of a novel, passive acoustic technique designed for monitoring HIFU-induced tissue damage in real time. Over 200 HIFU exposures were performed in freshly excised ox liver across a range of insonation durations and acoustic intensities. The results indicate that the successful formation of HIFU lesions in *ex vivo* ox liver is highly correlated with the presence of pronounced dips in the magnitude of the acoustic emissions from the HIFU focus at integer multiples of the insonation frequency. A detector based on this observation predicted lesioning with over 80% accuracy in regimes that were very likely to create lesions (60 J of energy or more), and had an error rate of less than 6% for exposures that were too short to cause lesioning (up to 1 s long). The overall sensitivity and specificity of the detector were 75.6% and 74.2%, respectively. The detector proposed in Chapter 6 could therefore provide a low-cost means of effectively monitoring clinical HIFU treatments passively and in real time.

Chapter

4

Optical Measurement of Damage in Protein-Embedding Hydrogels

In controlled laboratory studies of hyperthermia and thermal ablation, translucent hydrogels containing embedded proteins such as BSA are often used as tissue-mimicking materials owing to the increase in their opacity that takes place as they accumulate heat damage. In this chapter, an optical method that enables the straightforward quantification of thermal damage in these hydrogels is developed by using the protein analytic techniques described in Section 3.2 (page 50) to establish the physical mechanisms that link the optical metric of thermal damage with quantifiable damage to the proteins embedded in the gel. The optical damage metric is also shown to be biologically relevant by comparing its value to the damage sustained by cancer cells across a range of temperature profiles. The results in this chapter show that BSA hydrogels provide a simple physical model for quantifying biologically relevant heat damage in real time during controlled laboratory studies of hyperthermia and thermal ablation.

4.1 Motivation and Objectives

As mentioned previously in Section 3.2.2 (page 54), protein-embedding hydrogels are commonly used in laboratory "bench-top" testing of thermal ablation, and have the desirable property of becoming increasingly opaque following heat-induced denaturation of the embedded proteins. Although this property allows for the real-time, convenient, low-cost monitoring of thermal damage in these materials using an optical metric, the biological relevance and the underlying physical mechanisms of this metric are not well understood. This potentially hinders the efficacy of opacity-based monitoring in protein-embedding hydrogels.

This chapter aims to demonstrate that the opacity of protein-embedding hydrogels is an accurate, biologically relevant measure of heat-induced protein damage. Specifically, the objectives of this chapter are as follows:

- Establish a correlation between macroscopically observable variations in the opacity of BSA hydrogel and the amount of heat-induced changes occurring in the microscopic, molecular structure of the proteins;
- Determine the biochemical mechanisms that underlie the optical change, thereby providing a physical justification for the use of opacity as a proxy metric of thermally induced BSA denaturation;
- Establish a correlation between thermally induced cell death in a human cancer cell line and the opacity of BSA polyacrylamide hydrogel across a range of temperature profiles, thereby demonstrating that the optical measure of thermal damage is biologically relevant; and

- Investigate the amount of heat-induced protein damage that occurs at target temperatures relevant to HIFU ablation (50 °C to 100 °C).

4.2 Experimental Methods

4.2.1 Protein Structural Analysis

Three of the protein analytic techniques described earlier in Section 3.2.3 (page 55) were used to characterise samples of BSA (Sigma-Aldrich, A7906, Gillingham, Dorset, UK) that were dissolved in water and subjected to pre-set temperatures for a fixed time of 30 minutes. This approach allows the thermal characteristics of BSA to be studied separately from the other substances in the hydrogel. Firstly, turbidity analysis with UV/VIS spectroscopy was used to determine the relative amount of insoluble BSA protein aggregates in the samples. Secondly, SEC was performed to determine the relative content of BSA monomer and soluble protein aggregates in each sample. Thirdly, FTIR was employed to study the changes in the secondary structure content of the BSA protein molecules (as mentioned earlier in Section 3.2.1, page 50, heat-induced denaturation does not normally affect the primary structure of proteins). In all cases, the concentration of the BSA solutions were chosen such that measurable changes in the observed phenomena could be detected without saturating the devices used to perform the measurement.

Ultraviolet/Visible Spectroscopy

The aim of the UV/VIS technique is to measure the amount of insoluble BSA aggregates (i.e. precipitates) that form at different temperatures. Turbidity analysis was

performed on a Cary 50 Bio UV/VIS spectrophotometer with a single-cell Peltier temperature control element (Varian, Yarnton, Oxfordshire, UK). A 3 mL quartz cuvette was filled with 3.5% (w/v) BSA solution that had been prepared by dissolving the protein in double-distilled and filtered (0.2 µm) water. The samples were heated from room temperature to steady-state temperatures of 25 °C, 40 °C, 50 °C, 60 °C, 70 °C, 80 °C, and 90 °C for a duration of 30 minutes using the built-in Peltier element, and were continuously stirred throughout the heating. In all cases, the temperatures of the samples rose to within 1 °C of their steady-state values within 2 minutes or less.

During the heating procedure, turbidity was measured at 350 nm. This value was selected because of the relatively low absorbance of BSA at this wavelength [150] and also because 350 nm is a common choice in turbidity analyses reported in the literature [72, 151]. The temperature inside the cuvette was monitored using a Type T needle thermocouple (Omega Engineering, HYP0, Stamford, Connecticut, USA) connected to a temperature data logger (Pico Technology, Pico TC-08, Cambridge, Cambridgeshire, UK). The baseline value of 100% transmittance was set with the cuvette containing only distilled water. SEC was performed on the heat-treated samples immediately after the 30-minute heating period. Turbidity was also measured 24 h after heating to check for any reversible changes in protein denaturation.

Size Exclusion Chromatography

The SEC technique is used to quantify the amount of soluble aggregates present in each heated sample. The HPLC apparatus used in this study consisted of a

Prostar 210 dual-pump solvent delivery system, a Prostar 500 column valve module, a Prostar 325 UV detector, and a Model 410 autosampler (Varian). SEC was performed using a 4.6 mm by 250 mm Zorbax GF250 gel-filtration column (Agilent Technologies, South Queensferry, West Lothian, UK) with a pore diameter of 150 Å and a nominal particle size of 4.0 µm to 4.5 µm. A 20 mM phosphate buffer at a pH of 6.8 with 250 mM NaCl was chosen as the mobile phase. For these experiments, 10 µL samples were taken from each of the solutions that had been heat-treated in the UV/VIS spectrophotometer and were injected into the column with the mobile phase. The flow rate through the column was 250 µL/min under isocratic conditions (single solvent) and the temperature of the column was held constant at 30 °C. UV detection of the eluent was carried out at a wavelength of 280 nm, which corresponds to a local maximum in the absorption spectrum of BSA [152] owing to resonance in its tryptophan amino acid side chains [151]. Absorbance was monitored for 20 minutes following injection, after which peak identification and integration was performed using Galaxie chromatography software (Varian).

Fourier Transform Infrared Spectroscopy

The objective of the FTIR technique is to measure the relative amount of different secondary structure motifs (such as α-helices and β-sheets) as a function of temperature. To this end, a 2% (w/v) BSA solution was prepared in the same manner as described previously. Samples of this solution were then subjected to 25 °C, 40 °C, 60 °C, 70 °C, 80 °C, and 95 °C for 30 minutes by placing them in a preheated water bath and were subsequently centrifuged at 10 000 rpm for 10 minutes to eliminate precipitates. As in the UV/VIS experiment, the temperatures of the samples rose to

within 1 °C of their steady-state values within 2 minutes or less. The FTIR spectra were then collected on a Nicolet Magna 550 infrared spectrometer using a Proteus transmission cell kit (Thermo Fisher Scientific, Limburg an der Lahn, Hessen, Germany) with an optical path length of 6 µm. The instrument was continuously purged with dry air to avoid spectral noise from water vapour. Measurements consisted of 42 averaged scans and were repeated 3 times, preceded on each occasion by the recording of a new background spectrum in order to minimise baseline and temperature effects. Background subtraction was performed to obtain a flat baseline at wavenumbers between 1900 cm^{-1} and 1750 cm^{-1}.

Changes in the secondary structure of the proteins were detected using the baseline-corrected, area-normalised, non-deconvolved Amide I band of the spectrum (1700 cm^{-1} to 1600 cm^{-1}). The positions of the underlying peaks were determined using the second derivative of the spectra and were assigned to secondary structures according to the literature [153]. Quantification was performed by fitting peaks using PeakFit version 4.12 (Systat Software, Erkrath, Nordrhein-Westfalen, Germany) and assuming a Gaussian peak shape. The r^2 correlation coefficient of each fit was at least 0.999. The ratio of the area under a given Gaussian peak to the total area under the curve was then used as a relative measure of how often the secondary structure associated with that peak occurred in the sample, with values expressed as a percentage of the total number of secondary structure motifs that were observed and classified in this manner.

4.2.2 Heat-Induced Cell Death

The aim of this experiment was to measure the amount of thermally induced cell death in a human breast cancer cell line across a range of heating profiles. Cells were grown in RPMI 1640 medium without phenol red (PAA Laboratories, E15-048, Yeovil, Somerset, UK), 10% (v/v) of fetal bovine serum (PAA Laboratories, A15-151) and 25 U/mL of penicillin-streptomycin (Sigma-Aldrich, P4333). ZR75.1 human breast cancer cells were suspended in this medium at a final concentration of 10^6 cells/mL, after which 300 µL samples of this suspension were placed in enclosed microcentrifuge tubes. The samples were heated for 1 minute, starting from room temperature, in mechanically stirred water baths set at 25 °C, 40 °C, 50 °C, 60 °C, 70 °C, 80 °C, and 90 °C (measurement of the internal temperature of the samples themselves will be described shortly). The fraction of surviving cells in each heat-treated sample was then determined using an MTS-based assay kit (Promega, G5421, Southampton, Hampshire, UK) per the instructions from the manufacturer, with absorbance measured at 490 nm after 2 hours of MTS incubation using a Victor 2 plate reader (PerkinElmer, Cambridge, Cambridgeshire, UK).

To determine the temperature profiles that each sample was subjected to, an additional microcentrifuge tube containing 300 µL of cell medium only was included in each heat treatment. The temperature in this tube was monitored using a Type T needle thermocouple (Omega Engineering, HYP0) connected to a temperature data logger (Pico Technology, Pico TC-08). Given that the temperature of the water bath was kept fairly uniform throughout each heat treatment by stirring the water,

the temperature profile measured in the extra tube was taken as representative of the temperature profile experienced by all other samples in the same batch. In all cases, the temperature of the sample rose to within 1 °C of the surrounding water bath within 1 minute of immersion.

4.2.3 Opacity Measurements

Procedure for Manufacturing the BSA Polyacrylamide Hydrogel

Slices of BSA polyacrylamide hydrogels were manufactured according to the procedure described by Lafon et al. [79]. To begin with, trishydroxymethylaminomethane (TRIS) buffer was prepared at a concentration of 1 M and a pH of 8 using TRIS hydrochloride salt (Sigma-Aldrich, T3253) and TRIS base (Sigma-Aldrich, T1503). Next, deionised water was mixed with 100 mM of TRIS buffer and 7% (w/v) of acrylamide (Thermo Fisher Scientific, BPE1406) up to the desired volume of hydrogel. 7% (w/v) of BSA (Sigma-Aldrich, A7906) was then spread atop this mixture and was allowed to dissolve into the liquid by diffusion.

Once all of the BSA had dissolved, 100 mg of ammonium persulfate (APS; Thermo Fisher Scientific, BPE179) and 50 µL of N,N,N',N'-tetramethylethylenediamine (TEMED; Sigma-Aldrich, T7024) per 100 mL of mixture were added to initiate polymerisation. The hydrogels were cast in special moulds that produced uniform slices with a transverse area of 25 cm^2 (5 cm × 5 cm) and a thickness of 5 mm. The gels were allowed to set for 4 hours and were used within an hour of setting.

Experimental Setup for Monitoring Opacity and Temperature During Heating

To obtain hydrogel opacity data for a range of temperature profiles, the water bath setup shown in Figure 4.1 was used to subject each slice of BSA polyacrylamide hydrogel to different peak temperatures (25 °C to 90 °C) for 10 minutes. The setup consisted of a constant-temperature water bath that was heated using a hot plate and was mounted rigidly to an optical test bench. The water bath contained a basket that could be lowered in and out of the bath, and which was notched so that it did not translate or rotate within the bath once in place. The basket itself contained a special mount for the BSA hydrogel slices, in the form of eight rods that aligned with the outer perimeter of the slice. Each of these rods had a pointed tip, which allowed a hydrogel slice to be affixed to the mount by impaling it on the rods, as shown in the three pictures in Figure 4.2a. This design ensured that the top side and the underside of each hydrogel slice were heated by the water, and also kept the slices in a fixed position during heating.

To monitor the opacity of each hydrogel slice during heating, a digital SLR camera (Canon, EOS-400D, Reigate, Surrey, UK) was mounted above the water bath and was used to image the plane of the slices against a matte black background every 5 seconds. Figure 4.2a illustrates the perspective of the camera by showing three sample images from one run of the experiment, arranged as a time-lapse sequence. To prevent steam from clouding the camera lens, a small fan was placed between the water surface and the camera, as shown in Figure 4.1. The camera was set to acquire images in 24-bit colour at a resolution of 3888×2592 pixels, giving a linear pixel density of approximately 450 pixels/cm. The camera was set to operate without a

flash, and the ambient lighting level was kept as consistent as possible across runs. The water level was also kept the same from run to run, so that there was always the same thickness of water in the path between the camera lens and the hydrogel slice.

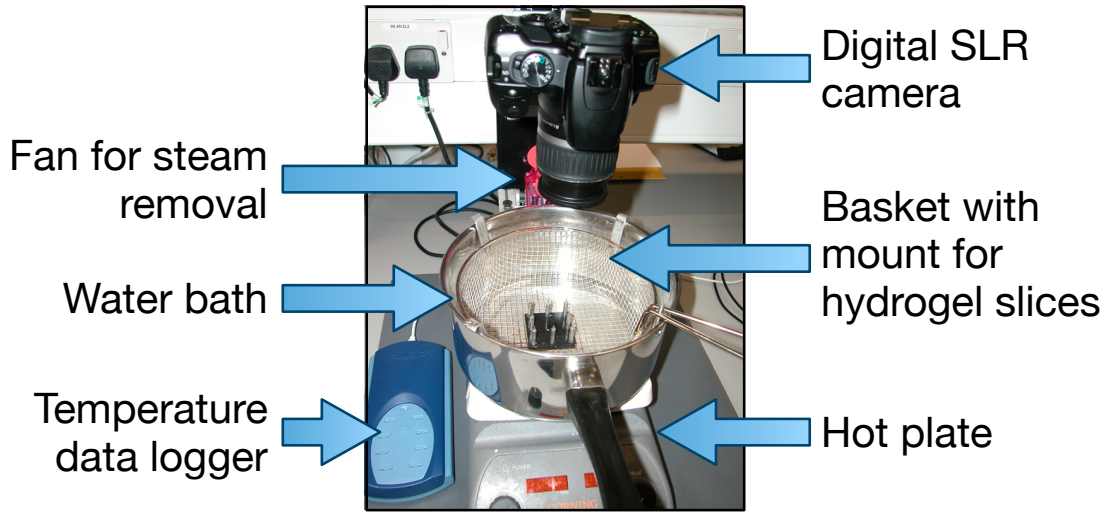

Figure 4.1: *Experimental setup for measuring heat-induced changes in the opacity of polyacrylamide hydrogel with embedded BSA.*

During heating, the *in situ* temperature of each hydrogel slice was monitored every 500 ms with a Type T needle thermocouple (Omega Engineering, HYP0) embedded in the centre of the slice and connected to a temperature data logger (Pico Technology, Pico TC-08). Test runs of the experiment confirmed that the temperature distributions within the slices were fairly even; this occurred because of the small thickness of the slices (5 mm) relative to their transverse area (25 cm^2). In all tests performed, the temperature of the hydrogel rose to within 1 °C of the water bath temperature within 2 minutes or less of heating. The temperature of the water bath was also monitored using a second thermocouple, but was found to remain constant in all runs of the experiment, even after the immersion of a hydrogel slice.

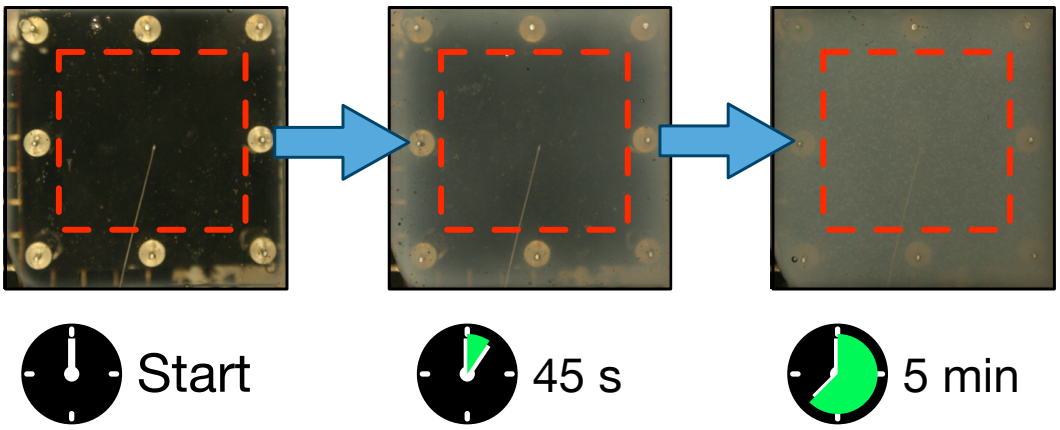

(a) *Time-lapse photographs of BSA hydrogel opacity. The squares indicate the central area of the hydrogel slices in which the greyscale intensity histograms in Figure 4.2b were computed. The inclusion of the thermocouple needle in these areas does not noticeably influence the histograms.*

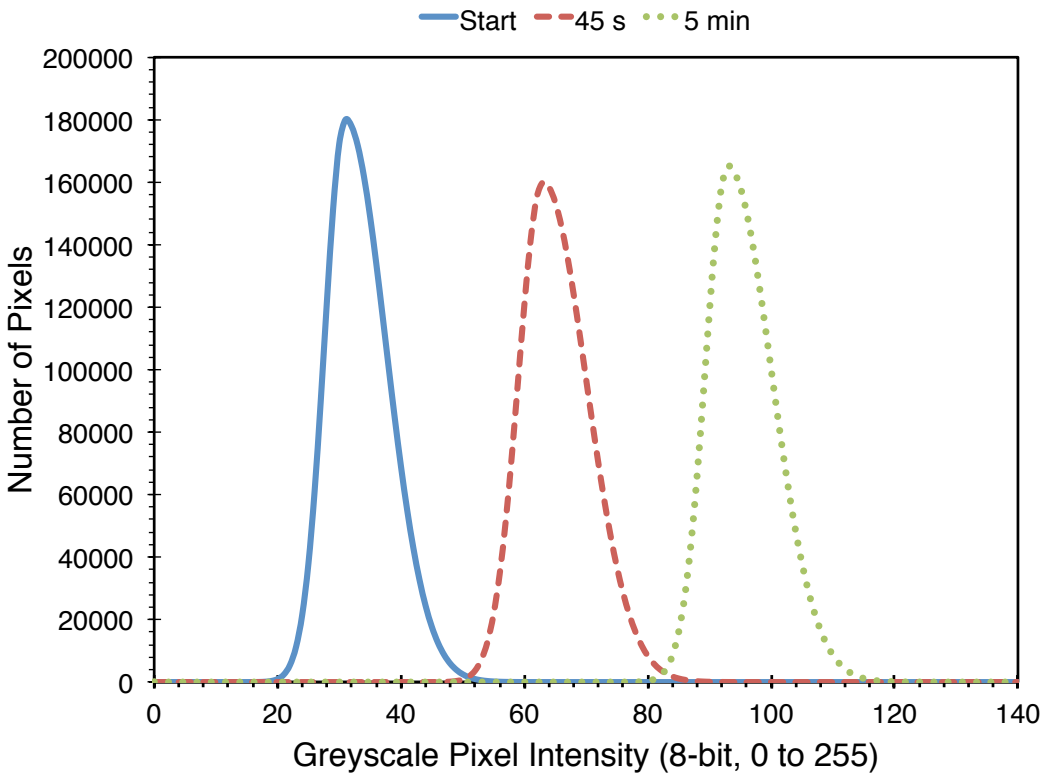

(b) *Greyscale pixel intensity histograms in the central area of the hydrogel slice for each of the photographs in the time-lapse sequence shown in Figure 4.2a. Here intensities of 0 and 255 correspond respectively to black and white.*

Figure 4.2: *Time-lapse photographs and corresponding 8-bit greyscale pixel intensity histograms of BSA polyacrylamide hydrogel in a 78°C water bath.*

Quantifying Protein Denaturation Based on Opacity

An optical metric of the degree of damage sustained by each hydrogel slice during heating was obtained from the photographs of the central area of each slice (outlined with red squares in Figure 4.2a). Because the hydrogel slices were imaged against a matte black background, the greyscale intensity of a given pixel in this area can be taken as a measure of the local degree of whiteness in the hydrogel slice, which is also a measure of its local opacity. This intensity was obtained by taking the average of the intensities of the three colour channels in the image (red, green, and blue). Since the images are in 24-bit colour, each colour channel is quantised at 8 bits per pixel. Hence, the greyscale intensity also has 8 bits of precision, making it possible to distinguish $2^8 = 256$ levels of whiteness (numbered 0 through 255, where 0 is black and 255 is white).

Figure 4.2b shows histograms of the greyscale pixel intensities in the area within the squares shown in Figure 4.2a. In all cases, the histograms were found to be Gaussian in shape, with well-defined means and standard deviations of less than 4% (10 levels). Tests over some randomly chosen images also gave similar results, even in smaller subregions with one-tenth of the area of the squares shown in Figure 4.2a. This confirms that denaturation took place uniformly in each hydrogel slice. For these reasons, the means of the greyscale pixel intensity histograms were used as a relative measure of the amount of denatured protein in each slice. These mean intensities were converted to normalised mean optical transmittance values using an affine transformation, with 100% corresponding to an unheated slice (measured at the start of each run of the experiment) and 0% corresponding to a slice that had

been denatured at 90 °C (the maximum temperature) until its mean pixel intensity had stabilised. The normalised mean optical transmittance $\bar{T}$ associated with a mean greyscale pixel intensity of I is therefore given by

$$\bar{T}(t) = \left(\frac{I_{\max} - I(t)}{I_{\max} - I_{\min}} \right) \cdot 100\% \tag{4.1}$$

where $I_{\min}$ and $I_{\max}$ are the mean intensities associated with the unheated and maximally heated hydrogel slices, respectively.

4.3 Results

4.3.1 Protein Structural Analysis

Ultraviolet/Visible Spectroscopy

Figure 4.3 shows the optical transmittances of the BSA samples after 30 minutes of heating, as measured by turbidity analysis using UV/VIS spectroscopy. Measurements indicate that the turbidity of the solution remains fairly constant up to 60 °C, after which there is a noticeable decline in its optical transmittance. This indicates the existence and increased formation of insoluble aggregates at temperatures above 60 °C; these aggregates act as scatterers of incident light. Additionally, no substantial changes were observed in these results 24 hours after heating, indicating that no reversible denaturation occurred.

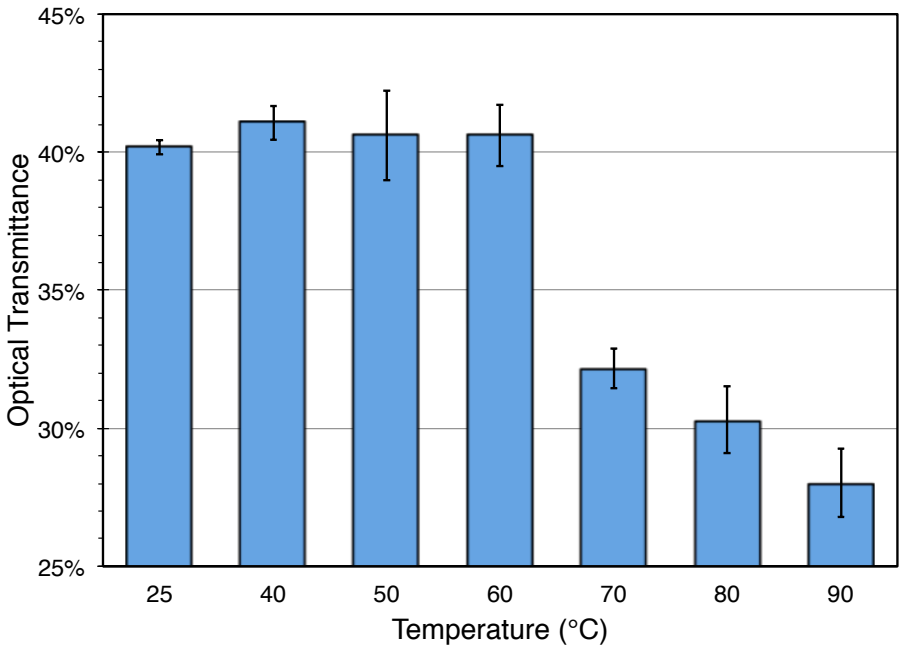

Figure 4.3: *Optical transmittance of 3.5% (w/v) BSA solutions exposed to various temperatures for 30 minutes. The data were obtained using a UV/VIS spectrometer set to 350 nm and with 100% transmittance corresponding to distilled water containing no BSA. The values plotted here are averaged over 3 separate runs of the experiment described in the text. Standard deviations are indicated with error bars.*

Size Exclusion Chromatography

Figure 4.4 shows minutes 6 through 12 of three SEC chromatograms for samples exposed to 25 °C, 70 °C, and 90 °C. Measurements are expressed in Absorbance Units (AU). The absorbance value at all other elution times was below the noise floor of the detector.

The chromatogram for 25 °C BSA (solid line) shows a large peak at a retention time of 9.82 min (1.173 AU), as well as smaller peaks at 9.03 min and 7.57 min (139 mAU and 5.2 mAU respectively). Using a BSA molecular weight standard (Sigma-Aldrich, P7869) with the same SEC method, it was determined that the large peak at 9.82 min corresponds to BSA monomer, i.e. undenatured single BSA

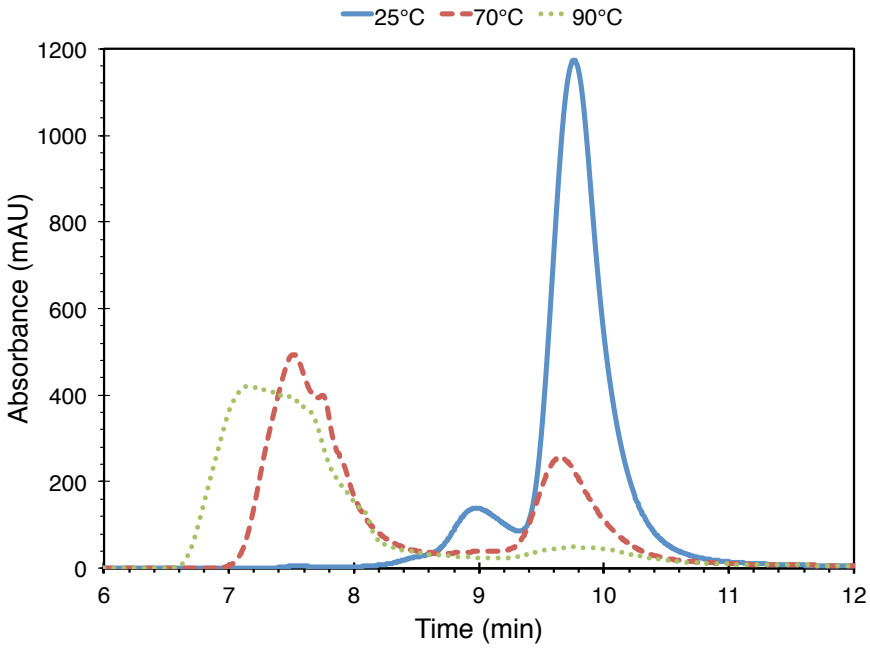

Figure 4.4: *Minutes 6-12 of three SEC chromatograms for 3.5% (w/v) BSA solutions heated to 25°C, 70°C, and 90°C for 30 minutes. Absorbance was monitored at 280 nm. For this run of the experiment, the chromatograms at 40°C, 50°C, and 60°C (not shown) were found to be similar to the 25°C one. Absorbance at all other times was found to lie below the noise floor.*

protein molecules with a molecular weight of 66.4 kDa [154]. The smaller peaks correspond to larger molecular weight aggregates.

The chromatograms associated with the samples treated at 40 °C, 50 °C, and 60 °C (not shown in Figure 4.4) do not vary much from the 25 °C one. However, in the 70 °C case (dashed line), the amplitude of the peak around 7.57 min has increased more than threefold to 494 mAU, while the monomer peak has dropped to 255 mAU, less than a quarter of its value for the sample at 25 °C. This indicates that some of the BSA monomers have aggregated together because of the thermal damage they have sustained. This trend continues in the sample treated at 90 °C (dotted line), in which very little monomer remains (peak value of 49 mAU) and most of the BSA proteins have formed aggregates. The aggregate peak in this chromatogram has a

maximum value of 420 mAU. It is also relatively spread out compared to the results at 25 °C and 70 °C and does not have a Gaussian shape, which indicates that it spans a range of aggregate sizes.

Figure 4.5 shows the relative amounts of monomer and aggregates in all heat-treated BSA samples, as computed by peak integration of their respective chromatograms (as discussed in Section 4.2.1). The figure shows that over 85% of the BSA is monomeric for temperatures less than or equal to 60 °C. However, beyond this threshold, there is a marked rise in the percentage of aggregates. At 80 °C, the distribution is essentially the reverse of the 60 °C one, with 85% of the BSA aggregated.

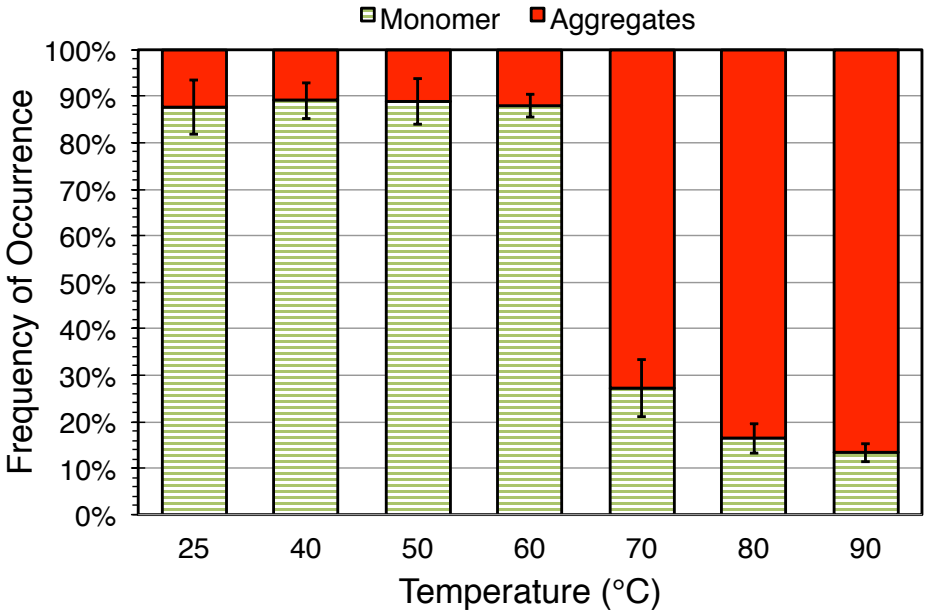

Figure 4.5: *The relative amount of BSA monomers and aggregates in 3.5% (w/v) BSA solution exposed to various temperatures for 30 minutes. The data were obtained by performing peak identification and integration on the associated SEC chromatograms. The values plotted here are averaged over 3 separate runs of the experiment described in the text. Standard deviations are indicated with error bars.*

Fourier Transform Infrared Spectroscopy

Figure 4.6a shows the Amide I band of the FTIR spectra obtained from BSA samples exposed to 25 °C, 70 °C, and 95 °C. The second derivatives of these spectra are plotted in Figure 4.6b. The locations of the fitted peaks for the spectra in Figure 4.6a are given by the zero-crossings in Figure 4.6b, which correspond to inflection points in the spectra.

Fitting peaks to all observed spectra and matching these with secondary structures in the manner described previously yields the data in Figure 4.7, which shows the secondary structure distribution of the heat-treated BSA samples. It should be noted that the values obtained are biased by the fact that the precipitates were spun out during the procedure, thereby enriching the mixture for the relatively undamaged protein. However, this limitation does not affect the conclusions that will be drawn from these results later in this chapter.

In the 25 °C sample, 77.6% of the secondary structure content is α-helix, while 11.6% is intramolecular β-sheet, 1.1% is intermolecular β-sheet, and the remaining 9.7% is comprised of various other secondary structure types (random coils, turns, etc.). These findings are consistent with other studies [151, 155], which report that the majority (60% or more) of the secondary structure motifs in BSA are α-helices.

The secondary structure distribution does not change much from the 25 °C one for temperatures up to 60 °C. However, at and above 70 °C, an increasing number of the α-helices transform into other types of secondary structure, mainly β-sheets.

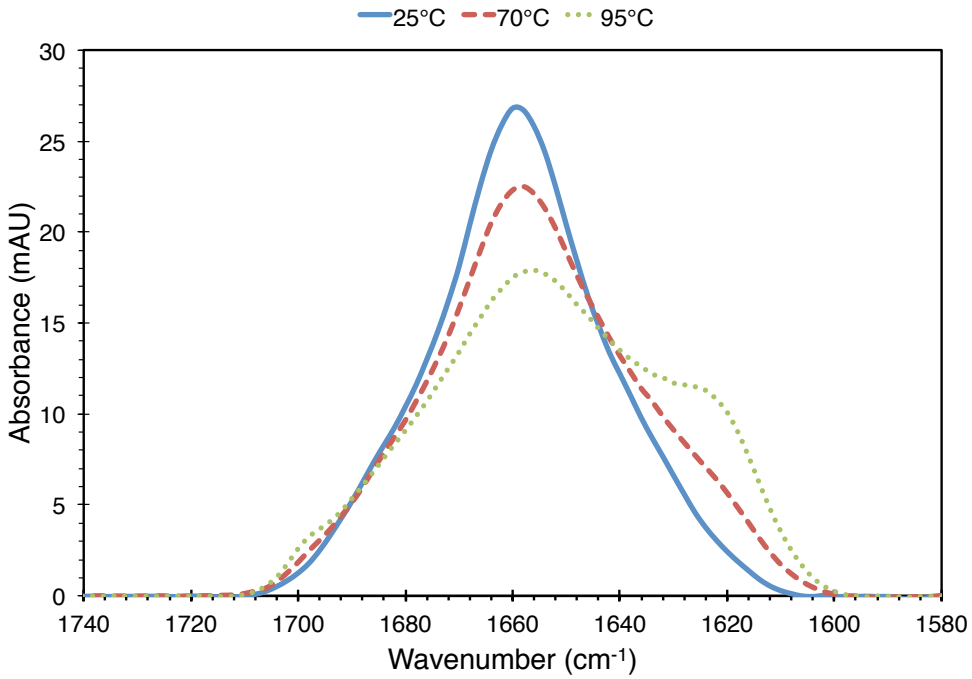

(a) *The FTIR spectra.*

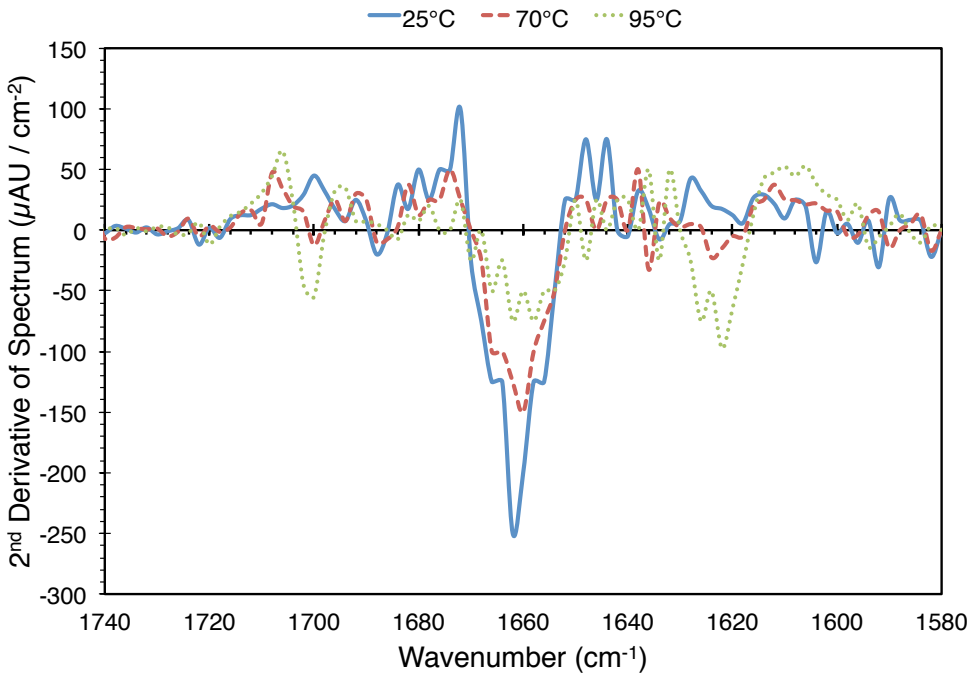

(b) *The second derivatives of the spectra in Figure 4.6a. The zero-crossings of these curves correspond to inflection points in the original spectra, which are used in the peak fitting process as described in the text.*

Figure 4.6: *Examples of FTIR spectra and second derivatives of these spectra in 2% (w/v) BSA solutions heated to 25°C, 70°C, and 95°C for 30 minutes. For this run of the experiment, the spectra at 40°C and 60°C (not shown) were found to be similar to the 25°C one.*

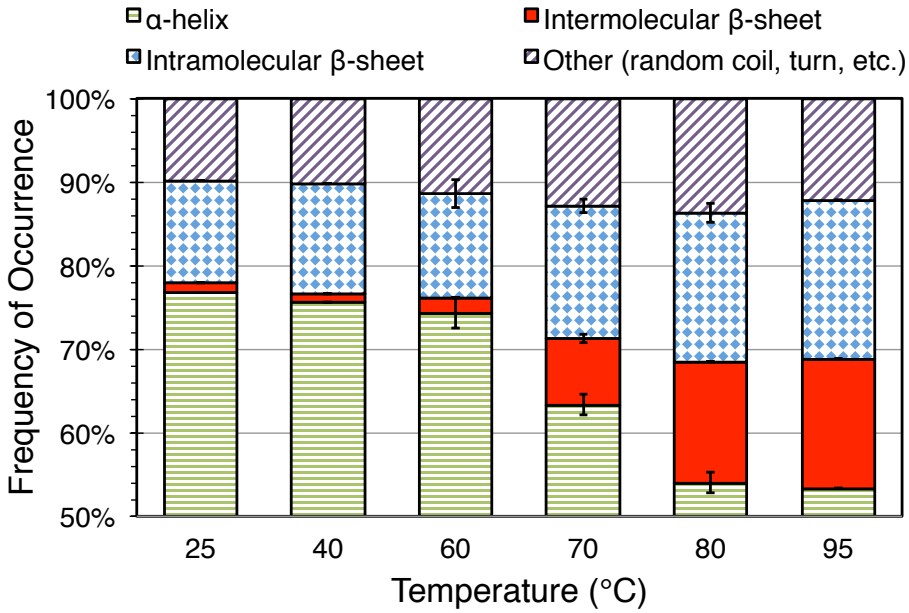

Figure 4.7: *Relative secondary structure distribution of BSA in 3.5% (w/v) solutions heated to various temperatures for 30 minutes. Note that the vertical axis begins at 50%. The data were obtained using a FTIR apparatus. The values plotted here are averaged over 3 separate runs of the experiment described in the text. Standard deviations of more than 0.5% are indicated with error bars.*

Notably, the number of intermolecular β-sheets rises markedly at 70 °C, whereas only a small number are present below this temperature.

In the 95 °C sample, α-helices comprise 53.1% of the secondary structure, while 15.3% is intermolecular β-sheet. Compared to the 25 °C sample, the amount of α-helices has decreased by nearly one-third while the number of intermolecular β-sheets has increased almost 14-fold.

4.3.2 Heat-Induced Cell Death

Figure 4.8a shows the fractions of surviving cells after 1 minute of heating to various target temperatures from 37 °C to 90 °C. The values are plotted as a function of the peak temperature achieved in the sample (which is simply its temperature just

before removal from the water bath). The figure shows that most or all cells survive at temperatures up to 60 °C, but almost none survive at 70 °C and beyond.

4.3.3 Optical Transmittance Measurements

Figure 4.9 shows the normalised mean optical transmittance of two BSA hydrogel slices heated to different target temperatures (70 °C and 85 °C), calculated using Equation 4.1 (page 105). It can be seen in Figure 4.9 that both curves decay towards steady-state values; this behaviour was observed in every run of the experiment. The steady-state optical transmittances from all runs of the experiment are grouped by target temperature in Figure 4.10. It was also found that differences in the steady-state opacities of hydrogel slices that had been heated to different target temperatures persisted even after the slices were cooled back to room temperature, as illustrated in Figure 4.11.

Meanwhile, Figure 4.8b shows the mean optical transmittance of the BSA hydrogel slices after 1 minute of heating for the same range of target temperatures as Figure 4.8a (37 °C to 90 °C). Here again, it can be seen that the mean optical transmittance does not change up to 60 °C, but drops at 70 °C and beyond. The values in Figure 4.8b are similar to the steady-state values shown in Figure 4.10; this is because at 70 °C and beyond, the opacity of the hydrogel typically reaches its steady state value within less than a minute.

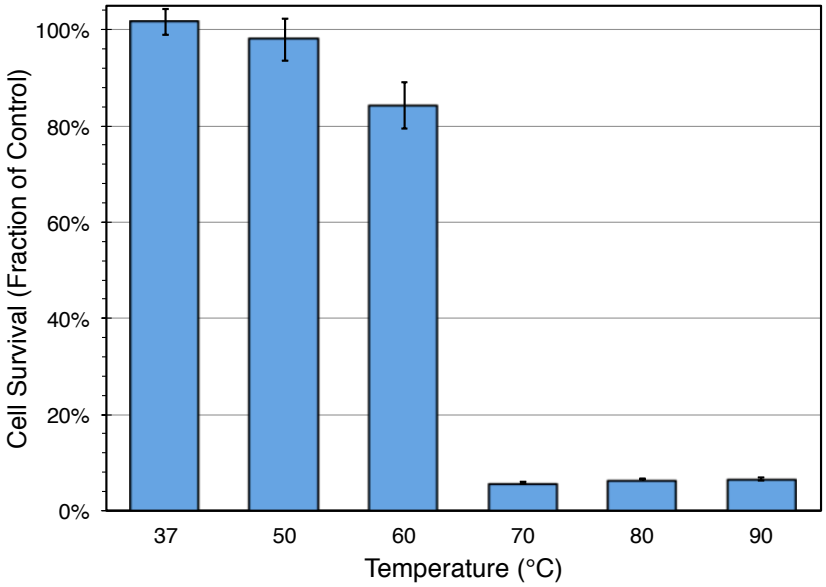

(a) *Survival of ZR75.1 human breast cancer cells after 1 minute of heating, expressed as a percentage of a control sample that was not heated. Cell survival was measured using an MTS assay.*

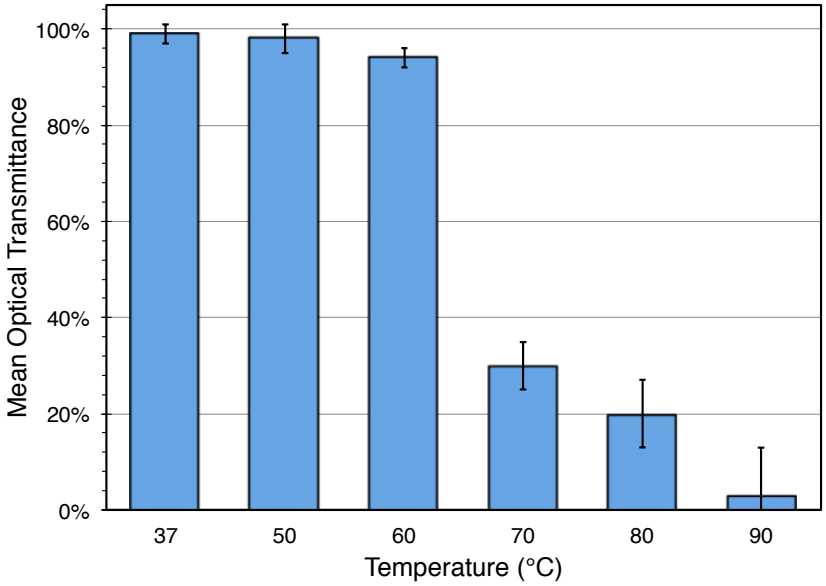

(b) *Normalised optical transmittance of polyacrylamide hydrogel with embedded BSA after 1 minute of heating, normalised to unheated and fully heated control samples as described in the text.*

Figure 4.8: *ZR75.1 cell viability and opacity of BSA polyacylamide hydrogel after 1 minute of heating at various target temperatures from 37°C to 90°C. The temperatures indicated are those of the water bath used to heat the samples, although the internal temperature of the samples themselves had settled to within 1°C of this value by the end of the heating process. The values plotted in both graphs are the means of the results from 3 separate runs of the experiment; standard deviations are indicated with error bars.*

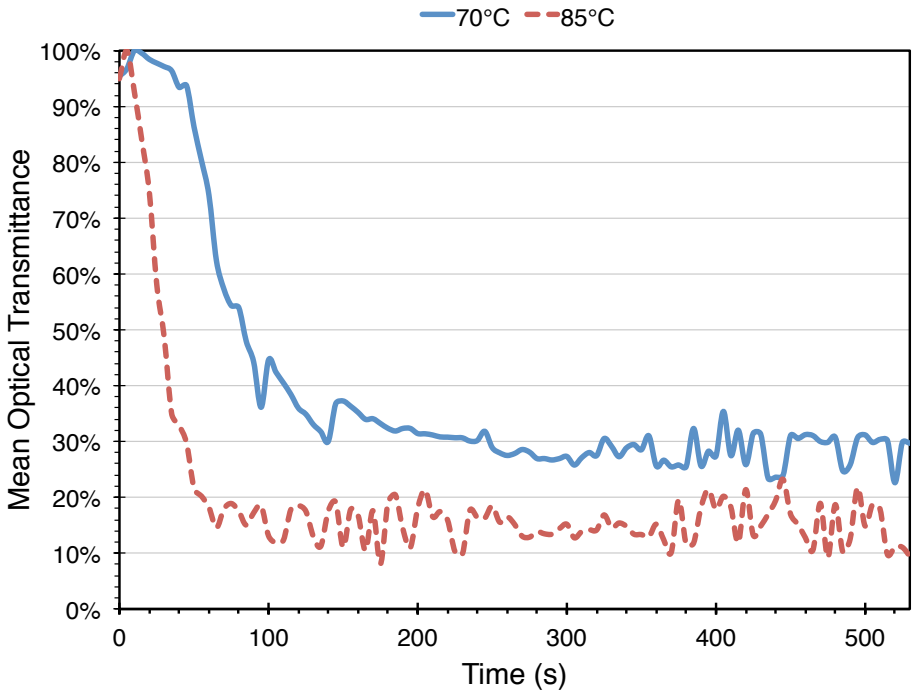

Figure 4.9: *Normalised mean optical transmittance of two BSA hydrogel slices heated to different target temperatures (70°C and 85°C).*

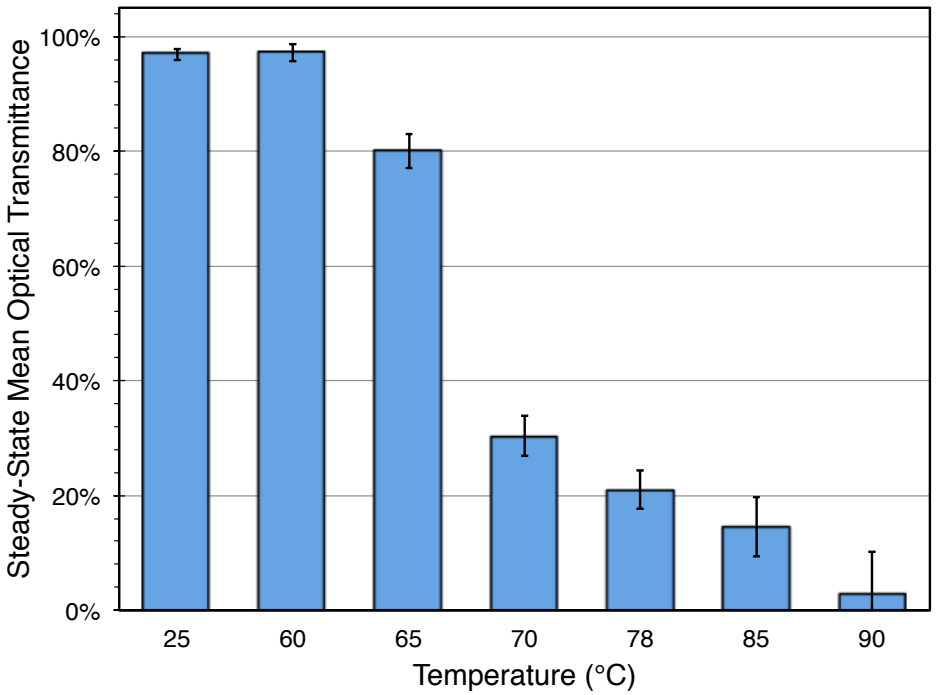

Figure 4.10: *Steady-state mean optical transmittance of BSA hydrogel slices at different target temperatures. Each value is averaged from 3 separate experimental runs; standard deviations are indicated with error bars.*

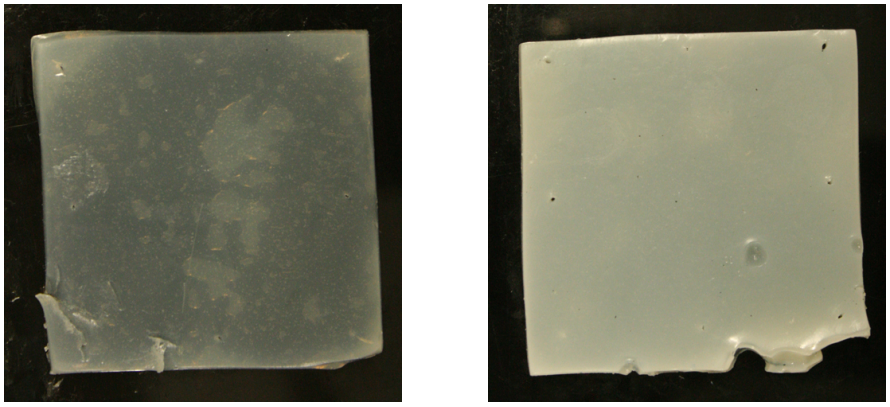

(a) *70°C target temperature.* (b) *85°C target temperature.*

Figure 4.11: *Photographs of the BSA hydrogel slices in Figure 4.9 after heating. The slices were photographed against a matte black background after they had cooled to room temperature.*

4.4 Discussion

4.4.1 Relationship Between Protein Denaturation and Hydrogel Opacity

Taken together, the protein structural analysis findings listed in Section 4.3.1 (page 105) explain the mechanism that links the opacity of BSA hydrogel with thermally induced denaturation of the proteins. The FTIR data in Figure 4.7 show that at the molecular level, an increasing number of the α-helices in the BSA transform into intermolecular β-sheets as the proteins accumulate thermal damage beyond 60 °C. This result also indicates that the BSA proteins are aggregating, because intermolecular β-sheets must be formed between two distinct protein molecules [72, 73] (although it should be noted that, in general, intermolecular β-sheets are not the only means by which proteins can form aggregates). This is confirmed by the SEC data in Figure 4.5, which show that the conversion of BSA monomer into soluble aggregates follows a similar trend to the graph of intermolecular β-sheet formation

against temperature displayed in Figure 4.7. Hence, the results indicate that the biochemical mechanism of thermal denaturation in BSA is aggregate formation due to the conversion of α-helices into intermolecular β-sheets. These findings are also consistent with the literature: de Wit and Klarenbeek [156] reported that the apparent transition temperature of BSA is 66 °C to 68 °C (depending on the ambient pH), while Lin and Koenig [155] found that BSA aggregation, protein unfolding, and intermolecular β-sheet conformation begin occurring past 60 °C.

The link between the denatured BSA aggregates and the opacity of the bulk medium is provided by the UV/VIS results in Figure 4.3, which again follow a similar trend to the graphs in Figures 4.5 and 4.7. The UV/VIS data demonstrate that as temperature is increased beyond 60 °C, more insoluble BSA aggregates form and decrease the transmittance of light through the solution by acting as optical scattering agents. These insoluble aggregates are generated from the initially soluble ones (as observed in the SEC data), which grow in size as more damage is accumulated and eventually become too large to remain dissolved.

The relationships just described form the complete mechanism that links change in the opacity of the BSA hydrogel with heat-induced denaturation of the proteins. To summarise, at the molecular level, an increasing number of the α-helices in the BSA transform into intermolecular β-sheets as the proteins accumulate thermal damage beyond 60 °C. This causes the BSA molecules to form aggregates, which grow in size and eventually precipitate out of solution. These now-insoluble aggregates scatter incident light and thus decrease the optical transmittance of the medium at a macroscopically observable scale. In the case of BSA hydrogel, the

optical change occurs locally because the matrix of the gel restricts the diffusion of aggregates through the medium. This local change in opacity can be measured using transmitted or backscattered light.

These results show that the opacity of a hydrogel with embedded BSA can serve as a proxy measure of the amount of thermal damage imparted to the proteins. This provides a convenient means of monitoring heat-induced damage in BSA hydrogel quantitatively and in real time during hyperthermia or thermal ablation.

4.4.2 Biological Relevance of the Optical Thermal Damage Metric

Having established that the opacity of BSA hydrogel provides an objective measure of the thermal damage sustained by the embedded proteins, it remains to show that this metric yields results that are comparable to the behaviour of a more biologically relevant system. To this end, the hydrogel opacity measurements in Figure 4.8b can be compared to the ZR75.1 human breast cancer cell survival rates illustrated in Figure 4.8a, since both sets of measurements were tested over the same temperature profiles. Both of these graphs follow a similar pattern: there is little change in both the viability of the breast cancer cells and optical transmittance of the hydrogel up to 60 °C, but these two quantities decrease markedly at 70 °C and beyond. This trend is also seen in Figures 4.3, 4.5, and 4.7, which respectively show UV/VIS optical transmittance, monomer loss, and intermolecular β-sheet formation for aqueous BSA.

The exact relationship between cell survival data and the optical transmittance of the BSA hydrogel would likely change considerably if another cell line were used,

given that the maximum amount of heat damage that a cell can tolerate is generally dependent on the cell type. However, for the purposes of this work, the similar trends observed between the datasets for breast cancer cell viability and BSA protein denaturation shows that the proposed opacity-based metric of heat-induced protein damage yields results that are biologically relevant. Hence, the optical metric can be used to develop and test hyperthermia or thermal ablation protocols in controlled laboratory settings, where the goal is to measure the amount of thermal damage that the protocol would have imparted to cells without having to resort to less convenient monitoring techniques such as histology or cellular assays. In such scenarios, the optical metric also has the significant added advantage that it can be monitored in real time, which is not the case for the other techniques.

4.4.3 Validation and Predictions of the Optical Thermal Damage Metric

Previous work performed by Lafon et al. [79] at lower temperatures and shown in Figure 4.12 supports the results obtained in this experiment: the opacity-time curves follow a similar pattern to those in Figure 4.9 (page 114), and the dependence of the steady-state opacity value on temperature can also be seen. The fact that different steady-state values are achieved depending on the target temperature (Figure 4.10, page 114) indicates that the reaction kinetics describing heat-induced protein damage can change with temperature. However, this is in contradiction with the CEM model of thermal dose discussed in Section 3.3.3 (page 65), which assumes a single rate of reaction. While this model is intended to apply to cells rather than proteins, the fact that it does not provide an adequate description of the simpler situation of high-temperature protein denaturation—which is itself implicated in the

cell death process—is an indication that the CEM model may not apply to cells at high temperatures either. The next chapter will therefore focus on quantifying the performance of the CEM model in describing cell death at these high temperatures (50 °C and above).

Figure 4.12: *Light transmission through 7% BSA polyacrylamide hydrogel as a function of time and target temperature. Reproduced from Lafon et al. [79].*

4.5 Conclusions

The data shown in this chapter demonstrate a clear correlation between the degree of BSA denaturation in hydrogel and the optical transparency of the medium, in addition to providing an experimentally verified explanation of the physical mechanisms that underlie this relationship by linking macroscopic variations in the opacity of the hydrogel with changes in the secondary structure distribution of the protein ensemble. The results also illustrate that the opacity of BSA polyacrylamide hydrogel and the viability of a cancer cell line follow similar trends across a range of temperatures relevant to hyperthermia and thermal ablation. Finally, the data

demonstrate that the amount of heat-induced protein damage is dependent on the maximum temperature reached, thereby motivating a more detailed performance assessment of the CEM model of thermal dose in the next chapter.

In summary, the work presented in this chapter shows that the opacity of hydrogels with embedded BSA provides a metric of accumulated thermal damage that is real-time, accurate, and biologically relevant. These hydrogels may therefore be used for developing, testing and optimising hyperthermia or thermal ablation treatment protocols in controlled laboratory environments.

Chapter 5

Determination of Cytotoxic Thermal Dose During HIFU Ablation

As discussed in Chapter 3, many of the models used to measure HIFU-induced cell death have not been validated or suitably adapted for ablation-relevant temperatures and rates of heating. Moreover, in Chapter 4 it was shown that the reaction kinetics describing heat-induced damage in proteins can be temperature-dependent, which potentially undermines the validity of these models. In this chapter, the performance of the $CEM_{43\,^\circ\mathrm{C}}$ thermal dose metric under HIFU-relevant heating is quantified. A total of 36 agar gels were embedded with different human cancer cell lines (PC3, 22RV1, or ZR75.1) as well as calcein AM and propidium iodide assays. Using a water bath, 12 of the gels were treated with mild hyperthermia, while another 12 were subjected to HIFU-relevant temperature profiles. In each of the remaining 12 gels, 8 HIFU exposures were carried out, and cavitation emissions were monitored passively with a detector transducer that was confocally and coaxially aligned with the HIFU source. Cell death was quantified by measuring the locally averaged fluorescence intensity of the assays relative to unheated and severely heat-shocked gels. The results show that the $CEM_{43\,^\circ\mathrm{C}}$ dose required to achieve the same level of heat-induced cell death varies considerably across cell lines, and that inertial cavitation can cause significant mechanical damage at ablation-relevant intensities even when little thermal dose is delivered ($CEM_{43\,^\circ\mathrm{C}} < 5\,\mathrm{s}$). These findings demonstrate the need for improved models of cell death at ablation-relevant temperatures.

5.1 Motivation and Objectives

As mentioned in Section 3.3.3 (page 65), the $\mathrm{CEM}_{43\,^\circ\mathrm{C}}$ metric of thermal dose is currently the most widely used method of quantifying HIFU-induced cell death. However, the model underlying the $\mathrm{CEM}_{43\,^\circ\mathrm{C}}$ metric has not been validated at temperatures above 54 °C, even though temperatures of up to 100 °C can be achieved during HIFU ablation. Notably, the model assumes that a single Arrhenius reaction dominates damage kinetics at any given temperature—an assumption called into question by the results previously shown in Section 4.3.3 (page 112)—and also does not account for damage caused by non-thermal mechanisms such as acoustic cavitation.

This chapter aims to begin addressing some limitations of the $\mathrm{CEM}_{43\,^\circ\mathrm{C}}$ metric by quantifying its performance under HIFU-relevant heating. Specifically, the objectives of this chapter are to:

- Design a setup in which HIFU-induced thermal and mechanical damage to cells can be measured objectively;
- Assess the validity of the $\mathrm{CEM}_{43\,^\circ\mathrm{C}}$ model above 54 °C (with the piecewise-constant approximation for R given in Equation 3.7, page 69); and
- Determine the relative contribution of mechanically induced damage at different HIFU pressure amplitudes.

5.2 Experimental Methods

5.2.1 Preparation of Cell-Embedding Agar Gels

ZR75.1 cells (human breast cancer) were grown in RPMI 1640 medium without phenol red (PAA Laboratories, E15-848), while 22RV1 and PC3 cells (human prostate cancer) were cultured in DMEM (PAA Laboratories, E15-877). Both growth media also contained 10% (v/v) of fetal bovine serum (PAA Laboratories, A15-151) and 25 U/mL of penicillin-streptomycin (Sigma-Aldrich, P4333).

Cell-embedding gels ("phantoms") were created by suspending 10 million cells from one of the three cell lines into 37 °C molten 0.5% (w/v) agar that had been dissolved in 5 mL of medium and 5 mL of 1X Dulbecco's PBS (PAA Laboratories, H15-002); hence, the final cell concentration in the phantoms was 10^6 cells/mL. Calcein AM (Sigma-Aldrich, 17783) and propidium iodide (Sigma-Aldrich, P4864) were added to the mixture at concentrations of 2 µM and 3 µM, respectively. The phantoms were then cast by injecting 10 mL of the mixture into sterile 7 cm × 7 cm × 2 mm moulds with acoustically transparent windows on both sides (Thermo Fisher Scientific, TKV-320-020S Opticell), as illustrated in Figure 5.1. The gels were set by placing them in a 4 °C fridge for 5 minutes; after this, they were warmed back to 37 °C in an incubator. A total of 36 phantoms (12 for each cell line) were prepared.

5.2.2 Delivery of Thermal and Mechanical Damage

A water bath was used to deliver a thermal dose of 60 minutes at 43 °C to 12 of the phantoms (4 per cell line) under conditions of mild hyperthermia (43 °C for

Figure 5.1: *Photograph of one of the holders used for casting the cell-embedding gels. The optically transparent windows that enclose the gel are made of thin plastic and are also acoustically transparent. The red colour of the liquid in this image is for illustration only (the gels described in the text are optically transparent). Reproduced from company literature by Thermo Fisher Scientific [157].*

60 minutes, 44 °C for 30 minutes, 45 °C for 15 minutes, and 46 °C for 7.5 minutes). Another 12 phantoms were subjected to HIFU-relevant temperature profiles by setting the water bath to 90 °C. During immersion in the water, the temperature in each phantom was monitored in real time using a Type T needle thermocouple (Omega Engineering, HYP0) connected to a temperature data logger (Pico Technology, Pico TC-08). Each phantom was withdrawn from the bath once it had reached one of several peak temperatures (approximately 60 °C, 70 °C, 75 °C, and 80 °C); typically this occurred about 15 s to 20 s after immersion. Immediately after withdrawal, the phantoms were immersed in a 37 °C water bath until they had cooled. Peak heating rates were found to be 2–3 °C/s and the total heating time was typically 15 s to 20 s. In all cases, the total $\mathrm{CEM}_{43\,^\circ\mathrm{C}}$ thermal dose was calculated from the measured temperature profile using Equations 3.5 and 3.7 (page 68).

The remaining 12 phantoms were each mounted in turn on the HIFU setup described in the next section. Prior to each HIFU exposure, the target was positioned such that the centre of the HIFU focal zone was located in the middle of the phantom. The exposure durations ranged from 2 s to 9 s in increments of 1 s, while the peak negative pressure amplitudes ranged from 3 MPa to 6 MPa in increments of 1 MPa.

5.2.3 Apparatus for HIFU Generation and Monitoring

Figure 5.2 illustrates the setup that was used to expose the cell-embedding gels to HIFU while monitoring acoustic emissions at the focus during the exposures (the same apparatus is also used in Chapter 6). In this setup, the tank in which the transducers and target are immersed is 110 cm long, 60 cm wide, and 70 cm high; it contains 300 L of degassed, deionised water kept at 37 °C using an immersion heater (Grant Instruments, GD100, Shepreth, Cambridgeshire, UK). Three pathways in the block diagram of Figure 5.2 can be identified: one for generating the HIFU (top), another for aligning the target (middle), and a third for passive acoustic monitoring (bottom). The components of each of these pathways are detailed throughout the remainder of this section.

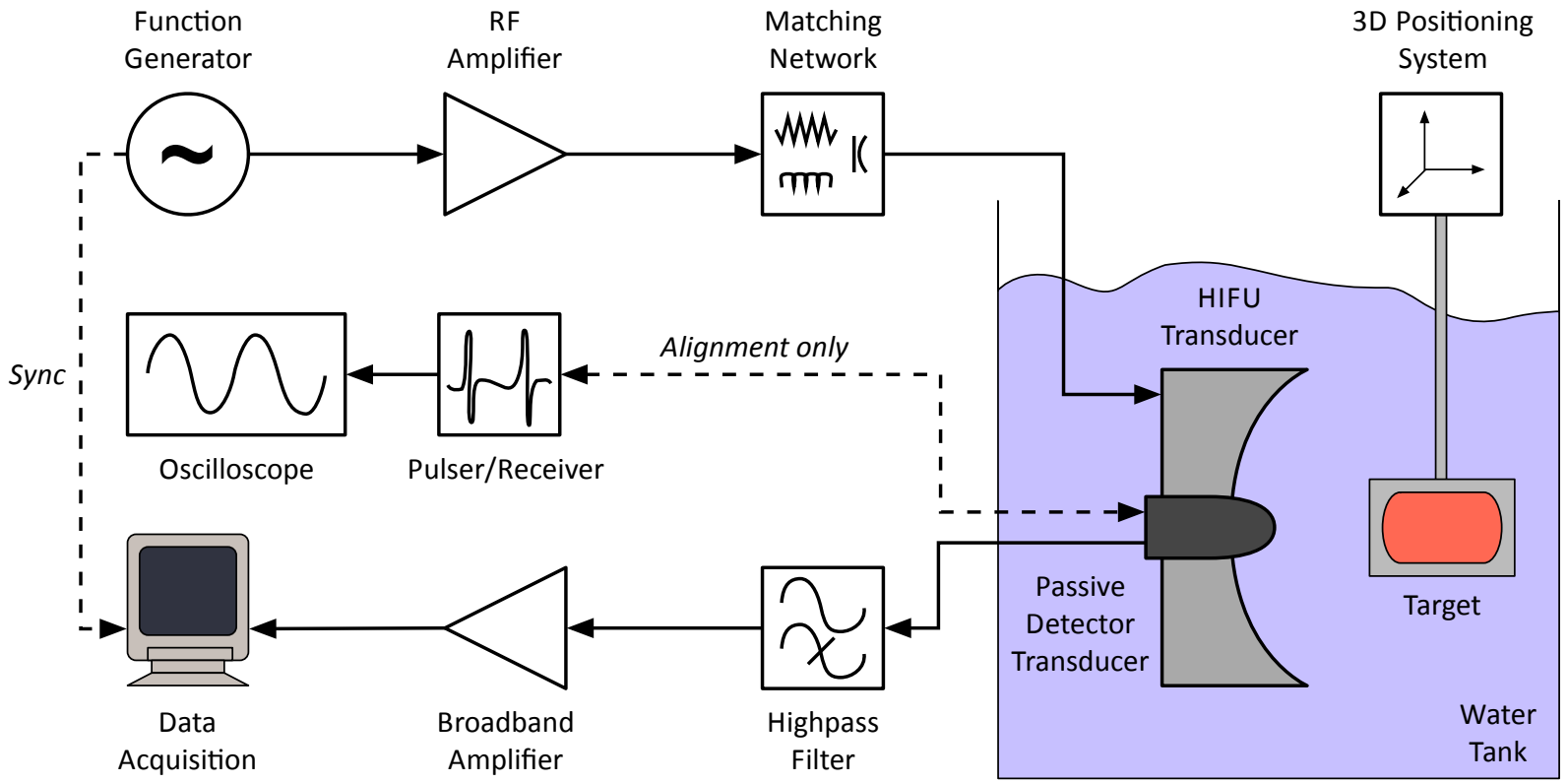

Figure 5.2: *Block diagram of the HIFU ablation monitoring setup used in this work. The driving signal for the HIFU transducer is generated by a computer-controlled function generator and a high-power RF amplifier, followed by a transducer-specific matching network to optimise power transfer. Meanwhile, acoustic emissions at the focus are monitored using a passive detector aligned confocally and coaxially with the HIFU transducer. Before being digitised and recorded by the data acquisition unit in the computer, the signal from the passive detector transducer is conditioned using a highpass filter followed by a broadband amplifier. Also shown are an ultrasonic pulser/receiver and an oscilloscope, which are used to align the tissue with the transducers but are disconnected during exposures.*

HIFU Generation

HIFU exposures are performed using a spherically focussed HIFU transducer (Sonic Concepts, H-102D, Bothell, WA, USA) with an insonation frequency of 1.067 MHz, which is close to the range of frequencies used clinically [6, 8]. The focal length of the transducer is 62.6 mm and its active diameter is 80 mm. Hence, in a medium whose speed of sound is close to 1523.7 m/s (the value for 37 °C water), Equations 2.20 through 2.23 of Section 2.3 (page 41) can be used to show that the −3 dB HIFU focal zone has a diameter of 1.43 mm, a length of 10.5 mm, a transverse focal area of 1.60 mm^2, and a focal volume of 11.2 mm^3. As shown in Appendix B, the speed of sound in all other media employed in this work is not far from that of water, and hence the aforementioned values will be fairly accurate in these media as well.

The driving signal for the HIFU transducer is generated by a computer-controlled arbitrary waveform generator (Agilent Technologies, 33250A, South Queensferry, West Lothian, UK) and a 55 dB high-power RF amplifier (E&I, A300, Rochester, NY, USA), followed by a transducer-specific matching network (Sonic Concepts) to maximise power transfer. The upper limit on the range of pressure amplitudes that can be investigated is determined by the highest safe electrical power input into the matching network (400 W), as recommended by the transducer manufacturer. This constraint means that the voltage amplitude into the matching network can range from 0 V to 180 V. The voltage-pressure calibration of the HIFU transducer was measured in water over this range of driving voltages using a 75 µm PVDF needle hydrophone (Precision Acoustics, HPM075, Dorchester, Dorset, UK). All pressure

amplitudes quoted in this work refer to the measured values in water; in different media, these can be adjusted according to the attenuation coefficient.

All exposures are carried out using quasi-continuous HIFU with a 95% duty cycle and a pulse length of 50 ms. As mentioned earlier in Section 2.2.3 (page 35), these settings allow for the passive localisation of any cavitating microbubbles [67].

Target Alignment

The HIFU transducer is mounted rigidly to the tank, while the target is mounted on a motorised 3D positioning system (Precision Acoustics, Dorchester, Dorset, UK) capable of moving in increments as small as 1 µm. Prior to each exposure, alignment is carried out using an ultrasonic pulser/receiver (JSR Ultrasonics, DPR300, Pittsford, NY, USA) operating in pulse-echo mode, in addition to an oscilloscope (Lecroy, 44MXi, Slough, Berkshire, UK). To minimise signal interference, these two devices are disconnected during the exposures themselves.

Passive Acoustic Monitoring

To measure acoustic emissions at the focus during each exposure, a broadband, focussed transducer with a centre frequency of 15 MHz and a focal length of 75.0 mm (Olympus, V319-SU, Southend-on-Sea, Essex, UK) is mounted on the HIFU transducer and employed as a passive detector. Before any exposures were performed, the detector and HIFU transducers were aligned confocally and coaxially by using a brass ball with a diameter of 6.4 mm as an acoustic target. It should also be noted that the sensitive focal volume of the detector transducer is frequency-dependent [69], per Equations 2.21 and 2.23 of Section 2.3 (page 41). Using the latter formula

to calculate the −3 dB focal volume of the passive detector at various multiples of the HIFU frequency and for a speed of sound of 1523.7 m/s yields the values listed in Table 5.1.

Frequency (MHz)	2.134	3.201	4.268	5.335
Harmonic	2^{nd}	3^{rd}	4^{th}	5^{th}
Focal Volume (mm^3)	1160	400	181	97.6

Table 5.1: *Calculation of the −3 dB focal volume of the detector transducer at various harmonics of the HIFU frequency (1.067 MHz), assuming a speed of sound of 1523.7 m/s as in 37°C water.*

The signal from the detector transducer is conditioned with a 2 MHz highpass filter (Allen Avionics, Mineola, NY, USA) to remove seep-through at the fundamental frequency of the HIFU transducer, followed by a broadband amplifier with a gain of 25 (Stanford Research Systems, SR445A, Sunnyvale, CA, USA). The conditioned signal is recorded using a 14-bit digitiser and data acquisition unit (National Instruments, NI PCI-5122, Austin, TX, USA). All computer-controlled components are operated using LabVIEW 8.6 (National Instruments).

Data acquisition is performed by acquiring traces of 40 000 samples of data at a sampling frequency of 100 MHz. Each new trace is acquired as soon as the previous trace is written out of the buffer; typical delays between consecutive traces were found to be of the order of 5 ms to 10 ms. To measure background noise (which did not change significantly across different runs of the experiments), acquisition is started 2 s before each HIFU exposure, and continues for 2 s more after the HIFU transducer is turned off. A comb filter is used to separate harmonic and broadband components in the frequency domain, with the amplitude of the latter taken as an

indicator of the strength of inertial cavitation, as discussed in Section 2.2.3 (page 35).

Figure 5.3 illustrates the data acquisition protocol with an example set of traces. Shown within this figure are a single HIFU exposure (Figure 5.3a), a single trace from this exposure (Figure 5.3b), the spectral content of this trace (Figure 5.3c), and the spectrogram of the entire HIFU exposure (Figure 5.3d). Spectrograms are generated using a Short Time Fourier Transform [158], and are effective tools for visualising how the frequency content of a signal evolves over time.

5.2.4 Quantification of Cell Death

In all phantoms, cell viability and cell death following thermal damage (induced using a 90 °C water bath) or mechanical damage (induced using HIFU) was quantified by imaging the heat-treated area of the phantoms using a fluorescence microscope (Nikon, Eclipse Ti-E, Kingston upon Thames, Surrey, UK). Each image was taken in a 6 mm × 6 mm plane halfway between the phantom walls at 4X magnification (3.2 µm/pixel). The fluorescence intensities of the calcein AM and propidium iodide were measured by applying FITC and TRITC filters, respectively, as shown in Figure 5.4. The average intensity values for the entire image were normalised by control values from images taken prior to heating (no cell death) as well as after severe heat shock (95 °C for 2 minutes; complete cell death). In this way, percentage measurements of cell viability and cell death before and after heating were obtained.

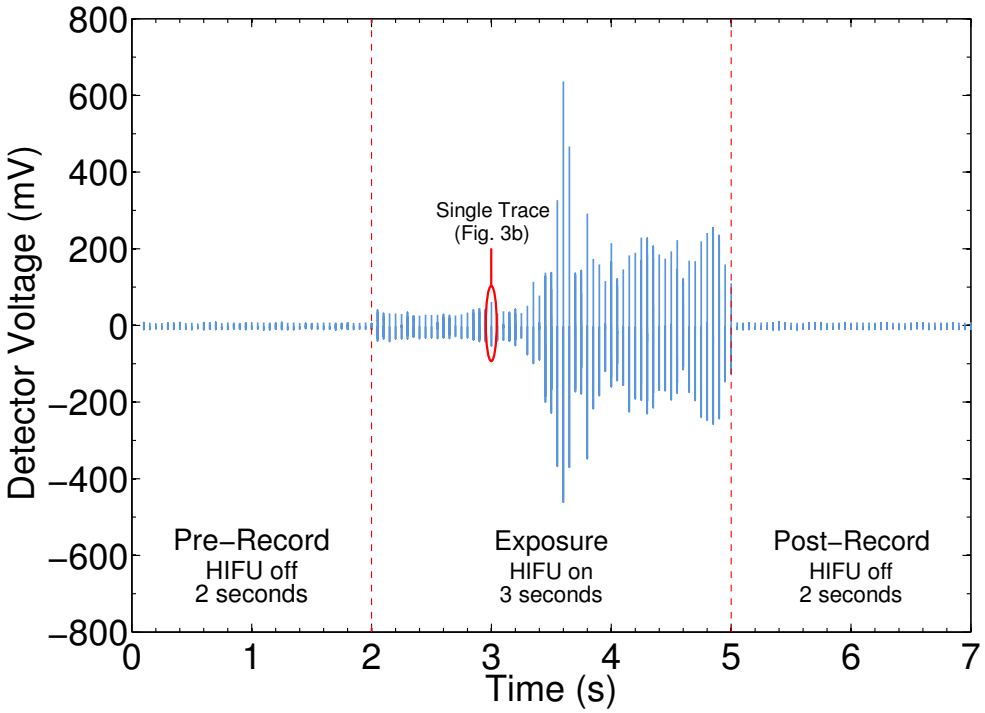

(a) *Example of a dataset acquired during a single HIFU exposure, with the 2-second pre- and post-exposure recording periods identified.*

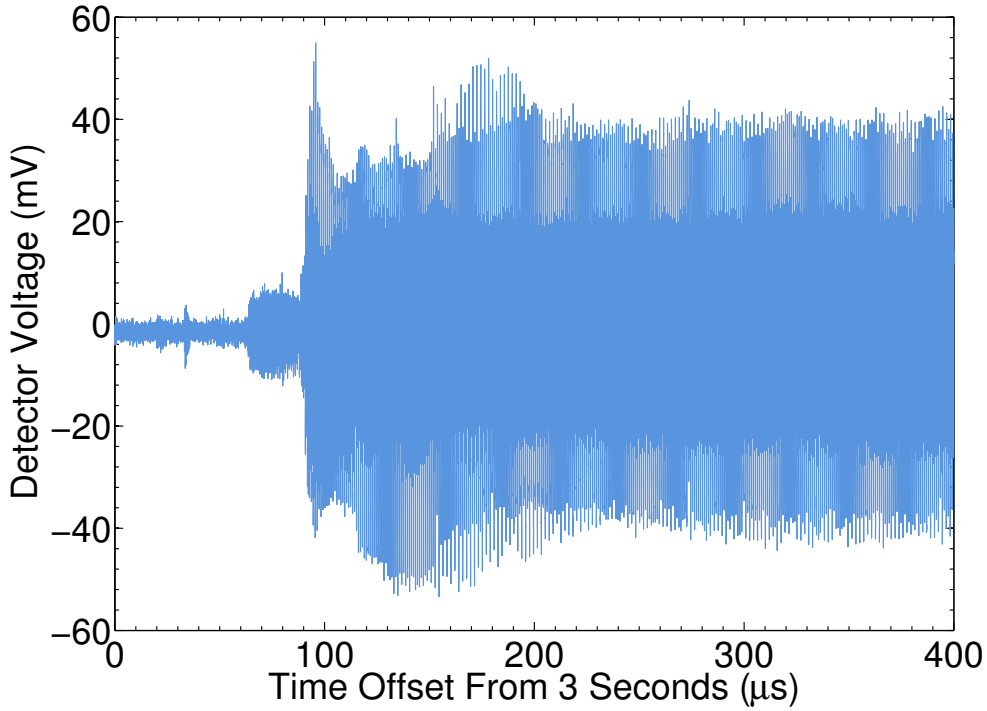

(b) *A trace captured during the HIFU exposure shown in Figure 5.3a. Each trace contains 40 000 samples spaced 10 ns apart.*

Figure 5.3: *Illustration of the data acquisition protocol for a 5 s HIFU exposure.* *(Continued on the next page.)*

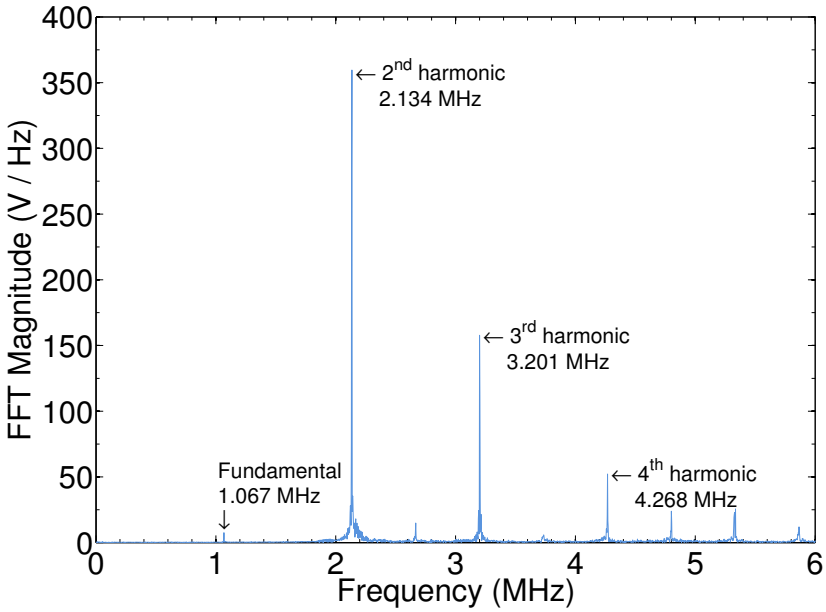

(c) *The spectral content of the trace shown in Figure 5.3b, obtained by taking the magnitude of the Fast Fourier Transform (FFT) of all 40 000 samples. The highest frequency shown in this plot is well below the Nyquist sampling frequency of 50 MHz. Much of the signal energy is concentrated around multiples of the insonation frequency (1.067 MHz).*

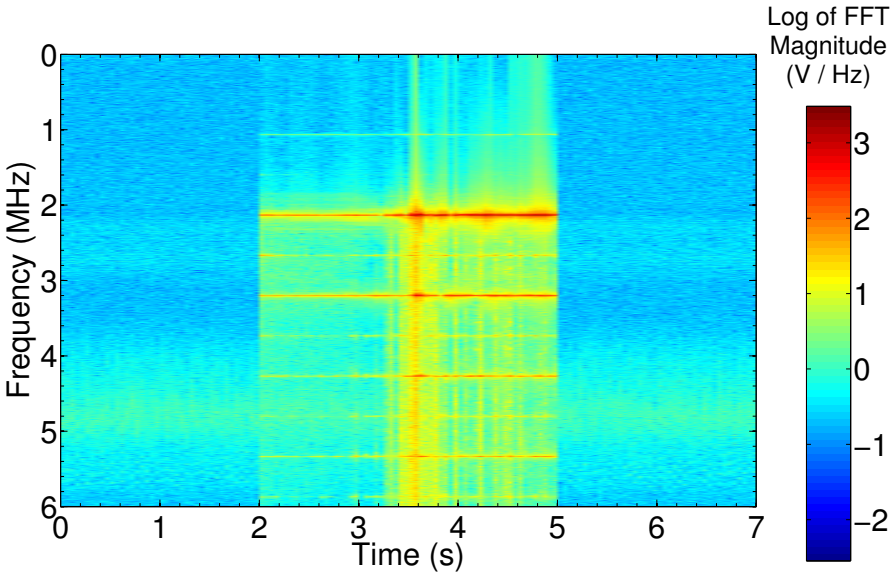

(d) *A spectrogram of the exposure, obtained by plotting the FFT magnitude over time. The FFT magnitude at a given time and frequency is indicated by the colour of the plot. As in Figure 5.3a, the pre- and post-exposure periods are marked by decreased signal energy across all frequencies compared to the exposure period from 2 s to 5 s. During the exposure, much of the signal energy is concentrated in the harmonics, as is the case in Figure 5.3c. An increase in the broadband noise level can also be seen at approximately 3.4 s.*

Figure 5.3: *Illustration of the data acquisition protocol for a 5 s HIFU exposure.*

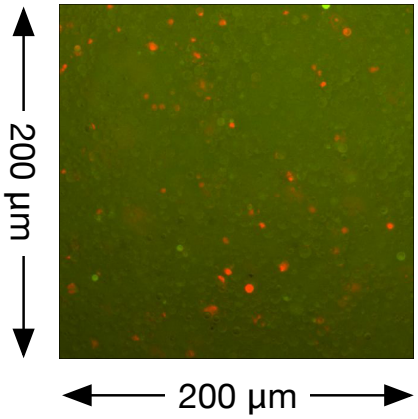

(a) *A 200 µm × 200 µm section from the combined 2-D fluorescence intensity maps of calcein AM (green, viable cells) and propidium iodide (red, dead cells) in one section of a cell phantom, imaged using the method described in the text.*

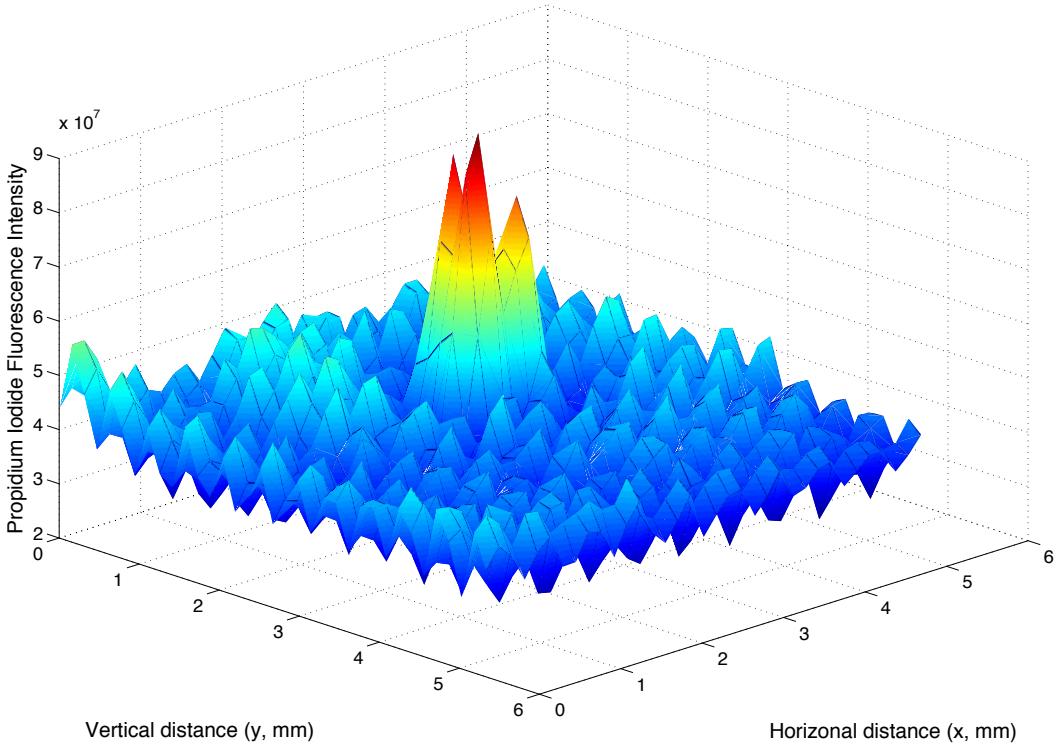

(b) *A fluorescence intensity map for propidium iodide in the region surrounding the HIFU focus after a 5 s exposure at 6 MPa peak rarefaction pressure. Damage caused by the first sidelobe of the HIFU beam is also visible in the image.*

Figure 5.4: *2-D fluorescence intensity maps of calcein AM and propidium iodide in cell phantoms.*

5.3 Results and Discussion

In all phantoms treated with a $\mathrm{CEM}_{43\,^\circ\mathrm{C}}$ of 60 minutes under mild hyperthermia, the amount of cell death was found to lie between 20% and 23%, confirming the validity of the $\mathrm{CEM}_{43\,^\circ\mathrm{C}}$ metric in this temperature range. However, the results shown in Figure 5.5 for HIFU-relevant temperature profiles demonstrate that different values of cell death are obtained for the same $\mathrm{CEM}_{43\,^\circ\mathrm{C}}$ above 60 °C. These results also suggest that the commonly employed thermal dose threshold of 240 minutes at 43 °C may not be sufficient to kill all cells if the heating time is short (15 s to 20 s for the data in Figure 5.5). This is likely due to important differences in the reaction kinetics that govern cell death under mild hyperthermia and under high-temperature ablation. The discrepancy between the model-based predictions and the experimental results could be addressed by using a parametric model of cell death instead, such as the two-state model proposed by Feng et al. [112] or $\mathrm{CEM}_{43\,^\circ\mathrm{C}}$ using the correct definition of the placeholder function R (given in Equation 3.6, page 69) instead of the commonly used piecewise-constant approximation (Equation 3.7). However, to do this, more information would be required on the appropriate activation energies and breakpoints above 54 °C.

For phantoms exposed to HIFU, it was found that significant levels of cell death (10% or more) began occurring at pressure amplitudes of 5 MPa held for 3 s or more. Elevated broadband noise levels were also observed in the acoustic emissions associated with these exposures. However, the temperature at the focus never exceeded 41 °C because of the large volume of 37 °C water surrounding the phantoms; hence

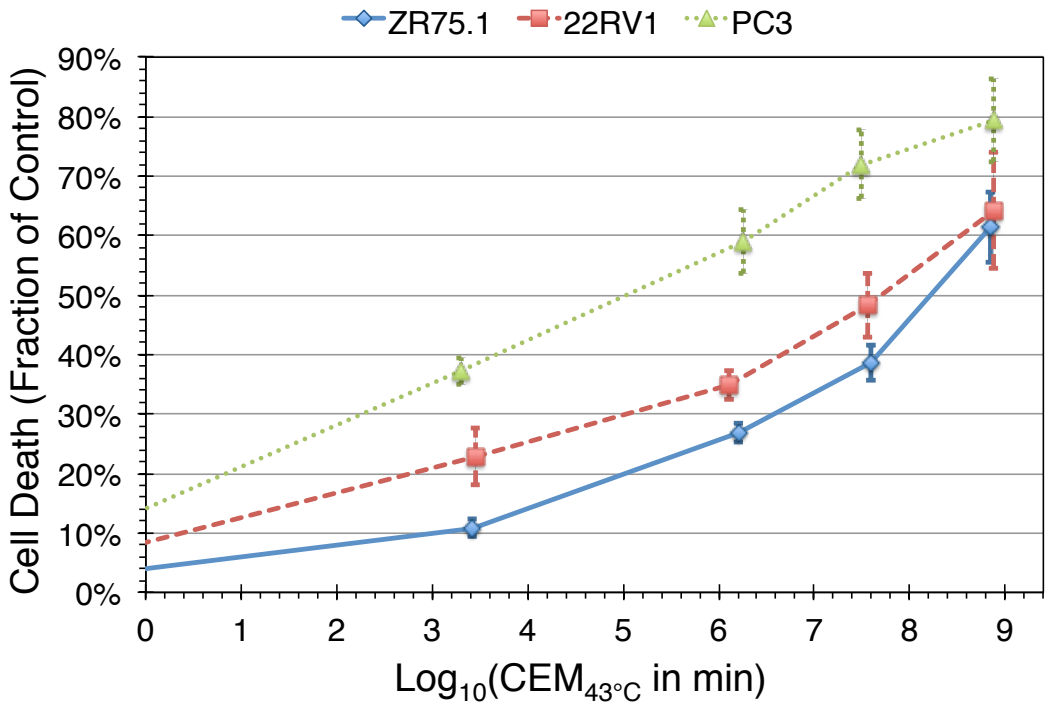

Figure 5.5: *Plot of thermally induced cell death versus $CEM_{43\,^\circ C}$ thermal dose for different cancer cell lines. Each sample is the average of 3 measurements from different sections of the same phantom; the error bars give standard deviation.*

the $CEM_{43\,^\circ C}$ thermal dose was never more than 5 s. It is therefore likely that inertial cavitation, rather than thermal effects, is responsible for causing cell death in these regimes. This demonstrates the potential limitations of $CEM_{43\,^\circ C}$—as well as other metrics of cell death based solely on temperature—in the context of HIFU ablation, particularly when inertial cavitation occurs.

5.4 Conclusions

In this chapter, an experimental setup was designed for measuring the thermal and mechanical damage delivered to cells following exposure to HIFU or HIFU-relevant temperature profiles. The data shown in this chapter demonstrate that the commonly used $CEM_{43\,^\circ C}$ model of thermal dose can yield misleading results when

the temperature exceeds 54 °C or when the peak rarefactional pressure and exposure time are high enough to permit significant damage from inertial cavitation to occur (5 MPa held for 3 s or more in the model used here).

The aforementioned limitations could potentially be addressed in future work by employing a more advanced parametric model of thermal dose, such as the $\mathrm{CEM}_{43\,^{\circ}\mathrm{C}}$ with the original definition of the R function or the two-state model proposed by Feng et al. [112] (see Section 3.3.3, page 65). Nevertheless, the different values for cell death obtained for different cell lines strongly suggest that a single thermal model is unlikely to provide adequate predictions of heat-induced cell death, unless the operator has prior knowledge of the cancer cell type and the surrounding tissue during HIFU therapy. However, this prior knowledge is difficult to obtain in the case of metastatic cancer. Hence, the next chapter focusses on the development of a novel, passive acoustic technique designed for monitoring HIFU-induced tissue damage in real time and without the need for thermometry.

Chapter

6

Real-Time Passive Acoustic Monitoring of HIFU-Induced Tissue Damage

The results of Chapter 5 show that models of damage based solely on temperature are unable to provide a complete description of HIFU-induced damage in tissue. This chapter therefore proposes a novel method of real-time HIFU treatment monitoring that employs the passively monitored acoustic emissions at the focus during exposure. 212 HIFU exposures were performed in 7 freshly excised ox livers across a range of insonation durations and acoustic intensities. Lesion presence and size were ascertained by slicing the tissue in the transverse and axial focal planes post-exposure. The results demonstrate that the successful formation of HIFU lesions in ex vivo ox liver is highly correlated with the presence of pronounced dips in the magnitude of the passively monitored acoustic emissions at integer harmonics of the insonation frequency. A detector based on this observation predicted lesioning with over 80% accuracy in regimes that were very likely to create lesions (60 J of energy or more), and had an error rate of less than 6% for exposures that were too short to cause lesioning (up to 1 s long). The overall sensitivity and specificity of the detector were 75.6% and 74.2%, respectively. The detector proposed in this chapter could therefore provide a low-cost means of effectively monitoring clinical HIFU treatments passively and in real time.

6.1 Motivation and Objectives

The results of the previous chapter show that models of damage based solely on temperature are unable to provide a complete description of HIFU-induced damage in tissue, particularly if the cell types present in the tumour are not known in advance. Moreover, as discussed earlier in Section 3.4.3 (page 79), thermometry is difficult to obtain *in vivo*, which limits the potential usefulness of any temperature-based monitoring technique.

The objective of this chapter is therefore to design, optimise, and validate a novel HIFU lesion formation detector that does not depend on thermometry and incorporates the following features:

- Employs passively monitored data only;
- Provides real time detection during HIFU exposure;
- Entails minimal additional equipment and cost; and
- Requires no modification of the HIFU signal.

To accomplish this objective, the detector will make use of the acoustic emissions at the focus during HIFU exposure, which can be monitored passively and can be analysed in real time for potential indicators of lesion formation.

6.2 Experimental Methods

6.2.1 Tissue Preparation and Exposure to HIFU

Ox livers were sourced from a commercial abattoir (Mutchmeats Limited, Witney, Oxfordshire, UK) and were used within 4 hours of slaughter. For each liver, a block of tissue measuring 9 cm × 9 cm in cross section and 4 cm in depth was cut out of the organ, avoiding large veins and blood vessels where possible. To maintain as much clinical relevance as possible, the tissue was cut such that the front face of the block retained the capsule surrounding the organ. During exposures, this face was positioned nearest to the HIFU transducer, as would be the case during an *in vivo* HIFU treatment.

The excised block of liver was immersed in 4 L of non-degassed 1X Dulbecco's PBS (Invitrogen, 21600-010, Paisley, Renfrewshire, UK). To prevent pre-focal cavitation near the tissue surface, the block of liver and PBS were degassed in a 6 L chamber at 0.2 bar for 30 minutes, after which the tissue was sealed in a holder of the same internal dimensions (9 cm × 9 cm × 4 cm). When transferring the tissue to the holder, care was taken to ensure that the liver was surrounded by degassed PBS at all times so as to minimise the ingress of air bubbles. The holder was constructed such that ultrasound could pass freely between the front and back faces of the tissue block via thin, acoustically transparent windows made of biaxially oriented polyethylene terephthalate film (commonly referred to as boPET or Mylar). The sealed holder containing the tissue and PBS is shown in Figure 6.1a.

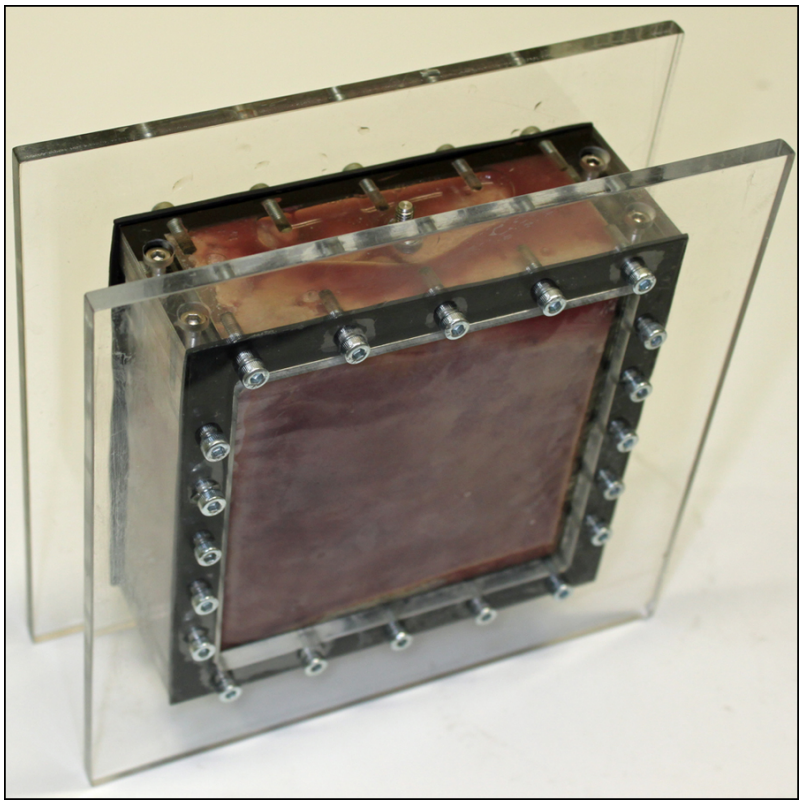

(a) *The tissue holder used to encapsulate the degassed tissue and PBS during HIFU exposures in the water tank.*

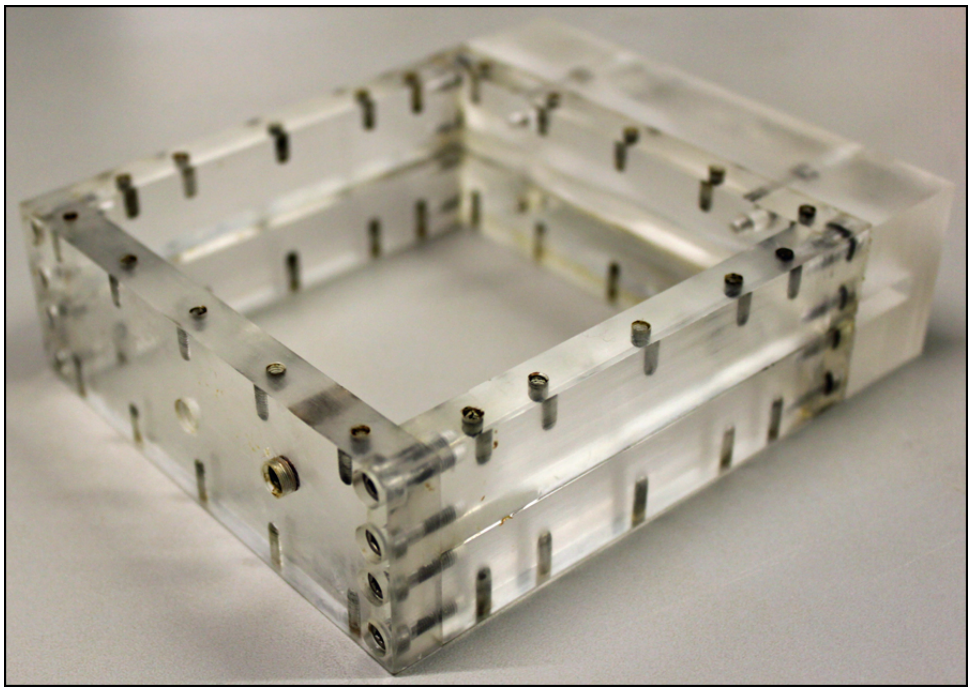

(b) *A tissue holder constructed with a transverse slot at 2 cm depth. This slot was used to slice the tissue through the central plane of the HIFU focal region after the exposures were completed.*

Figure 6.1: *Photographs of the holders used in the HIFU tissue ablation experiment.*

HIFU exposures were performed using a setup identical to the one described in the previous chapter (Section 5.2.3, page 125). The exposures in each tissue sample were carried out at a depth of 2 cm in the tissue, in grids with a spacing of 1 cm between adjacent points, as illustrated in Figure 6.2a. As in the rest of this work, the pressure amplitudes quoted in this chapter refer to the measured values in water. Assuming an attenuation coefficient through liver tissue of 5.0 Np/m as indicated in Appendix B, the amplitudes in tissue at the shooting depth of 2 cm will be 90% of those measured in water. The I_{SPTA} intensity (spatial peak, temporal average) was calculated with Equation 2.24 (page 44) by assuming a plane wave at the HIFU focus and by using the acoustic impedance of 37 °C bovine liver indicated in Appendix B.

6.2.2 Post-Exposure Lesion Volume Measurement

After the tissue had been exposed to HIFU, the sample was removed from its holder and sliced transversely at a depth of 2 cm, through the central plane of the HIFU focal region, by making use of a guiding slit in the side of the holder shown in Figure 6.1b. A photograph of the tissue after this cut, on the side farthest from the transducer, is shown in Figure 6.2a. The diameter d of each lesion cross-section was measured using vernier callipers (Fowler, 54-101-150-2, Newton, MA, USA). The tissue was then sliced in the axial plane passing through the centre of each lesion, as illustrated in Figure 6.2b, and the length ℓ of each lesion was also measured using the callipers.

To determine lesion volume, the shape of the lesions was approximated as a prolate spheroid. This approximation was motivated by visual inspection of the

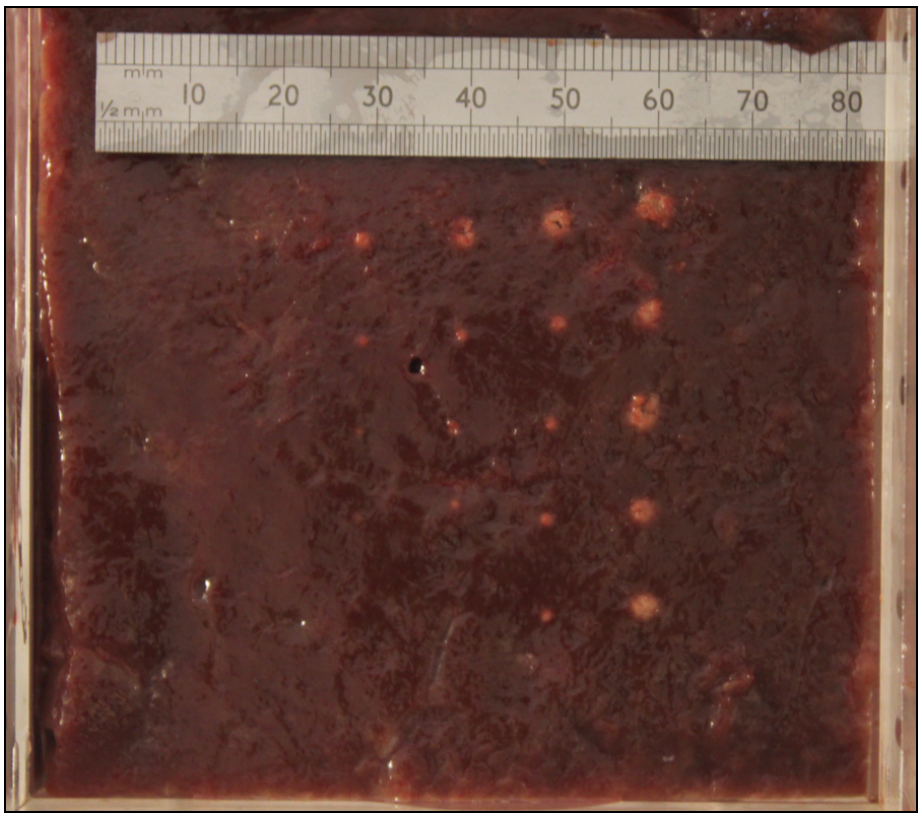

(a) *Transverse view of a grid of lesions created with an acoustic intensity (I_{SPTA}) of 1130 W/cm^2 and various exposure times (e.g. 5 s in the rightmost column). The part of the tissue shown is the one farthest from the transducer.*

(b) *Axial view of the 5 s lesions (the rightmost column in the grid of Figure 6.2a). Only the distal half of each lesion (2 cm to 4 cm deep) is shown in the image.*

Figure 6.2: *An example of a lesion grid generated during the HIFU tissue ablation experiment. A ruler is included in both images to show scale. The spacing between adjacent lesions is 1 cm.*

lesions and has also been used in other studies [125]. Under this approximation, the diameter d of the lesion cross-section corresponds to the equatorial diameter and the length ℓ of the lesion corresponds to the polar diameter, giving a lesion volume V of

$$V = \frac{\pi d^2 \ell}{6}. \tag{6.1}$$

This originates from the same formula as the one used previously to calculate the $-3\,\mathrm{dB}$ focal volumes of spherically focussed acoustic transducers (Equation 2.23, page 43), since the focal regions of those transducers are also shaped like prolate spheroids.

6.2.3 Lesion Detection Algorithm

All data were analysed in MATLAB release 2009a (The MathWorks, Natick, MA, USA). Initial examination of the spectrograms associated with each exposure suggested that, in exposures that generated lesions, the magnitude of the passively monitored acoustic signal would temporarily decrease by an order of magnitude or more at integer multiples of the insonation frequency, as illustrated in Figure 6.3. Based on this observation, an algorithm was devised to detect the presence or absence of this feature in the signal and was implemented in MATLAB.

The lesion detection algorithm is illustrated in Figure 6.4. To begin with, a spectrogram of the signal is computed using a Short Time Fourier Transform [158], as illustrated in Figure 5.3d (page 132). The harmonics of interest are then extracted directly from the spectrogram. In Figure 5.3d, this would correspond to isolating

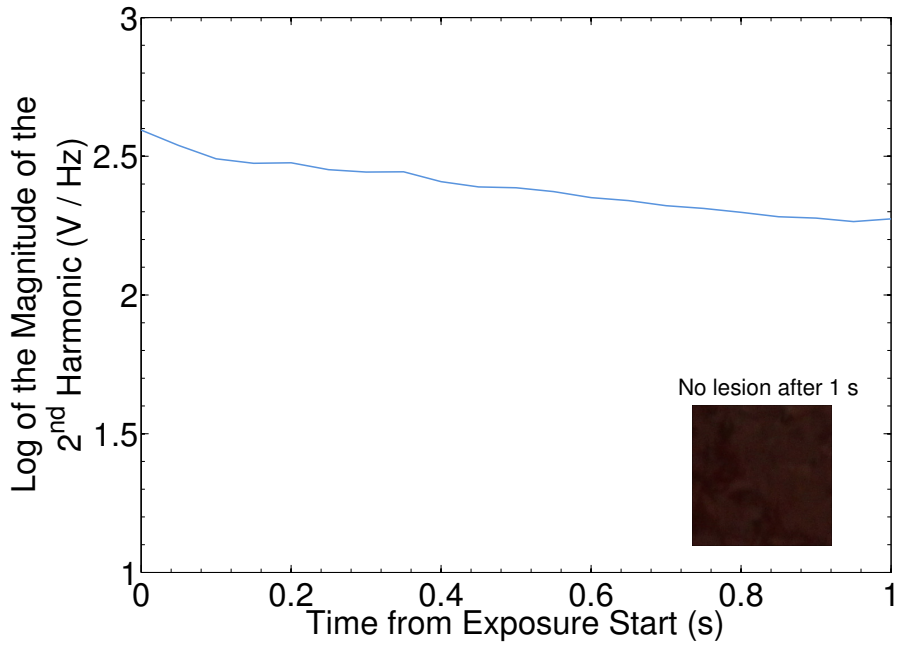

(a) *An exposure lasting 1 s, resulting in no lesion. No dips in the signal magnitude at any of harmonics 2 through 5 were observed (2^{nd} harmonic only displayed).*

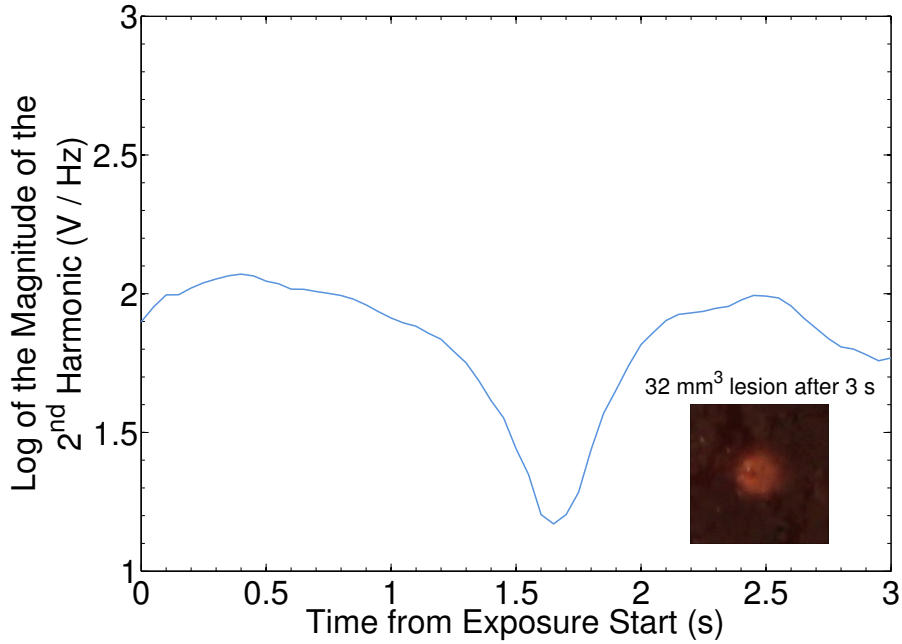

(b) *A 3 s exposure that created a lesion of 32 mm^3, shown in the inset. Here a dip can be observed in the magnitude of the 2^{nd} harmonic.*

Figure 6.3: *Examples of the correlation between the formation of lesions and the appearance of dips in the magnitude of the passively monitored signal at harmonics of the insonation frequency. The magnitudes are plotted on a logarithmic scale. Both exposures were carried out at the same acoustic intensity (I_{SPTA}) of 1130 W/cm^2.*

single horizontal lines in the plot at the frequencies closest to those associated with each harmonic.

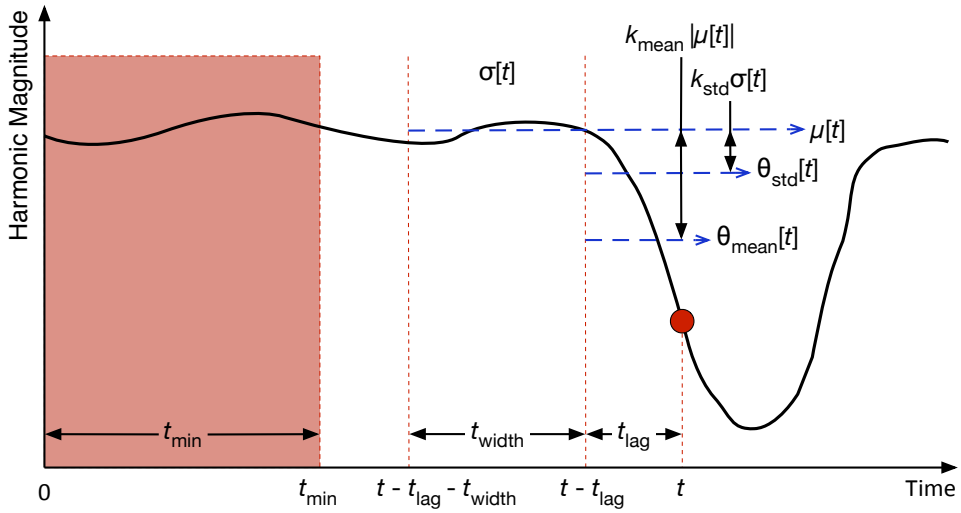

Figure 6.4: *Illustration of the operation of the lesion detection algorithm, which is designed to detect dips in the magnitude of the received signal at integer multiples of the insonation frequency. The various detector parameters are also indicated on the diagram. The filled circle represents the current time (denoted t).*

For simplicity, in this study the emissions data from each exposure were only analysed after the exposure was completed. Ideal (non-causal) bandpass filters with a passband width of 30 kHz were used to obtain the spectrogram as well as to extract the harmonics. Since the fundamental frequency was filtered out prior to signal acquisition as noted previously, the lowest harmonic examined was the 2^{nd} one. Also, the highest harmonic that could be reliably distinguished from noise in all exposures was found to be the 5^{th} one; hence, higher harmonics than this were not considered.

After extracting all harmonics of interest, the natural logarithm of each harmonic is taken. The mean μ and standard deviation σ are then calculated for each of these logarithmically scaled signals over a window having a width of $t_{\text{width}} = 450$ ms and

a lag of $t_{\text{lag}} = 200\,\text{ms}$ with respect to the current time, as illustrated in Figure 6.4. Thus, at a given time t, the mean and standard deviation in the window may be computed using the equations

$$\mu[t] = \frac{\sum_{\tau \in [t - t_{\text{lag}} - t_{\text{width}}, t - t_{\text{lag}}]} h[\tau]}{f_{\text{s}} \cdot t_{\text{width}}} \tag{6.2}$$

and

$$\sigma[t] = \sqrt{\frac{\sum_{\tau \in [t - t_{\text{lag}} - t_{\text{width}}, t - t_{\text{lag}}]} h^2[\tau]}{f_{\text{s}} \cdot t_{\text{width}}} - \mu^2[t]} \tag{6.3}$$

where h is the natural logarithm of the magnitude over time of the harmonic being analysed and f_{s} is the sampling frequency (hence, $f_{\text{s}} \cdot t_{\text{width}}$ is the number of points in the window). It should be noted that Equations 6.2 and 6.3 can only be applied once a time of at least $t_{\text{min}} = t_{\text{width}} + t_{\text{lag}} = 650\,\text{ms}$ has elapsed, since this is the minimum time required to establish the window. However, it will be shown later that no lesioning occurs during this initial time period.

To identify dips such as those shown in Figures 6.3b and 6.4, two thresholds are established based on the values of the mean μ and the standard deviation σ associated with each harmonic. The first threshold, θ_{mean}, is set 25% below the mean, while the second threshold, θ_{std}, is set to 4 standard deviations below the mean. These thresholds are illustrated in Figure 6.4 and may be computed using the equations

$$\theta_{\text{mean}}[t] = \mu[t] - k_{\text{mean}}|\mu[t]| \tag{6.4}$$

and

$$\theta_{\text{std}}[t] = \mu[t] - k_{\text{std}}\sigma[t] \tag{6.5}$$

where $k_{\text{mean}} = 25\% = 0.25$ and $k_{\text{std}} = 4.0$. A dip is identified when the harmonic falls below the smaller of these two thresholds and subsequently rises above this same threshold at a later time.

6.2.4 Detector Performance Assessment

The performance of the lesion detection algorithm was assessed by comparing the output of the algorithm to the post-exposure measurement of lesion volume, with the latter taken as the "gold standard" in this case. For this purpose, a lesion was deemed to have formed if its volume was nonzero. The four possible cases that can occur when comparing the output of the detector to the lesion formation assessment are true negative (TN, no lesion and no dip), true positive (TP, both lesioning and a dip occur), false negative (FN, lesioning occurs but no dip is observed), and false positive (FP, a dip is observed but lesioning has not occurred). The first two cases (true negative and true positive) thus correspond to correct detection, while the latter two cases (false negative and false positive) are detector errors.

By classifying the results into the four cases listed, the following measures of detector performance may be derived [8, 159]:

$$\text{Incidence of Lesioning} = \frac{\text{TP} + \text{FN}}{\text{TN} + \text{TP} + \text{FN} + \text{FP}}; \tag{6.6}$$

$$\text{Accuracy} = \frac{\text{TN} + \text{TP}}{\text{TN} + \text{TP} + \text{FN} + \text{FP}}; \tag{6.7}$$

$$\text{Sensitivity} = \frac{\text{TP}}{\text{TP} + \text{FN}}; \text{ and} \tag{6.8}$$

$$\text{Specificity} = \frac{\text{TN}}{\text{TN} + \text{FP}}. \tag{6.9}$$

Here sensitivity may be interpreted as the proportion of positive cases (i.e. those in which lesions formed) that have been correctly identified by the lesion detection algorithm, while specificity represents the proportion of negative cases (those in which a lesion did not form) that have been correctly identified.

6.2.5 Detector Parameter Selection

The lesion detection algorithm described previously contains four parameters: t_{width} (width of the window), t_{lag} (lag of the window), k_{mean} (mean-based threshold, Equation 6.4), and k_{std} (standard deviation threshold, Equation 6.5). In selecting the values of these parameters used in this study, the objective was to maximise the sensitivity of the detector (Equation 6.8) given an acceptable level of specificity (Equation 6.9). In detectors involving a single adjustable parameter, a common tool used to accomplish this task is the Receiver Operating Characteristic (ROC) of the detector, which is a plot of sensitivity against specificity across a range of candidate values for the parameter. In this case, a similar technique was used to select parameter values; however, because the present detector algorithm involves

more than one adjustable parameter, the graph of sensitivity versus specificity is a scatter plot rather than a single curve.

Table 6.1 lists the candidate parameter values that were tested. Figure 6.5 displays the overall sensitivity and specificity of the detector for all 14 553 possible combinations of the candidate values, with each point in the graph corresponding to one combination. The dotted line with 45° slope represents the performance of a random detector whose output has no correlation with the observed phenomenon; it can be seen that nearly all sets of parameter values tested yield a better performance than this baseline.

Parameter	Values Tested	Selection
t_{width} (window width)	50, 100, 150, ..., (700 ms - t_{lag})	450 ms
t_{lag} (window lag)	0, 50, 100, ..., 500 ms	200 ms
k_{mean} (mean-based threshold)	0, 5%, 10%, ..., 100%	25%
k_{std} (standard deviation threshold)	0, 1.0, 2.0, 2.5, 3.0, 3.5, and 4.0	4.0

Table 6.1: *Parameter selection process for the harmonic dip detector. The ranges of t_{width} and t_{lag} are chosen such that $t_{min} = t_{width} + t_{lag}$ does not exceed 700 ms. There are a total of 14 553 possible combinations of candidate parameter values.*

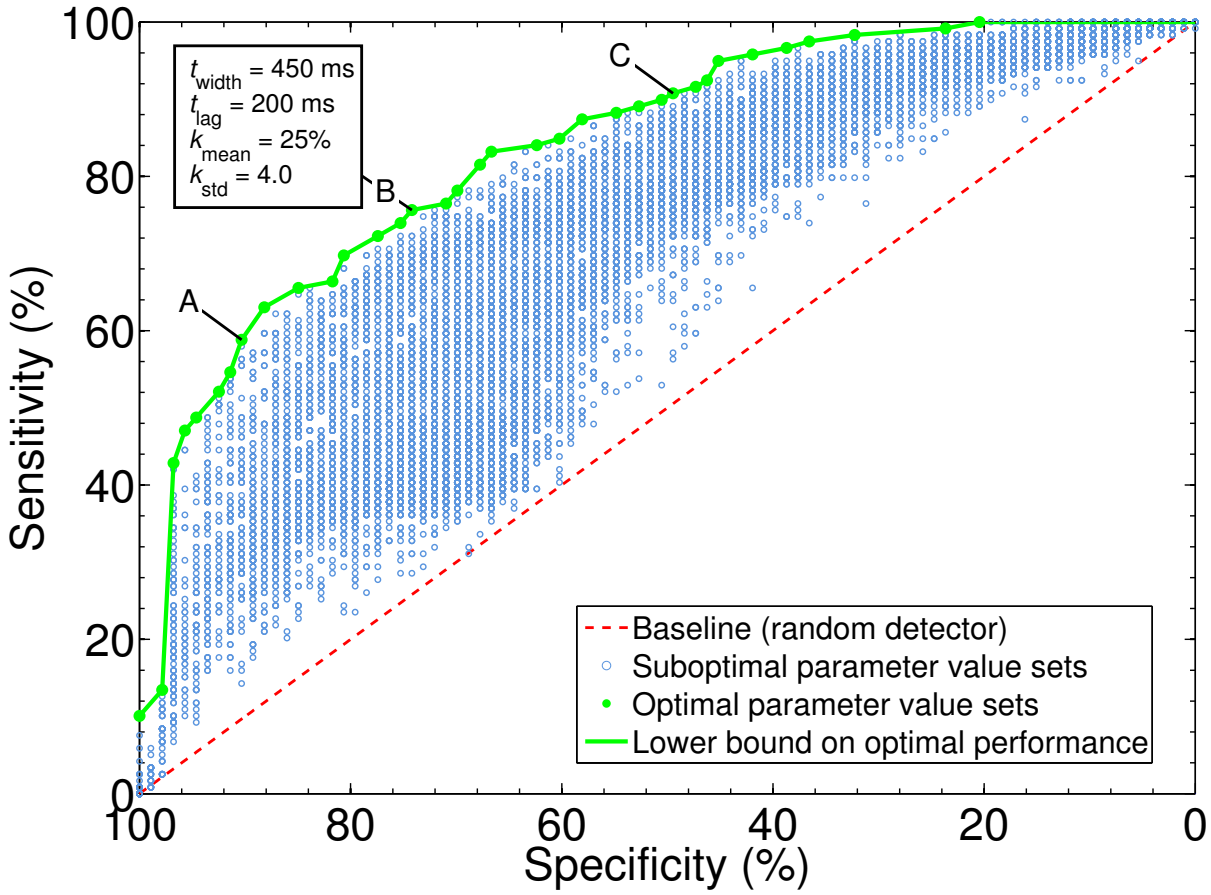

Figure 6.5: *Scatter plot of the sensitivity and specificity of the detector across all 212 exposures for each of the 14 553 parameter value combinations listed in Table 6.1. Note that the horizontal axis is in decreasing order. Detector performance statistics at the optimal points labelled A (the point closest to 90% specificity), B (the selected operating point), and C (the point closest to 90% sensitivity) are given in Table 6.2. The parameter values associated with the selected operating point are also indicated on the figure.*

In many binary classification tests, selecting detector parameters involves determining an acceptable compromise between sensitivity and specificity by varying the detection threshold. This trade-off is seen in Figure 6.5, as the general trend is for sensitivity to decrease as specificity increases. Points plotted as hollow circles in the figure correspond to suboptimal sets of parameter values, in that there exists at least one other set of values that achieves a better sensitivity for an equal or greater specificity. On the other hand, points plotted as filled circles correspond to optimal sets of parameter values, for which no higher sensitivity can be achieved without decreasing the specificity. The solid curve linking the optimal points thus represents a lower bound on the maximum detector sensitivity that can be achieved for a given level of specificity. The point corresponding to the selected values of $t_{\text{width}} = 450$ ms, $t_{\text{lag}} = 200\,\text{ms}$, $k_{\text{mean}} = 25\%$, and $k_{\text{std}} = 4.0$ is indicated on Figure 6.5 and is labelled as point B. This operating point was chosen because it yields a good balance between sensitivity (75.6%) and specificity (74.2%) out of all the optimal sets in the figure.

As shown in Equations 6.8 and 6.9, changing the sensitivity and specificity of the detector will affect its overall performance. Table 6.2 illustrates this by listing the detector performance statistics at point A (the operating point closest to 90% specificity) and at point C (the operating point closest to 90% sensitivity) alongside those at point B (the selected operating point). The practical implications of choosing an operating point with a different sensitivity or a different specificity will be discussed further in Section 6.3.3 (page 158).

	Point A	Point B (Selected)	Point C
Sensitivity	58.8% (Low)	75.6% (Mid-range)	90.8% (High)
Specificity	90.3% (High)	74.2% (Mid-range)	49.5% (Low)
Accuracy	72.6% (154 of 212)	75.0% (159 of 212)	72.6% (154 of 212)
False Negatives	23.1% (49 of 212)	13.7% (29 of 212)	5.2% (11 of 212)
False Positives	4.3% (9 of 212)	11.3% (24 of 212)	22.2% (47 of 212)

Table 6.2: *Detector performance across all 212 exposures for the three optimal analyses labelled in Figure 6.5. Points A and C are the operating points closest to 90% specificity and 90% sensitivity, respectively, while Point B is the selected operating point and corresponds to mid-range values of sensitivity and specificity.*

6.3 Results and Discussion

6.3.1 Lesion Size

Figure 6.6 shows the variation in lesion volume with exposure time (Figure 6.6a) and energy (Figure 6.6b). In both graphs, the lesion volumes are further split according to acoustic intensity. The pressure amplitude corresponding to each intensity level is also indicated, based on the relationship between intensity and pressure given in Equation 2.24 (page 44). The error bars in each figure result mainly from the difficulty in obtaining precise measurements of lesion volumes using manual slicing. The variability between tissues from different animals as well as inhomogeneities within the same block of tissue also act as sources of error. Nevertheless, in spite of these factors, lesion volume as measured by manual slicing increases with exposure time, acoustic intensity, and exposure energy, as would be expected. Moreover, Figure 6.6a shows that across the range of I_{SPTA} intensities tested ($126\,\mathrm{W/cm^2}$ to $1910\,\mathrm{W/cm^2}$), no lesioning occurred for exposures shorter than 1 s. This implies that no events of significance are missed in the first 650 ms before detection begins.

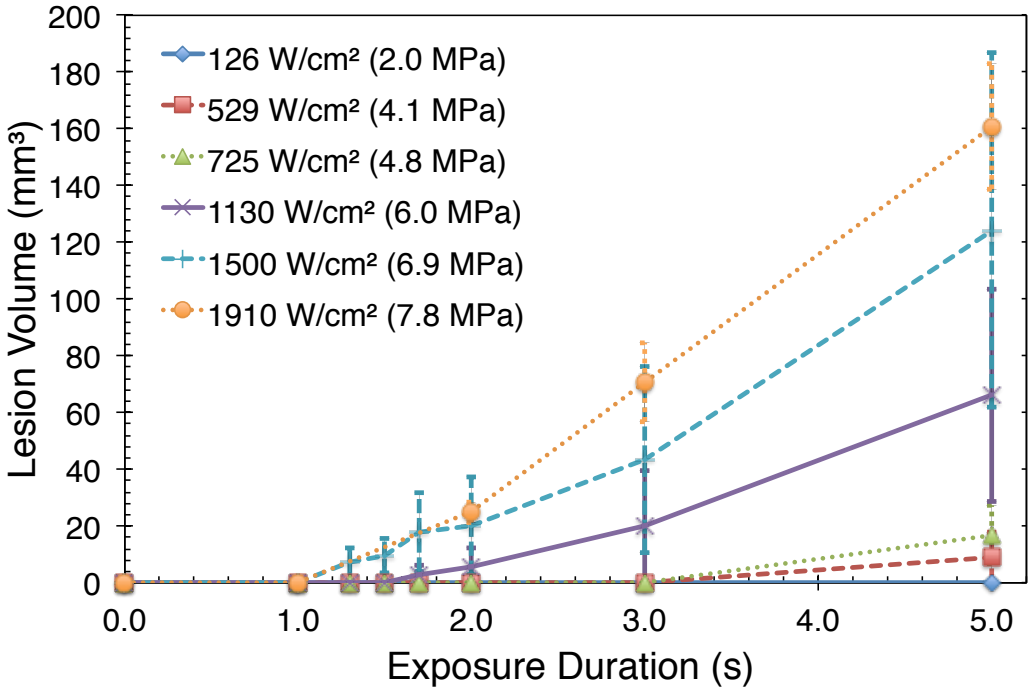

(a) *Average lesion volume as a function of exposure time.*

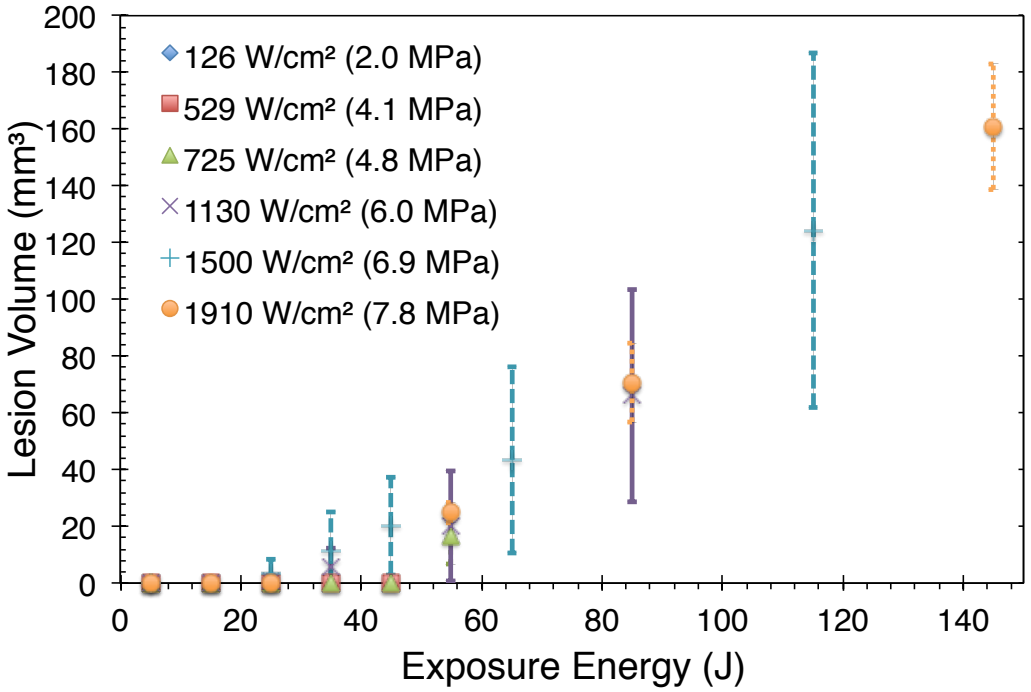

(b) *Average lesion volume as a function of exposure energy.*

Figure 6.6: *Average lesion volume as a function of exposure time and exposure energy. In both graphs, lesion volume is further split according to acoustic intensity (I_{SPTA}), with the corresponding pressure amplitude also indicated. For exposures that did not result in lesion formation, the lesion volume was recorded as zero. Standard deviations are indicated with error bars.*

6.3.2 Detector Performance and Sources of Error

The performance of the harmonic dip detector across all 212 exposures is shown in Table 6.3. For comparison, the performance of hyperecho monitoring in a HIFU ablation study by Yu and Xu [8] is also listed in this table (see Section 3.4.5, page 85 for a description of the hyperecho technique). It should be noted that there are important differences between the hyperecho study and the work presented here, including a much higher acoustic intensity in the former case ($I_{\mathrm{SATA}} = 14\,300\,\mathrm{W/cm^2}$, compared to at most $I_{\mathrm{SPTA}} = 1910\,\mathrm{W/cm^2}$ in this work) as well as different tissue types (*in vivo* rabbit liver in the hyperecho study versus *ex vivo* ox liver in this work). However, notwithstanding these differences, the harmonic dip detector is over 26% more accurate, 26% more sensitive, and 28% more specific than hyperecho monitoring. Moreover, if only the exposures at the highest acoustic intensity used in this study are considered in the comparison, the performance improvement is even greater: at $I_{\mathrm{SPTA}} = 1910\,\mathrm{W/cm^2}$, the accuracy, sensitivity, and specificity of the harmonic dip detector are all above 90%, while even at $I_{\mathrm{SATA}} = 14\,300\,\mathrm{W/cm^2}$, none of these measures of performance exceeds 50% with the hyperecho monitoring technique. The performance gap would likely increase further still if the harmonic dip detector were applied to exposures with an intensity comparable to that used in the hyperecho study, although in such a scenario it might also be necessary to use different detector parameters than those quoted here to accommodate the potentially shorter lesion formation time. Specifically, the value of t_{min} might need to be lowered to ensure that no lesions form before detection begins.

	Hyperecho Monitoring	Harmonic Dip Detection	
		All Exposures	I_{SPTA} = 1910 W/cm^2
True Negatives	6.4% (5 of 78)	32.5% (69 of 212)	20.0% (3 of 15)
True Positives	42.3% (33 of 78)	42.5% (90 of 212)	73.3% (11 of 15)
False Negatives	43.6% (34 of 78)	13.7% (29 of 212)	6.7% (1 of 15)
False Positives	7.7% (6 of 78)	11.3% (24 of 212)	0% (0 of 15)
Incidence of Lesioning	85.9% (67 of 78)	56.1% (119 of 212)	80.0% (12 of 15)
Accuracy	48.7% (38 of 78)	75.0% (159 of 212)	93.3% (14 of 15)
Sensitivity	49.3% (33 of 67)	75.6% (90 of 119)	91.7% (11 of 12)
Specificity	45.5% (5 of 11)	74.2% (69 of 93)	100% (3 of 3)

Table 6.3: *Performance comparison between the harmonic dip detector (ex vivo) and hyperecho monitoring (in vivo). The hyperecho performance data were taken from the work of Yu and Xu [8]; in that study, all exposures were performed in rabbit liver at the same acoustic intensity ($I_{SATA} = 14\,300\,W/cm^2$). Performance data for the dip detector is listed for all exposures, as well as those with the highest acoustic intensity employed in this study ($I_{SPTA} = 1910\,W/cm^2$).*

The performance of the harmonic dip detector is split according to exposure time in Figure 6.7a, as well as by exposure energy in Figure 6.7b. For exposure time, Figure 6.7a shows that the best performances occur for the 1 s and 5 s exposures, respectively the shortest and longest durations tested. The weakest performances occur at 1.3 s, 1.7 s, and 2 s; for times longer than these, it can be seen that the detection rate generally increases with exposure duration. Similarly, Figure 6.7b shows that with respect to exposure energy, the best performances occur above 60 J, while the worst performances originate from exposures delivering between 20 J and 60 J.

The high detector performance and low number of false positives at lower exposure times (less than 1 s) and at lower energy levels (less than 20 J) is consistent with the result that no lesions form under these conditions, as shown by the lesion

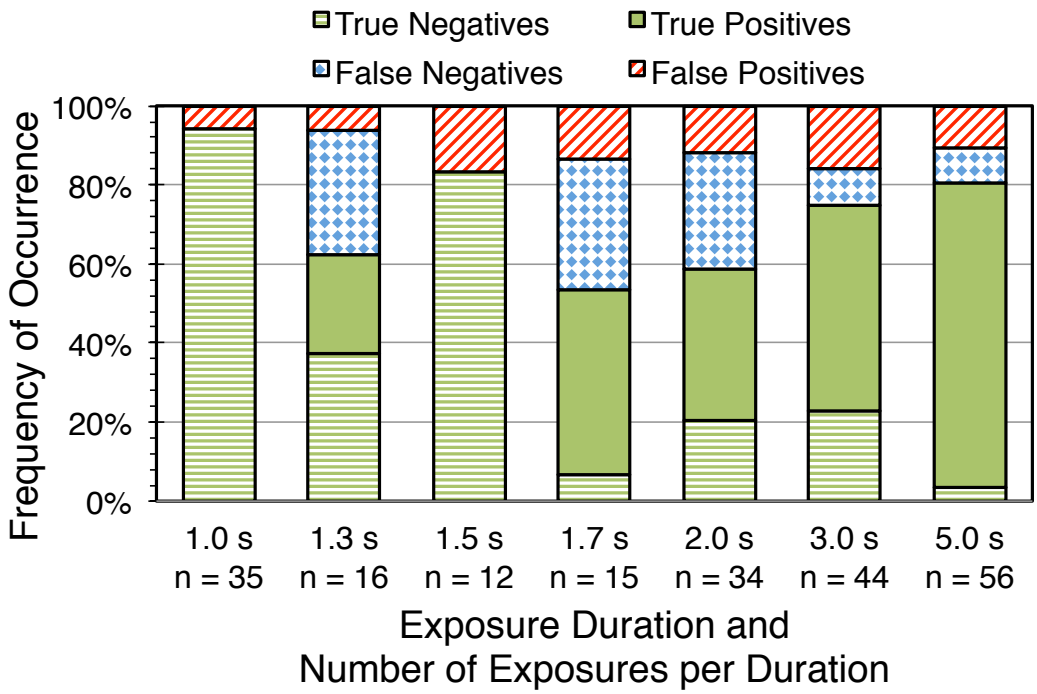

(a) *Detector performance, grouped by exposure time.*

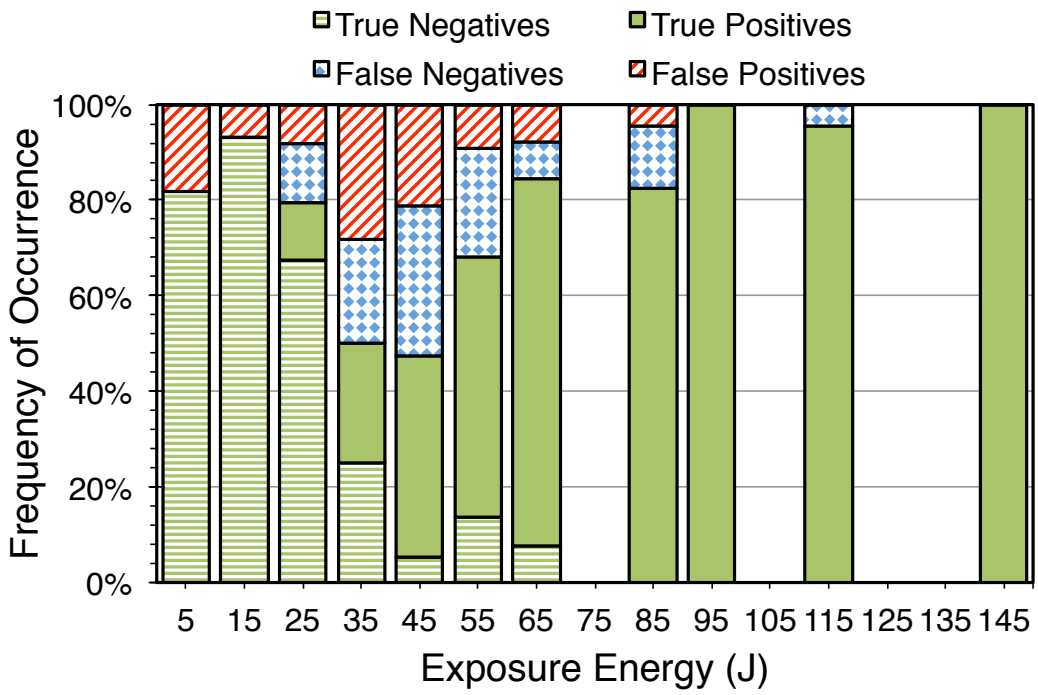

(b) *Detector performance, grouped by exposure energy. The bins on the horizontal axis are 10 J wide.*

Figure 6.7: *Detector performance versus exposure time and exposure energy.*

volume graphs in Figure 6.6 as well as by the absence of both true positives and false negatives in these intervals (hence, per Equation 6.6 on page 148, the incidence of lesioning is zero). This observation demonstrates that the detector functions correctly in the period preceding the onset of lesioning. Likewise, the high performance at longer exposure durations (3 s or more) and at higher energy levels (60 J or greater) shows that the detector performs well in regimes that are very likely to cause significant lesioning. On the other hand, the low performance at intermediate exposure times (1.3 s, 1.7 s, and 2 s) and at intermediate energies (between 20 J and 60 J) is likely because lesions are just beginning to form under these conditions. This explanation is consistent with a "minimum energy" being required to instigate lesioning, and is also supported by a number of observations that can be made upon closer inspection of the performance versus exposure duration results in Figure 6.7a. Firstly, the accuracy of the detector generally increases with exposure duration after 1.7 s, which is consistent with more lesions having had sufficient time to form properly and subsequently be identified by the detector. Secondly, as shown in Figure 6.6a, the volume of the lesions caused by exposures up to 2 s long is generally about 25 mm^3 or less. In comparison, Table 5.1 (page 129) shows that the −3 dB focal volume of the detector transducer ranges in size from 98 mm^3 to 1160 mm^3 across the frequencies that were examined for dips. Thus, many of the lesions that were created with shorter exposures may have simply been too small to detect relative to the sensitive volume of the detection transducer. Finally, in 13 of the 20 false negatives associated with intermediate times or intermediate energies, the start of a dip was observed close to the end of the exposure, but it appeared that the signal did

not have time to return above the threshold prior to the end of the exposure. This may indicate that the corresponding lesions formed soon after the HIFU was turned off: during this time, there were no longer any acoustic emissions to monitor at the focus, but the tissue would have continued to experience thermal damage until the heat that was deposited by the HIFU had dissipated. For exposures such as these, it is likely that the signal was not recorded during the time period in which the lesion actually formed, thereby resulting in a false negative rather than successful detection.

In summary, the detector performs well for exposures where significant lesioning is very likely to occur, without raising undue errors before lesions have started to form. The detection rate drops in the transition between these two states, where small lesions have just begun to appear. However, this is to be expected for the reasons mentioned previously, and in practice may be avoided by using a sufficiently long exposure with a high enough level of energy. This strategy, as well as other ways of mitigating the effect of detector errors in a clinical setting, is discussed next.

6.3.3 Consequences of Detector Errors and Mitigation Strategies

In practice, false negatives (where lesioning occurs but no dip is detected) are undesirable because of the misinformation conveyed to the operator. However, provided they do not occur so frequently as to make the detector impractical to use, false negatives do not present a danger to successful treatment in a clinical setting, as the surgeon could simply extend the exposure or perform an additional one. In the relatively unlikely event that no harmonic dip appeared in any of the sub-

sequent tries, this course of action could be repeated until a certain maximum total exposure time were reached. Using this strategy, false negatives would essentially result in overtreatment, not unlike the currently employed method of monitoring for hyperechogenic regions in 2-D ultrasound images taken post-exposure. However, in contrast to the latter technique, the total time lost to false negative overtreatment would likely be minimal, since Figure 6.7 as well as Table 6.3 show that false negatives occur only in a minority of exposures. Moreover, the decision to extend the exposure or perform an additional one can be made automatically near the end of the current exposure, meaning that the only extra delay caused by this strategy is the additional exposure time. This represents a considerable improvement over the hyperecho method, in which time is also lost acquiring and interpreting the 2-D ultrasound images in between exposures. Finally, using the aforementioned strategy, the amount of overtreatment induced by false negatives can be kept to a safe minimum by limiting the maximum exposure time; no such control is possible with hyperecho monitoring because of the systematic overtreatment that occurs with this technique (see the previous discussion in Section 3.4.5, page 85).

On the other hand, false positives (where a dip is detected but no lesion has formed) present a potentially greater danger in a clinical scenario, as these could lead to undertreatment. Figure 6.7b demonstrates that exposures with between 20 J and 60 J of energy are especially susceptible to this type of error. As mentioned previously, this is likely because lesions are just beginning to form at these energy levels for the HIFU frequency and the acoustic intensities used in this work. A straightforward solution to reduce the false positive rate is therefore to establish

appropriate minimum values for any two of the three key treatment parameters found in Equation 2.25 (page 44): exposure time, acoustic intensity, and exposure energy. The choice of values may be based on previous experience or empirical data: for example, Figures 6.6b and 6.7b show that under the conditions of this study, an exposure that delivers at least 80 J at an intensity of 1130 W/cm^2 will produce lesions averaging 66 mm^3 in size that will be detected with a false positive rate of less than 8%. An additional consideration specific to this study is the imprecision of the manual slicing technique used to assess lesioning, as some lesions may have been missed or been too small to detect. Moreover, combining the present detector with other real-time lesion detection methods described in Section 3.4 (page 75)—such as HMIFU [110]—could decrease the false positive rate even further.

Lastly, another means of reducing either type of detector error (false negative or false positive) is to choose a different set of detector parameters using Figure 6.5 (page 150). The reason this strategy works can be seen in Equations 6.8 and 6.9 (page 148): the former shows that increasing detector sensitivity results in fewer false negatives, while the latter demonstrates that increasing specificity reduces the number of false positives. However, the disadvantage of this error reduction strategy as compared to the others mentioned previously is that decreasing the rate of occurrence of one type of error will invariably increase the rate of occurrence of the other type. This originates from the trade-off between sensitivity and specificity seen in Table 6.2 (page 152) and Figure 6.5. For example, comparing points B and C in the table shows that the number of false negatives can be reduced by 8.5% at the expense of 10.9% more false positives, while point A shows that a false positive

rate of just 4.3% can be achieved if a false negative rate of 23.1% can be tolerated. It should also be noted that in practice, there are limits to how far this trade-off can be taken. On the one hand, an extreme reduction in the false negative rate would result in a large quantity of untreated tissue unbeknownst to the operator, which would not be acceptable in applications involving the ablation of cancerous tissue. On the other hand, excessively decreasing the number of false positives or attempting to eliminate them entirely would result in an impractical detector that would produce too many false negatives to be useful in an operating theatre. The optimal compromise between these two extremes depends on both the preferences of the operator as well as the nature of the application: the former determines how many false negatives can be tolerated in the operating room, while the latter dictates the maximum number of false positives that can be present without adversely affecting the success of the treatment (i.e. what percentage of tissue can be left unablated without the operator's knowledge). Nevertheless, Figure 6.5 demonstrates that there are a considerable number of acceptable operating points available for the harmonic dip detector, many of which yield a better performance (i.e. a higher sensitivity and also a higher specificity) than existing methods such as hyperecho monitoring.

6.3.4 Real-Time Implementation

Although the detector algorithm proposed here can be implemented in real time, in this study the emissions data from each HIFU exposure were only analysed after the exposure had been completed. A true real-time implementation, in which the algorithm would operate during HIFU exposure, would entail a number of additional

considerations, such as appropriate filter selection. However, provided that the magnitude of the frequency components between the harmonics remains orders of magnitude below the harmonics themselves, and that consecutive harmonics are well spaced out, a notch filter with a sufficiently rapid rolloff would be capable of extracting a given harmonic. The filtered signal would correspond approximately to a sinusoid at the frequency of the harmonic located in the passband of the filter. Straightforward demodulation in the form of envelope detection would then provide the time-varying magnitude of the harmonic during the exposure.

6.3.5 Potential Underlying Physical Mechanisms

Although the results shown in Figure 6.7 and Table 6.3 demonstrate that the presence of harmonic dips correlates well with the formation of lesions, further investigation into the physical mechanisms that underlie this correlation is required. Based on previous work, it is likely that a change in the viscoelastic or other material properties of the tissue is implicated in the physical explanation [31–34]. For example, the dips could be caused by the tissue absorbing energy as it undergoes the transition from reversible heat-induced stiffness change to the irreversible change in stiffness that marks the onset of tissue denaturation (see the earlier discussion on tissue necrosis and stiffness change in Section 3.4.4, page 82).

Given the high peak rarefaction pressures employed in this study, it is also possible that acoustic cavitation is occurring and is playing a role in changing the acoustic emissions at the focus during the exposure [53, 64, 160, 161]. If acoustic cavitation is involved, one possibility is that the cavitating microbubbles are acting

as nonlinear scatterers because of changes in their cavitation dynamics, which are in turn caused by changes in the viscoelastic properties of the surrounding medium. Alternatively, the microbubbles could be functioning as linear scatterers of an initially linear wave propagating in a nonlinear medium (i.e. there are harmonics present by the time the wave reaches the bubbles). In this case, the dips would be caused by a change in the nonlinearity coefficient (B/A) of the surrounding tissue as it stiffens because of irreversible denaturation. A confounding factor in distinguishing these two possibilities is the difficulty in separating the effects of nonlinear propagation (i.e. effects caused by the changes in the material properties of the medium; see Section 2.2.2, page 33) from those caused by changing bubble dynamics (discussed previously in Section 2.2.3, page 35). In fact, both types of effect may be present simultaneously [161, 162]. Further experiments are therefore required to ascertain the role acoustic cavitation plays in causing the observed correlation between dips in the signal harmonics and lesioning in the tissue.

6.3.6 Potential Application and Benefits to Clinical Medicine

Although the tissue model employed in this work was designed to replicate clinical treatments as closely as possible using *ex vivo* tissue, further testing on *in vivo* or perfused tissue is required to determine if dips in the harmonics of the focal emissions also occur with lesioning in such environments. With appropriate sensors, it would even be possible to test data acquired passively during exposures in humans, although in that case an alternative measure of lesion formation would be required for assessing detector performance.

Nevertheless, if harmonic dip detection does prove applicable to *in vivo* tissue, the technique proposed in this work would represent a significant improvement over currently used monitoring techniques, as illustrated by the performance comparison with hyperecho monitoring in Table 6.3. Using the harmonic dip detector to monitor treatment could therefore reduce the collateral damage to healthy tissue caused by overtreatment, as well as decrease treatment time and cost. As an added bonus, existing monitoring techniques such as hyperecho monitoring and MR thermometry could also continue to be used alongside harmonic dip detection if desired. Such a multi-detector approach would help facilitate the transition for clinicians by providing them with a backup monitoring method that they would already be familiar with, and by extension guarantee that treatment efficacy does not decrease compared to current practice during the transition period.

6.4 Conclusions

The results in this chapter demonstrate that lesioning in *ex vivo* ox liver tissue is highly correlated with the presence of pronounced local minima ("dips") in the harmonics of the passively monitored acoustic emissions at the HIFU focus. A detector based on this observation that enables real-time monitoring of lesion formation in *ex vivo* ox liver was also designed, optimised, and validated. The detector predicted lesioning with over 80% accuracy in regimes that were very likely to create lesions (60 J of acoustic energy or more), and had an error rate of less than 6% for exposures that were too short to cause lesioning (up to 1 s long). The overall sensitivity and specificity of the detector were 75.6% and 74.2%, respectively. The proposed

detector could therefore provide a low-cost means of effectively monitoring clinical HIFU treatments passively and in real time. This detector also has the significant advantage of not requiring thermometry, which can be difficult to obtain during *in vivo* HIFU treatments.

Chapter 7

Conclusions and Future Work

In this closing chapter, the key findings and novel contributions of this work are summarised. The implications of these findings for future work are also discussed, including their potential role in the creation of an automated, real-time HIFU control system.

7.1 Summary of Key Findings

The main objective of this work was to develop improved metrics of HIFU-induced biological damage that are specifically suited to monitoring and controlling HIFU ablation. Through the experimental work described in the previous three chapters, this objective was met for proteins, cells, and tissue.

In Chapter 4, an optical method that enables the straightforward quantification of thermal damage in protein-embedding hydrogels was developed and was shown to be biologically relevant by comparing its value to the damage sustained by cancer

cells across a range of temperature profiles. The amount of protein damage was also found to be dependent on the maximum temperature reached as well as the rate of heating.

In Chapter 5, hydrogels embedded with different cell lines were used to assess the performance of most widely used model of heat-induced cell death ($CEM_{43\,^\circ C}$) objectively across a range of HIFU-relevant conditions. It was shown that, while the $CEM_{43\,^\circ C}$ model can be made to work in a specific temperature range and for a specific cell line, the amount of cell death caused by a given temperature profile varies across cell lines in general. Moreover, it was also demonstrated that the mechanically induced cell death neglected by the model can greatly undermine its accuracy when the peak rarefaction pressure is high enough to permit significant damage from inertial cavitation to occur (5 MPa for 3 s or more in this work). These results show that damage models based solely on temperature are unable to provide a complete description of HIFU-induced damage in tissue, which can be comprised of multiple cell lines in the case of metastatic cancers.

Finally, in Chapter 6, a novel, passive acoustic technique designed for real-time monitoring of HIFU-induced tissue damage was developed. Based on a study of over 200 exposures in freshly excised ox liver, it was found that the successful formation of HIFU lesions is highly correlated with the presence of pronounced dips in the magnitude of the acoustic emissions at the HIFU focus at integer multiples of the insonation frequency. A detector based on this observation predicted lesioning with over 80% accuracy in regimes that were very likely to create lesions (60 J of acoustic energy or more), and had an error rate of less than 6% for exposures that were too

short to cause lesioning (up to 1 s long). The overall sensitivity and specificity of the detector were 75.6% and 74.2%, respectively. The proposed detector could therefore provide a low-cost means of effectively monitoring clinical HIFU treatments passively and in real time.

In summary, this work has contributed to improving the available methods of monitoring HIFU-induced biological damage in proteins, cells, and tissue. Several potential applications of these contributions to future work are discussed in the next section.

7.2 Future Work

7.2.1 Controlling HIFU Therapy Automatically and in Real Time

Perhaps the most natural application of the enhanced damage monitoring methods developed in this work lies in the automated (or semi-automated) control of HIFU therapy. With automated control, the HIFU ablation system could be designed to stop the exposure when a certain condition is met or when a certain threshold is passed, without the need for further intervention by the clinician. This would make HIFU surgery easier to perform and could help increase the clinical adoption of the technique.

The control system could be designed to function using a normalised degree of damage (e.g. a value from 0% to 100%). With this approach, the same control system could be used with many different damage metrics and biological media (e.g. different types of tissue), provided that the correct normalisation function is used

in each case. Other issues to consider include the selection of a model for the plant (e.g. an Auto-Regressive Moving Average difference equation or a neural network), as well as choosing unbiased estimators for any model parameters [159].

7.2.2 Developing and Validating Advanced Thermal Dose Metrics

The experimental setup designed in Chapter 5 provides a versatile tool for obtaining objective measurements of HIFU-induced thermal and mechanical cell death. Although this setup was only used to assess the commonly employed version of the $\mathrm{CEM}_{43\,^{\circ}\mathrm{C}}$ model in this work, it could also be coupled with some of the more advanced models of thermal dose discussed in Section 3.3.3 (page 65), or be used to develop entirely new dose models that are better suited to HIFU ablation. For example, with additional testing, it would be possible to determine the appropriate activation energies and breakpoints for Arrhenius-based thermal dose models (such as CEM) above 54 °C.

The HIFU setup used in this work (see Section 5.2.3, page 125) can also be modified to test conditions in which both thermally induced cell death and mechanically induced cell death occur simultaneously. Notably, the data that would be acquired under such conditions could potentially be used to develop a model of HIFU-induced damage that incorporates the effect of cavitation. To allow both types of damage to occur simultaneously, the cell phantom would need to be insulated from the surrounding water in the HIFU tank using an acoustically transparent substance, such as the polyacrylamide hydrogel described in Section 4.2.3 (page 100). Glass microspheres could also be suspended in the cell phantoms at the time they are cast to

increase the attenuation at the focus. However, although attempts were made to realise these ideas in the context of the present work, accurate thermometry could not be obtained with the available equipment because of the constant occurrence of cavitation on the thin-wire thermocouples used to monitor the temperature at the HIFU focus. In future work, a non-invasive temperature measurement device—such as an infrared camera—could be used to avoid this problem.

7.2.3 Enhancing the Detection of HIFU-Induced Lesions *in Vivo*

As mentioned in Section 6.3 (page 152), many improvements could be made to the tissue lesioning detector developed in Chapter 6. These include developing a true real-time implementation of the algorithm (discussed in Section 6.3.4), determining the physical mechanisms that underlie the operation of the detector (Section 6.3.5), and testing the detector on *in vivo* or perfused tissue (Section 6.3.6). Finally, as mentioned previously in Chapter 6, the design of the harmonic dip detector allows it to work alongside many other monitoring techniques discussed in Section 3.4 (page 75), including MRI, ultrasound hyperecho imaging, and elastographic methods such as HMIFU. Such a multi-detector approach would likely yield better results than any single indicator of tissue damage, and could eventually provide the real-time, accurate, convenient, and low-cost monitoring that is needed to enable the widespread clinical use of HIFU cancer therapy.

Appendices

Appendix

List of Publications

A.1 Peer-Reviewed Journal Articles

- **S. D. Nandlall**, E. Jackson, and C.-C. Coussios. *Real-Time Passive Acoustic Monitoring of HIFU-Induced Tissue Damage*. Ultrasound in Medicine and Biology, volume 37, number 6, pages 922–934, June 2011. DOI: 10.1016/j.ultrasmedbio.2011.02.016.

- **S. D. Nandlall**, H. A. Schiffter, S. Vonhoff, M. Bazán-Peregrino, M. Arora, and C.-C. Coussios. *Real-Time Optical Measurement of Biologically Relevant Thermal Damage in Tissue-Mimicking Hydrogels Containing Bovine Serum Albumin*. International Journal of Hyperthermia, volume 26, number 5, pages 456–464, August 2010. DOI: 10.3109/02656731003789292.

A.2 Peer-Reviewed Abstracts

The following list includes presentations, posters, and proceedings papers that were presented at international conferences.

- **S. D. Nandlall**, M. Bazán-Peregrino, S. Mo, and C.-C. Coussios. *Determination of Cytotoxic Thermal Dose During HIFU Ablation.* In: E. E. Konofagou and R. Muratore (editors), *Proceedings of the 11th International Symposium on Therapeutic Ultrasound*, American Institute of Physics, in press. Conference held in New York, NY, USA on 10–13 April 2011.

- **S. D. Nandlall**, E. Jackson, and C.-C. Coussios. *Real-Time Passive Acoustic Monitoring of Tissue Damage During Thermal Ablation by High-Intensity Focused Ultrasound.* Presented at the 160$^{\text{th}}$ Meeting of the Acoustical Society of America and 2$^{\text{nd}}$ Pan-American/Iberian Meeting on Acoustics in Cancún, Mexico on 15–19 November 2010. DOI: 10.1121/1.3508627.

- C.-C. Coussios, M. Gyöngy, R. Ritchie, I. R. Webb, **S. D. Nandlall**, E. Jackson, C. D. Arvanitis, M. Bazán-Peregrino, and M. Arora. *Passive Mapping for Real-Time Monitoring of Ultrasound Therapy.* Presented at the 160$^{\text{th}}$ Meeting of the Acoustical Society of America and 2$^{\text{nd}}$ Pan-American/Iberian Meeting on Acoustics in Cancún, Mexico on 15–19 November 2010. DOI: 10.1121/1.3508622.

- **S. D. Nandlall**, H. A. Schiffter, S. Vonhoff, M. Arora, and C.-C. Coussios. *Correlation of Optically Observable Thermal Damage with Protein Denatur-*

ation in a Tissue-Mimicking Hydrogel. Presented at the Society of Thermal Medicine 2009 Annual Meeting in Tucson, AZ, USA on 3–7 April 2009.

- **S. D. Nandlall**, M. Arora, H. A. Schiffter, and C.-C. Coussios. *On the Applicability of the Thermal Dose Cumulative Equivalent Minutes Metric to the Denaturation of Bovine Serum Albumin in a Polyacrylamide Tissue Phantom.* In: E. S. Ebbini (editor), *Proceedings of the 8th International Symposium on Therapeutic Ultrasound*, volume 1113, number 1, pages 205–209, American Institute of Physics, 2009. Conference held in Minneapolis, MN, USA on 10–13 September 2008. DOI: 10.1063/1.3131414.

Appendix

B

Table of Acoustic Properties

The following table lists the speeds of sound (Section 2.1.5, page 23), characteristic acoustic impedances (Section 2.1.6, page 25), and 1 MHz attenuation coefficients (Section 2.1.7, page 27) of various substances, including all those exposed to ultrasound in this work. Sources: [37, 43, 44, 77, 79, 80, 106, 163–166].

Substance		Speed of Sound (c, m/s)	Impedance (Z, MPa·s/m)	Attenuation at 1 MHz (α, Np/m)
Water	**at 20°C**	1482.2	1.48	0.03
	at 37°C	1523.7	1.51	0.02
Agar 2% w/v	**at 20°C**	1542	1.48	2.1
	at 37°C	1559	1.49	1.6
Polyacrylamide 7% w/v	**at 20°C**	1544	1.61	1.6
	at 37°C	1576	1.62	0.8
Liver 37°C	**bovine**	1600	1.76	5.0
	canine	1601	1.76	4.4
	human	1595	1.75	4.5
	porcine	1588	1.75	2.3

Appendix

Mathematical Definition of T_n Spatial Descriptors

In Section 3.3.3 (page 65), the concept of T_n spatial temperature descriptors were introduced; however, only an informal definition of these descriptors was provided. In this appendix, a mathematically rigorous definition of T_n descriptors will be developed using measure theory, with the aim of providing a solid basis for performing computations with these quantities.

C.1 A Formal Definition of T_n Descriptors

As mentioned in Definition 3.3 (page 71), the informal definition of the T_n spatial descriptor is the n^{th} percentile of the temperature distribution by tissue volume ($0 \leq n \leq 100$). Hence, if a tissue has a T_{90} temperature of 65 °C, this means that at least 90% of the tissue volume is at a temperature equal to or greater than 65 °C. This intuitive definition may be formalised using sets and measure theory, as stated next.

Definition C.1 (A Formal Definition of T_n Descriptors)

Let:

- V be a bounded, nonempty subset of $\mathbb{R}^3$ that corresponds to the volume occupied by the tissue;
- n be any number from 0 to 100 inclusively;
- $T(P)$ denote the value of the tissue's spatial temperature distribution at any point $P \in V$;
- $\mathcal{P}(V)$ denote the power set of V, i.e. the set of all possible subsets of V;
- $\mu(.)$ denote the set measure function, i.e. a function that returns the volume of the set passed to it; and
- C_n denote the set of all subsets of V, except for the empty set, whose measure equals or exceeds $n\%$ of the measure of V, i.e.

$$C_n = \left\{ S \in \mathcal{P}(V) - \varnothing \,:\, \mu(S) \geq \frac{n}{100}\mu(V) \right\}. \tag{C.1}$$

Then the T_n spatial temperature descriptor of the tissue is defined as

$$T_n = \sup_{S \in C_n} \left(\inf_{P \in S} T(P) \right). \tag{C.2}$$

This definition states that the T_n temperature may be found by considering all subsets of the tissue volume whose size is at least $n\%$ of this total volume and finding

the lowest temperature for each subset. The largest of these lower bounds then represents the highest temperature exceeded by at least $n\%$ of the tissue volume.

Although Definition C.1 is mathematically rigorous, it is not a practical one to work with directly, since the number of sets to minimise the temperature distribution over grows exponentially with the number of points in V, and may even be uncountably infinite. Hence, it is desirable to develop simplified formulae for finding the value of the T_n descriptor in commonly encountered cases. Two such situations are the T_0 and T_{100} descriptors, which are discussed in the next two sections.

C.2 Derivation of a Simplified Formula for T_0

Intuitively, the T_0 descriptor might be expected to correspond to the maximum temperature achieved in the tissue volume, or the smallest temperature exceeded by "0%" of the tissue. This is indeed the case, as proven in the following theorem.

THEOREM C.1 (A SIMPLIFIED FORMULA FOR T_0)

In the case of the T_0 descriptor, Equation C.2 simplifies as follows if the temperature distribution achieves a maximum value at least once over V:

$$T_0 = \max_{P \in V} T(P).$$

PROOF:

Setting $n = 0$ in the expression for the set C_n stated in Equation C.1 yields

$$C_0 = \{S \in \mathcal{P}(V) - \varnothing \,:\, \mu(S) \geq 0\} = \mathcal{P}(V) - \varnothing.$$

Hence, it is possible to substitute $\mathcal{P}(V) - \varnothing$ for C_0 in Equation C.2, which yields

$$T_0 = \sup_{S \in \mathcal{P}(V) - \varnothing} \left(\inf_{P \in S} T(P) \right). \tag{C.3}$$

Let P^* be any point at which the temperature reaches is maximum value in V, i.e. define

$$P^* = \arg\max_{P \in V} T(P). \tag{C.4}$$

Since it was assumed that $T(.)$ achieves its maximum at least once over V, at least one value of P^* is guaranteed to exist. If there is more than one point returned by the arg max function (which will occur if $T(.)$ achieves its maximum value at more than one point in V), then designate any single one of these points as P^*.

Two cases will now be considered: one where the volume V contains only one point, and one where it contains at least two distinct ones. In the former case, the single point contained in V will be the point P^* defined in Equation C.4. It follows that the only possible subsets of V in this case are the empty set and $\{P^*\}$, and hence $\mathcal{P}(V) - \varnothing = \{\varnothing, \{P^*\}\} - \varnothing = \{\{P^*\}\}$. Directly substituting this result into Equation C.3 yields

$$\begin{aligned}
T_0 &= \sup_{S \in \{\{P^*\}\}} \left(\inf_{P \in S} T(P) \right) \\
&= \sup \left\{ \inf_{P \in \{P^*\}} T(P) \right\} \\
&= \sup \{\inf\{T(P^*)\}\} \\
&= T(P^*) \\
&= \max_{P \in V} T(P).
\end{aligned}$$

Equation C.1 has therefore been verified for the case where the volume V contains only one point. On the other hand, if there are at least two distinct points in V, then let S^* be the subset of $\mathcal{P}(V) - \varnothing$ that contains only the maximum point P^*, i.e. define $S^* = \{P^*\}$. Because V contains more than one point, it follows that $\mathcal{P}(V) - \varnothing$ also contains sets other than S^* (such as the set that contains the second distinct point). Hence, the set $(\mathcal{P}(V) - \varnothing) - S^*$ is not empty, and $\mathcal{P}(V) - \varnothing$ can be partitioned into the two nonempty sets S^* and $(\mathcal{P}(V) - \varnothing) - S^*$. Using this partition to expand Equation C.3 yields

$$\begin{aligned} T_0 &= \sup\left(\left\{\inf_{P\in S^*} T(P)\right\} \cup \left[\bigcup_{S\in(\mathcal{P}(V)-\varnothing)-S^*} \left\{\inf_{P\in S} T(P)\right\}\right]\right) \\ &= \sup\left(\{T(P^*)\} \cup \left[\bigcup_{S\in(\mathcal{P}(V)-\varnothing)-S^*} \left\{\inf_{P\in S} T(P)\right\}\right]\right) \\ &= \max\left(\sup\left(T(P^*)\right), \sup_{S\in(\mathcal{P}(V)-\varnothing)-S^*} \left[\inf_{P\in S} T(P)\right]\right) \\ &= \max\left(T(P^*), \sup_{S\in(\mathcal{P}(V)-\varnothing)-S^*} \left[\inf_{P\in S} T(P)\right]\right). \end{aligned} \tag{C.5}$$

For any point P in V, $T(P) \leq T(P^*)$ since P^* is a maximum of the temperature function over all of V according to its definition in Equation C.4. Hence

$$\sup_{S\in(\mathcal{P}(V)-\varnothing)-S^*} \left(\inf_{P\in S} T(P)\right) \leq T(P^*).$$

This inequality shows that the first term in the max function in Equation C.5 is greater than or equal to the second, from which it follows that

$$T_0 = T(P^*) = \max_{P\in V} T(P).$$

This verifies Equation C.1 in the case where the volume V contains more than one point, which completes the overall proof of this theorem.

Q.E.D.

It should be noted that Theorem C.1 only applies if the temperature function actually achieves a defined maximum over the tissue volume V. This limitation does not affect most situations of practical interest, in which the temperature distribution is typically measured at a finite number of points (see Section C.4, page 183). However, in theoretical thermal dose calculations, it may not always be the case that the temperature function achieves a defined maximum over its domain V. This can occur if the volume V is open, as in the following hypothetical example:

$$V = \{(x, y, z) : 0 \leq x, y, z < 1\},$$

$$T(x, y, z) = xyz.$$

Here, the temperature function $T(x, y, z)$ has no defined maximum since V is an open interval of $\mathbb{R}^3$, and hence Theorem C.1 does not apply. In cases such as these, Equation C.3 must be employed to find T_0.

C.3 Derivation of a Simplified Formula for T_{100}

Just as the T_0 descriptor corresponds to the maximum temperature in the tissue volume, it might be expected that T_{100} should correspond to the minimum temperature, or the temperature exceeded by "100%" of the tissue. As the following

theorem shows, this intuition is essentially correct; however, an additional qualification is necessary to state this result rigorously in measure-theoretic terms.

THEOREM C.2 (A FORMULA FOR T_{100})

In the case of the T_{100} descriptor, the formula in Equation C.2 simplifies as follows:

$$T_{100} = \operatorname*{ess\,inf}_{P \in V} T(P).$$

PROOF:

Setting $n = 100$ in the expression for the set C_n stated in Equation C.1 yields

$$C_{100} = \{S \in \mathcal{P}(V) - \varnothing \,:\, \mu(S) \geq \mu(V)\}.$$

Since no subset of V can be larger than V itself, only the subsets of V that have the same measure as V will satisfy the aforementioned condition. This includes the set V itself, as well as V less any subset of measure zero. The following equivalent expression may therefore be written for C_{100}:

$$C_{100} = \{V - M \,:\, [M \in \mathcal{P}(V)] \wedge [\mu(M) = 0]\}.$$

Using this alternate formula for C_{100}, Equation C.2 becomes

$$\begin{aligned} T_{100} &= \sup_{S \in C_{100}} \left(\inf_{P \in S} T(P) \right) \\ &= \sup_{M \in \mathcal{P}(V):\mu(M)=0} \left(\inf_{P \in (V-M)} T(P) \right). \end{aligned}$$

In the previous equation, the set whose supremum is being taken is a collection of all possible essential lower bounds for $T(.)$ over V, or values that are exceeded everywhere in V except on a set of measure zero. The supremum of this set, which corresponds to the highest possible essential lower bound, is by definition the essential infinimum of $T(.)$ over V.

Q.E.D.

Theorem C.2 shows that the T_{100} temperature is the essential minimum of the temperature function over the volume. This is not always the same as the (absolute) minimum, as the temperature distribution may in fact take on values less than the essential minimum at certain points; however, the measure of the set of points over which this happens is guaranteed to be zero. Mathematically, T_{100} is said to be the highest temperature value that is exceeded "almost everywhere" in the set. This distinction is academic for most cases of practical interest, where the temperature distribution is typically sampled at only a finite number of locations (a situation discussed in the next section). However, the difference between the essential and actual minimum may be important for theoretical thermal dose calculations on certain types of temperature distributions or volumes.

C.4 T_n Descriptors of Sampled Distributions

The theorem in this section provides a formula for easily computing T_n descriptors in situations where the temperature distribution consists of measurements at a finite number of points in space. This case covers most situations encountered in engineering applications of T_n descriptors. As will be shown shortly, the result corresponds

to what might be expected from the intuitive definition of T_n descriptors given in Section 3.3.3 (page 71).

THEOREM C.3 (T_n DESCRIPTORS OF SAMPLED DISTRIBUTIONS)

Consider the situation described in Definition C.1, and suppose that the tissue volume V consists of a finite number N of distinct points labelled $P_1, P_2, \ldots, P_N$. Assume without loss of generality that these points have been indexed in decreasing order of temperature, so that

$$T(P_1) \geq T(P_2) \geq \cdots \geq T(P_N). \tag{C.6}$$

Let the set measure function $\mu(.)$ be proportional to the number of points contained in the set that it operates on. Thus, if a subset S of V contains $\eta(S)$ points, the measure of S will be

$$\mu(S) = \frac{\eta(S)}{N}\mu(V). \tag{C.7}$$

Then the value of the T_n spatial temperature descriptor is $T(P_k)$, where

$$k = \begin{cases} 1 & \text{if } n = 0 \\ \left\lceil \frac{n}{100} N \right\rceil & \text{otherwise} \end{cases} \tag{C.8}$$

and where the brackets indicate rounding up to the nearest integer.

PROOF:

According to Theorem C.1, T_0 is the maximum of $T(.)$ over V, which is $T(P_1)$ in this situation. This covers the $n = 0$ case of Equation C.8, and so it will be assumed that $n > 0$ for the remainder of this proof.

Substituting the expression for $\mu(S)$ given in Equation C.7 into the formula for the set C_n stated in Equation C.1 yields

$$\begin{aligned} C_n &= \left\{ S \in \mathcal{P}(V) - \varnothing \,:\, \frac{\eta(S)}{N}\mu(V) \geq \frac{n}{100}\mu(V) \right\} \\ &= \left\{ S \in \mathcal{P}(V) - \varnothing \,:\, \eta(S) \geq \frac{n}{100}N \right\}. \end{aligned}$$

This implies that a subset of V can only be in C_n if it contains at least m points, where

$$m = \left\lceil \frac{n}{100}N \right\rceil.$$

Since n has been taken to be strictly greater than zero, it follows from this equation that the value of m must be at least 1.

Let S_m be the set that contains the first m points in V, i.e. $S_m = \{P_1, P_2, \ldots, P_m\}$. This set is guaranteed to contain at least one point (since $m \geq 1$), and must also be a member of C_n (because it has been defined such that it contains the minimum number of points required for inclusion in C_n). Since the points in V have been indexed in decreasing order of temperature (as stated in Equation C.6), the lowest temperature in the set S_m will occur at the point P_m, and hence

$$\inf_{P \in S_m} T(P) = T(P_m). \tag{C.9}$$

Two cases will now be considered: one where the set C_n only contains the set S_m, and one where it contains other sets as well. In the former case, direct application of Equation C.2 in Definition C.1 yields

$$\begin{aligned} T_n &= \sup_{S \in C_n} \left(\inf_{P \in S} T(P) \right) \\ &= \sup \left\{ \inf_{P \in S_m} T(P) \right\} \\ &= \inf_{P \in S_m} T(P) \\ &= T(P_m) \end{aligned}$$

where last line follows from Equation C.9. This verifies the second case of Equation C.8 when the set C_n only contains the set S_m.

On the other hand, if C_n contains sets other than S_m, the set $C_n - S_m$ will be nonempty. Hence, C_n can be partitioned into the two nonempty sets S_m and $C_n - S_m$. This partition can be used to expand Equation C.2 as follows:

$$\begin{aligned} T_n &= \sup_{S \in C_n} \left(\inf_{P \in S} T(P) \right) \\ &= \sup \left(\left\{ \inf_{P \in S_m} T(P) \right\} \cup \left[\bigcup_{S \in C_n - S_m} \left\{ \inf_{P \in S} T(P) \right\} \right] \right) \\ &= \sup \left(\{T(P_m)\} \cup \left[\bigcup_{S \in C_n - S_m} \left\{ \inf_{P \in S} T(P) \right\} \right] \right) \\ &= \max \left(\sup\{T(P_m)\}, \sup_{S \in C_n - S_m} \left[\inf_{P \in S} T(P) \right] \right) \\ &= \max \left(T(P_m), \sup_{S \in C_n - S_m} \left[\inf_{P \in S} T(P) \right] \right) \end{aligned} \tag{C.10}$$

where the third line again follows from Equation C.9. All of the sets in $C_n - S_m$ contain at least m points but must be distinct from S_m. Since S_m already contains

the first m points of V, it follows that every set in $C_n - S_m$ must contain at least one point having an index greater than m. As mentioned before, the points have been indexed in decreasing order of temperature (as per Equation C.6), and so the temperature at any point whose index is higher than m cannot exceed $T(P_m)$. Therefore, any set $S \in C_n - S_m$ contains at least one point whose temperature is at most $T(P_m)$, which implies that

$$\forall\, S \in C_n - S_m \;:\; \inf_{P \in S} T(P) \leq T(P_m).$$

This logical statement is in fact equivalent to the following inequality:

$$\sup_{S \in C_n - S_m} \left(\inf_{P \in S} T(P) \right) \leq T(P_m).$$

This inequality shows that the first term in the max function in Equation C.10 is greater than or equal to the second, and once again it follows that $T_n = T(P_m)$. This verifies the second case of Equation C.8 when the set C_n contains sets other than S_m, which completes the overall proof of this theorem.

Q.E.D.

The practical interpretation of Theorem C.3 is that it provides an algorithm for finding the value of the T_n descriptor in a temperature distribution that contains a finite number of points, assuming that each point covers an equal area of the overall volume. This algorithm consists of sorting the temperature distribution in descending order and finding the temperature at the point whose rank is given by Equation C.8. This point is simply the one corresponding to the n^{th} percentile of

the distribution, or the point with the next-lowest temperature if there is no sample exactly on this percentile. This corresponds to what might be expected from the informal definition of the T_n descriptor stated in Definition 3.3 (page 71).

In cases where there is no point exactly on the n^{th} percentile, it may also be advisable to interpolate the distribution before applying this algorithm in order to improve the estimate of T_n. This additional step will yield better results if the number of sample points is large and if the temperature distribution is smooth (i.e. if the variation between two adjacent samples is acceptably small).

References

[1] J. E. Kennedy. *High-Intensity Focused Ultrasound in the Treatment of Solid Tumours*. Nature Reviews Cancer, vol. 5, pp. 321–327, April 2005.

[2] G. R. ter Haar and C.-C. Coussios. *High Intensity Focused Ultrasound: Past, Present and Future*. International Journal of Hyperthermia, vol. 23, no. 2, pp. 85–87, January 2007.

[3] C.-C. Coussios and R. A. Roy. *Applications of Acoustics and Cavitation to Noninvasive Therapy and Drug Delivery*. Annual Review of Fluid Mechanics, vol. 40, pp. 395–420, 2008.

[4] X. He and J. C. Bischof. *Quantification of Temperature and Injury Response in Thermal Therapy and Cryosurgery*. Critical Reviews in Biomedical Engineering, vol. 31, pp. 355–422, 2003.

[5] G. R. ter Haar and C.-C. Coussios. *High Intensity Focused Ultrasound: Physical Principles and Devices*. International Journal of Hyperthermia, vol. 23, no. 2, pp. 89–104, January 2007.

[6] F. Wu, Z.-B. Wang, W.-Z. Chen, H. Zhu, J. Bai, J.-Z. Zou, K.-Q. Li, C.-B. Jin, F.-L. Xie, and H.-B. Su. *Extracorporeal High Intensity Focused Ultrasound Ablation in the Treatment of Patients with Large Hepatocellular Carcinoma*. Annals of Surgical Oncology, vol. 11, no. 12, pp. 1061–1069, 2004.

[7] J. E. Kennedy, F. Wu, G. R. ter Haar, F. V. Gleeson, R. R. Phillips, M. R. Middleton, and D. Cranston. *High-Intensity Focused Ultrasound for the Treatment of Liver Tumours*. Ultrasonics, vol. 42, pp. 931–935, 2004.

[8] T. Yu and C. Xu. *Hyperecho as the Indicator of Tissue Necrosis During Microbubble-Assisted High Intensity Focused Ultrasound: Sensitivity, Specificity and Predictive Value*. Ultrasound in Medicine and Biology, vol. 34, no. 8, pp. 1343–1347, 2008.

[9] The HAIFU Technology Company. *Chongquing, People's Republic of China*. World Wide Web (http://www.haifu-hifu.co.uk/Products/ModelJC.asp), June 2011.

[10] M. R. Bailey, V. A. Khokhlova, O. A. Sapozhnikov, S. G. Kargl, and L. A. Crum. *Physical Mechanisms of the Therapeutic Effect of Ultrasound (A Review)*. Acoustical Physics, vol. 49, no. 4, pp. 369–388, November 2003.

[11] I. Rivens, A. Shaw, J. Civale, and H. Morris. *Treatment Monitoring and Thermometry for Therapeutic Focused Ultrasound*. International Journal of Hyperthermia, vol. 23, no. 2, pp. 121–139, January 2007.

[12] C. Lafon, G. Bouchoux, R. Souchon, and J.-Y. Chapelon. *Monitoring and Follow up of HIFU Lesions by Ultrasound.* In: *Proceedings of the 4th IEEE International Symposium on Biomedical Imaging*, pp. 1068–1071, 2007.

[13] X. Zheng and S. Vaezy. *An Acoustic Backscatter-Based Method for Localization of Lesions Induced by High-Intensity Focused Ultrasound.* Ultrasound in Medicine and Biology, vol. 36, no. 4, pp. 610–622, 2010.

[14] D. Hanahan and R. A. Weinberg. *The Hallmarks of Cancer.* Cell, vol. 100, pp. 57–70, January 2000.

[15] C. D. Mathers and D. Loncar. *Projections of Global Mortality and Burden of Disease from 2002 to 2030.* Public Library of Science Medicine, vol. 3, no. 11, pp. 2011–2030, November 2006.

[16] D. M. Parkin, F. Bray, J. Ferlay, and P. Pisani. *Global Cancer Statistics, 2002.* CA: A Cancer Journal for Clinicians, vol. 55, pp. 74–108, 2005.

[17] J. R. Stewart. *Prospects for Hyperthermia in Cancer Therapy.* In: M. Urano and E. Douple (editors), *Hyperthermia and Oncology*, vol. 1 (Thermal Effects on Cells and Tissues), chap. 1, pp. 1–12. VSP B.V., Zeist, The Netherlands, 1988.

[18] J. F. Edd, L. Horowitz, R. V. Davalos, L. M. Mir, and B. Rubinsky. *In Vivo Results of a New Focal Tissue Ablation Technique: Irreversible Electroporation.* IEEE Transactions on Biomedical Engineering, vol. 53, no. 5, pp. 1409–1415, June 2006.

[19] B. Al-Sakere, F. André, C. Bernat, E. Connault, P. Opolon, R. V. Davalos, B. Rubinsky, and L. M. Mir. *Tumor Ablation with Irreversible Electroporation.* PLoS ONE, vol. 2, no. 11, p. e1135, November 2007.

[20] F. Wu, W.-Z. Chen, J. Bai, J.-Z. Zou, Z.-L. Wang, H. Zhu, and Z.-B. Wang. *Pathological Changes in Human Malignant Carcinoma Treated with High-Intensity Focused Ultrasound.* Ultrasound in Medicine and Biology, vol. 27, no. 8, pp. 1099–1106, August 2001.

[21] F. Wu, L. Zhou, and W. R. Chen. *Host Antitumour Immune Responses to HIFU Ablation.* International Journal of Hyperthermia, vol. 23, no. 2, pp. 165–171, March 2007.

[22] A. Gelet, J. Y. Chapelon, R. Bouviera, O. Rouviere, D. Lyonnet, and J. M. Dubernard. *Transrectal High Intensity Focused Ultrasound for the Treatment of Localized Prostate Cancer: Factors Influencing the Outcome.* European Urology, vol. 40, pp. 124–129, 2001.

[23] C. R. Hill, J. C. Bamber, and G. R. ter Haar. *Physical Principles of Medical Ultrasonics.* John Wiley and Sons, Bognor Regis, West Sussex, UK, 2004.

[24] R. S. C. Cobbold. *Foundations of Biomedical Ultrasound.* Oxford University Press, Oxford, Oxfordshire, UK, 2007.

[25] M. F. Insana and D. G. Brown. *Ultrasonic Scattering in Biological Tissues*, chap. Acoustic Scattering Theory Applied to Soft Biological Tissues, pp. 76–124. CRC Press, Boca Raton, FL, USA, 1993. Edited by K. K. Shung and G. A. Thieme.

[26] L. A. Frizzell, E. L. Cartensen, and J. F. Dyro. *Shear Properties of Mammalian Tissues at Low Megahertz Frequencies*. Journal of the Acoustical Society of America, vol. 60, no. 6, pp. 1409–1411, December 1976.

[27] X. Yang and C. C. Church. *A Model for the Dynamics of Gas Bubbles in Soft Tissue*. Journal of the Acoustical Society of America, vol. 118, no. 6, pp. 3595–3606, December 2005.

[28] J. F. Kelly and R. J. McGough. *Fractal Ladder Models and Power Law Wave Equations*. Journal of the Acoustical Society of America, vol. 126, no. 4, pp. 2072–2081, October 2009.

[29] L. B. Eldred, W. P. Baker, and A. N. Palazotto. *Kelvin-Voigt Versus Fractional Derivative Models as Constitutive Relations for Viscoelastic Materials*. American Institute of Aeronautics and Astronautics Journal, vol. 33, no. 3, pp. 547–550, March 1995.

[30] A. S. Dukhin and P. J. Goetz. *Bulk Viscosity and Compressibility Measurement Using Acoustic Spectroscopy*. Chemical Physics, vol. 130, no. 12, pp. 1–13, 2009.

[31] M. R. Gertner, B. C. Wilson, and M. D. Sherar. *Ultrasound Properties of Liver Tissue During Heating*. Ultrasound in Medicine and Biology, vol. 23, no. 9, pp. 1395–1403, 1997.

[32] R. Righetti, F. Kallel, R. J. Stafford, R. E. Price, T. A. Krouskop, J. D. Hazle, and J. Ophir. *Elastographic Characterization of HIFU-Induced Lesions in Canine Livers*. Ultrasound in Medicine and Biology, vol. 25, no. 7, pp. 1099–1113, 1999.

[33] M. Z. Kiss, M. J. Daniels, and T. Varghese. *Investigation of Temperature-Dependent Viscoelastic Properties of Thermal Lesions in ex Vivo Animal Liver Tissue*. Journal of Biomechanics, vol. 42, pp. 959–966, 2009.

[34] E. Sapin-de Brosses, J.-L. Gennisson, M. Pernot, M. Fink, and M. Tanter. *Temperature Dependence of the Shear Modulus of Soft Tissues Assessed by Ultrasound*. Physics in Medicine and Biology, vol. 55, pp. 1701–1718, 2010.

[35] P. M. Morse and K. U. Ingard. *Theoretical Acoustics*. Princeton University Press, Princeton, NJ, USA, 1987.

[36] T. G. Leighton. *The Acoustic Bubble*. Academic Press, Oxford, Oxfordshire, UK, 1997.

[37] W. Marczak. *Water as a Standard in The Measurements of Speed of Sound in Liquids*. Journal of the Acoustical Society of America, vol. 102, no. 5, pp. 2776–2779, November 1997.

[38] M. Tanter, M. Pernot, J.-F. Aubry, G. Montaldo, F. Marquet, and M. Fink. *Compensating for Bone Interfaces and Respiratory Motion in High-Intensity Focused Ultrasound.* International Journal of Hyperthermia, vol. 23, no. 2, pp. 141–151, 2007.

[39] W. L. Nyborg. *Heat Generation by Ultrasound in a Relaxing Medium.* Journal of the Acoustical Society of America, vol. 70, no. 2, pp. 310–312, August 1981.

[40] W. L. Nyborg. *Sonically Produced Heat in a Fluid with Bulk Viscosity and Shear Viscosity.* Journal of the Acoustical Society of America, vol. 80, no. 4, pp. 1133–1139, October 1986.

[41] M. F. Hamilton and D. T. Blackstock. *Nonlinear Acoustics: Theory and Applications.* Academic Press, Oxford, Oxfordshire, UK, 1997.

[42] J. N. Tjøtta and S. Tjøtta. *Nonlinear Equations of Acoustics, with Application to Parametric Acoustic Arrays.* Journal of the Acoustical Society of America, vol. 69, no. 6, pp. 1644–1652, June 1981.

[43] F. A. Duck. *Physical Properties of Tissue.* Academic Press, Oxford, Oxfordshire, UK, 1990.

[44] P. A. Narayana and J. Ophir. *On the Frequency Dependence of Attenuation in Normal and Fatty Liver.* IEEE Transactions on Sonics and Ultrasonics, vol. 30, no. 6, pp. 379–383, November 1983.

[45] T. G. Muir and E. L. Cartensen. *Prediction of Nonlinear Acoustic Effects at Biomedical Frequencies and Intensities.* Ultrasound in Medicine and Biology, vol. 6, pp. 345–357, 1980.

[46] A. A. Atchley. *Not Your Ordinary Sound Experience: A Nonlinear Acoustics Primer.* Acoustics Today, vol. 1, pp. 19–24, October 2005.

[47] E. A. Filonenko and V. A. Khokhlova. *Effect of Acoustic Nonlinearity on Heating of Biological Tissue by High-Intensity Focused Ultrasound.* Acoustical Physics, vol. 47, no. 4, pp. 468–475, 2001.

[48] V. A. Khokhlova, M. R. Bailey, J. A. Reed, B. W. Cunitz, P. J. Kaczkowski, and L. A. Crum. *Effects of Nonlinear Propagation, Cavitation, and Boiling in Lesion Formation by High Intensity Focused Ultrasound in a Gel Phantom.* Journal of the Acoustical Society of America, vol. 119, no. 3, pp. 1834–1848, March 2006.

[49] E. L. Cartensen, W. K. Law, N. D. McKay, and T. G. Muir. *Demonstration of Nonlinear Acoustical Effects at Biomedical Frequencies and Intensities.* Ultrasound in Medicine and Biology, vol. 6, pp. 359–368, 1980.

[50] E. Y. Knight, M. F. Hamilton, Y. A. Ilinskii, and E. A. Zabolotskaya. *On Rayleigh Wave Nonlinearity, and Analytical Approximation of the Shock Formation Distance.* Journal of the Acoustical Society of America, vol. 102, no. 5, pp. 2529–2535, November 1997.

[51] C. E. Brennen. *Cavitation and Bubble Dynamics*. Oxford University Press, Oxford, Oxfordshire, UK, February 1995.

[52] W. Lauterborn and T. Kurz. *Physics of Bubble Oscillations*. Reports on Progress in Physics, vol. 73, no. 10, pp. 1–88, September 2010.

[53] C.-C. Coussios, C. H. Farny, G. R. ter Haar, and R. A. Roy. *Role of Acoustic Cavitation in the Delivery and Monitoring of Cancer Treatment by High-Intensity Focused Ultrasound*. International Journal of Hyperthermia, vol. 23, no. 1, pp. 1–17, January 2007.

[54] L. A. Crum. *Nucleation and Stabilization of Microbubbles in Liquids*. Applied Scientific Research, vol. 38, pp. 101–115, 1982.

[55] C. C. Church. *Spontaneous Homogeneous Nucleation, Inertial Cavitation and the Safety of Diagnostic Ultrasound*. Ultrasound in Medicine and Biology, vol. 28, no. 10, pp. 1349–1364, 2002.

[56] A. A. Atchley and A. Prosperetti. *The Crevice Model of Bubble Nucleation*. Journal of the Acoustical Society of America, vol. 86, no. 3, pp. 1065–1084, September 1989.

[57] R. E. Apfel. *The Role of Impurities in Cavitation-Threshold Determination*. Journal of the Acoustical Society of America, vol. 48, no. 5, pp. 1179–1186, June 1970.

[58] F. G. Blake Jr. *Onset of Cavitation in Liquids*. PhD thesis, Harvard University, Cambridge, MA, USA, 1949.

[59] J. Frohly, S. Labouret, C. Bruneel, I. Looten-Baquet, and R. Torguet. *Ultrasonic Cavitation Monitoring by Acoustic Noise Power Measurement*. Journal of the Acoustical Society of America, vol. 108, no. 5, pp. 2012–2020, November 2000.

[60] R. E. Apfel and C. K. Holland. *Gauging the Likelihood of Cavitation from Short-Pulse, Low-Duty Cycle Diagnostic Ultrasound*. Ultrasound in Medicine and Biology, vol. 17, no. 2, pp. 179–185, 1991.

[61] R. E. Apfel. *Possibility of Microcavitation from Diagnostic Ultrasound*. IEEE Transactions on Ultrasonics, Ferroelectrics, and Frequency Control, vol. 33, no. 2, pp. 139–142, March 1986.

[62] T. G. Leighton. *Derivation of the Rayleigh-Plesset Equation in Terms of Volume*. Technical Report 308, Institute of Sound and Vibration Research, University of Southampton, Southampton, Hampshire, UK, January 2007.

[63] J. B. Keller and M. Miksis. *Bubble Oscillations of Large Amplitude*. Journal of the Acoustical Society of America, vol. 68, no. 2, pp. 628–633, August 1980.

[64] I. R. Webb, M. Arora, R. A. Roy, S. J. Payne, and C.-C. Coussios. *Dynamics of Gas Bubbles in Time-Variant Temperature Fields*. Journal of Fluid Mechanics, vol. 663, pp. 209–232, 2010.

[65] N. Hockham, C.-C. Coussios, and M. Arora. *A Real-Time Controller for Sustaining Thermally Relevant Acoustic Cavitation During Ultrasound Therapy.* IEEE Transactions on Ultrasonics, Ferroelectrics, and Frequency Control, vol. 57, no. 12, pp. 2685–2694, December 2010.

[66] V. Ilyichev, V. L. Koretz, and N. P. Melnikov. *Spectral Characteristics of Acoustic Cavitation.* Ultrasonics, vol. 27, pp. 357–361, 1989.

[67] P. Kennedy, M. Arora, and C.-C. Coussios. *Localization and Interpretation of Bubble Activity During HIFU Exposure.* In: E. S. Ebbini (editor), *Proceedings of the 8th International Symposium on Therapeutic Ultrasound*, vol. 1113, pp. 68–72. American Institute of Physics, 2009.

[68] Olympus NDT. *Ultrasonic Transducer Technical Notes.* World Wide Web (http://www.olympus-ims.com/en/knowledge), June 2011.

[69] H. T. O'Neil. *Theory of Focusing Radiators.* Journal of the Acoustical Society of America, vol. 21, no. 5, pp. 516–526, September 1949.

[70] C. M. Payne. *Principles of Naval Weapon Systems.* Naval Institute Press, Annapolis, MD, USA, 2006.

[71] S. N. Goldberg, C. J. Grassi, J. F. Cardella, J. W. Charboneau, G. D. Dodd III, D. E. Dupuy, D. Gervais, A. R. Gillams, R. A. Kane, F. T. Lee Jr., T. Livraghi, J. McGahan, D. A. Phillips, H. Rhim, and S. G. Silverman. *Image-Guided Tumor Ablation: Standardization of Terminology and Reporting Criteria.* J Vasc Interv Radiol, vol. 16, no. 6, pp. 765–778, June 2005.

[72] J. M. Berg, J. L. Tymoczko, and L. Stryer. *Biochemistry.* W. H. Freeman, New York, NY, USA, 2006.

[73] C. Tanford. *Protein Denaturation.* Advances in Protein Chemistry, vol. 23, pp. 121–282, 1968.

[74] F. Despa, D. P. Orgill, J. Neuwalder, and R. C. Lee. *The Relative Thermal Stability of Tissue Macromolecules and Cellular Structure in Burn Injury.* Burns, vol. 31, pp. 568–577, 2005.

[75] L.-S. Bouchard and M. J. Bronskill. *Magnetic Resonance Imaging of Thermal Coagulation Effects in a Phantom for Calibrating Thermal Therapy Devices.* Medical Physics, vol. 27, no. 5, pp. 1141–1145, May 2000.

[76] C. Lafon, P. J. Kaczkowski, S. Vaezy, M. Noble, and O. A. Sapozhnikov. *Development and Characterization of an Innovative Synthetic Tissue-Mimicking Material for High Intensity Focused Ultrasound (HIFU) Exposures.* In: *IEEE Ultrasonics Symposium*, pp. 1295–1298. IEEE, 2001.

[77] K. Takegami, Y. Kaneko, T. Watanbe, T. Maruyama, Y. Matsumoto, and H. Nagawa. *Polyacrylamide Gel Containing Egg White as a New Model for Irradiation Experiments Using Focused Ultrasound.* Ultrasound in Medicine and Biology, vol. 30, no. 10, pp. 1419–1422, 2004.

[78] M. Lazebnik, E. L. Madsen, G. R. Frank, and S. C. Hagness. *Tissue-Mimicking Phantom Materials for Narrowband and Ultrawideband Microwave Applications.* Physics in Medicine and Biology, vol. 50, pp. 4245–4258, 2005.

[79] C. Lafon, V. Zderic, M. L. Noble, J. C. Yuen, P. J. Kaczkowski, O. A. Sapozhnikov, F. Chavrier, L. A. Crum, and S. Vaezy. *Gel Phantom for use in High-Intensity Focused Ultrasound Dosimetry.* Ultrasound in Medicine and Biology, vol. 31, no. 10, pp. 1383–1389, 2005.

[80] Y. Liu and P. Zhong. *High Intensity Focused Ultrasound Induced Transgene Activation in a Cell-Embedded Tissue Mimicking Phantom.* In: *IEEE Ultrasonics Symposium*, pp. 1746–1749. IEEE, 2006.

[81] G. Speyer, P. Kaczkowski, A. Brayman, M. Andrew, S. G. Kargl, and L. A. Crum. *Quantitative Assessment of Thermal Dose Using Photographic Measurements of Tissue Discoloration.* Journal of the Acoustical Society of America, vol. 123, no. 5, p. 3223, May 2008.

[82] Y. Xiang, Y. Liu, and M. L. Lee. *Ultrahigh Pressure Liquid Chromatography Using Elevated Temperature.* Journal of Chromatography A, vol. 1104, no. 1–2, pp. 198–202, February 2006.

[83] J. L. R. Arrondo, A. Muga, J. Castresana, and F. M. Goni. *Quantitative Studies of the Structure of Proteins in Solution by Fourier-Transform Infrared Spectroscopy.* Progress in Biophysics and Molecular Biology, vol. 59, no. 1, pp. 23–56, 1993.

[84] B. Hildebrandt, P. Wust, O. Ahlers, A. Dieing, G. Sreenivasa, T. Kerner, R. Felix, and H. Riess. *The Cellular and Molecular Basis of Hyperthermia.* Critical Reviews in Oncology, Hematology, vol. 43, pp. 33–56, 2002.

[85] R. S. Cotran, V. Kumar, and S. L. Robbins. *Robbins Pathologic Basis of Disease.* W. B. Saunders Company, Philadelphia, PA, USA, 5th edition, 1994.

[86] H. H. Kampinga. *Thermotolerance in Mammalian Cells: Protein Denaturation and Aggregation, and Stress Proteins.* The Journal of Cell Biology, vol. 104, pp. 11–17, 1993.

[87] J. R. Lepock, H. E. Frey, and K. P. Ritchie. *Protein Denaturation in Intact Hepatocytes and Isolated Cellular Organelles During Heat Shock.* The Journal of Cell Biology, vol. 122, no. 6, pp. 1267–1276, September 1993.

[88] P. W. J. J. Burgman and A. W. T. Konings. *Heat Induced Protein Denaturation in the Particulate Fraction of HeLa S3 Cells: Effect of Thermotolerance.* Journal of Cellular Physiology, vol. 153, pp. 88–94, 1992.

[89] A. de Maio. *Heat Shock Proteins: Facts, Thoughts, and Dreams.* Shock, vol. 11, no. 1, pp. 1–12, 1999.

[90] M. N. Rylander, Y. Feng, J. Bass, and K. R. Diller. *Thermally Induced Injury and Heat-Shock Protein Expression in Cells and Tissues.* Annals of the New York Academy of Sciences, vol. 1066, pp. 222–242, 2005.

[91] J. W. Lichtman and J.-A. Conchello. *Fluorescence Microscopy.* Nature Methods, vol. 2, no. 12, pp. 910–919, December 2005.

[92] M. W. Dewhirst, B. L. Viglianti, M. Lora-Michiels, M. Hanson, and P. J. Hoopes. *Basic Principles of Thermal Dosimetry and Thermal Thresholds for Tissue Damage From Hyperthermia.* International Journal of Hyperthermia, vol. 19, no. 3, pp. 267–294, May 2003.

[93] W. C. Dewey. *Arrhenius Relationships from the Molecule and Cell to the Clinic.* International Journal of Hyperthermia, vol. 10, no. 4, pp. 457–483, 1994.

[94] S. A. Sapareto and W. C. Dewey. *Thermal Dose Determination in Cancer Therapy.* International Journal of Radiation Oncology, Biology, Physics, vol. 10, no. 6, pp. 787–800, 1984.

[95] F. J. Fry, G. Kossoff, R. C. Eggleton, and F. Funn. *Threshold Ultrasonic Dosages for Structural Changes in the Mammalian Brain.* Journal of the Acoustical Society of America, vol. 48, no. 6, pp. 1413–1417, 1970.

[96] T. C. Robinson and P. P. Lele. *An Analysis of Lesion Development in the Brain and in Plastics by High-Intensity Focused Ultrasound at Low-Megahertz Frequencies.* Journal of the Acoustical Society of America, vol. 51, no. 4, pp. 1333–1351, December 1972.

[97] R. M. Lerner, E. L. Cartensen, and F. Dunn. *Frequency Dependence of Thresholds for Ultrasonic Production of Thermal Lesions in Tissue.* Journal of the Acoustical Society of America, vol. 54, no. 2, pp. 504–506, 1973.

[98] F. Dunn, J. E. Lohnes, and F. J. Fry. *Frequency Dependence of Threshold Ultrasonic Dosages for Irreversible Structural Changes in Mammalian Brain.* Journal of the Acoustical Society of America, vol. 58, no. 2, pp. 512–514, August 1975.

[99] R. L. Johnston and F. Dunn. *Ultrasonic Absorbed Dose, Dose Rate, and Produced Lesion Volume.* Ultrasonics, vol. 14, no. 4, pp. 153–155, July 1976.

[100] E. W. Gerner. *Thermal Dose and Time-Temperature Factors for Biological Responses to Heat Shock.* International Journal of Hyperthermia, vol. 3, no. 4, pp. 319–327, 1987.

[101] W. C. Dewey, L. E. Hopwood, S. A. Sapareto, and L. E. Gerwick. *Cellular Responses to Combinations of Hyperthermia and Radiation.* Radiology, vol. 123, no. 2, pp. 463–474, 1977.

[102] C. C. Church. *Thermal Dose and the Probability of Adverse Effects from HIFU.* In: C.-C. Coussios and G. R. ter Haar (editors), *Proceedings of the 6th International Symposium on Therapeutic Ultrasound*, vol. 911, pp. 131–137. American Institute of Physics, 2006.

[103] M. Menzinger and R. Wolfgang. *The Meaning and Use of the Arrhenius Activation Energy.* Angewandte Chemie (International Edition), vol. 8, no. 6, pp. 438–444, 1969.

[104] F. L. Lizzi, D. J. Coleman, J. Driller, M. Ostromogilsky, S. Chang, and P. Greenall. *Ultrasonic Hyperthermia for Ophthalmic Therapy.* IEEE Transactions on Sonics and Ultrasonics, vol. 31, no. 5, pp. 473–481, 1984.

[105] B. E. Billard, K. Hynynen, and R. B. Roemer. *Effects of Physical Parameters on High Temperature Ultrasound Hyperthermia.* Ultrasound in Medicine and Biology, vol. 16, no. 4, pp. 409–420, 1990.

[106] C. A. Damianou, N. T. Sanghvi, F. J. Fry, and R. Maass-Moreno. *Dependence of Ultrasonic Attenuation and Absorption in Dog Soft Tissues on Temperature and Thermal Dose.* Journal of the Acoustical Society of America, vol. 102, no. 1, pp. 628–634, July 1997.

[107] H. Wan, J. Aarsvold, M. O'Donnell, and C. A. Cain. *Thermal Dose Optimization for Ultrasound Tissue Ablation.* IEEE Transactions on Ultrasonics, Ferroelectrics, and Frequency Control, vol. 46, no. 4, pp. 913–928, July 1999.

[108] K. Hynynen and N. J. McDannold. *MRI Guided and Monitored Focused Ultrasound Thermal Ablation Methods: A Review of Progress.* International Journal of Hyperthermia, vol. 20, no. 7, pp. 725–737, 2004.

[109] K.-S. Cheng and R. B. Roemer. *Closed-Form Solution for the Thermal Dose Delivered During Single Pulse Thermal Therapies.* International Journal of Hyperthermia, vol. 21, no. 3, pp. 215–230, 2005.

[110] C. Maleke and E. E. Konofagou. *Harmonic Motion Imaging for Focused Ultrasound (HMIFU): A Fully Integrated Technique for Sonication and Monitoring of Thermal Ablation in Tissues.* Physics in Medicine and Biology, vol. 53, pp. 1773–1793, 2008.

[111] M. C. Pilatou, E. A. Stewart, S. E. Maier, F. M. Fennessy, K. Hynynen, C. M. C. Tempany, and N. J. McDannold. *MRI-Based Thermal Dosimetry and Diffusion-Weighted Imaging of MRI-Guided Focused Ultrasound Thermal Ablation of Uterine Fibroids.* Journal of Magnetic Resonance Imaging, vol. 29, pp. 404–411, 2009.

[112] Y. Feng, J. T. Oden, and M. N. Rylander. *A Two-State Cell Damage Model Under Hyperthermic Conditions: Theory and In Vitro Experiments.* Journal of Biomechanical Engineering, vol. 130, pp. 1–10, August 2008.

[113] N. A. Moussa, E. N. Tell, and E. G. Cravalho. *Time Progression of Hemolysis of Erythrocyte Populations Exposed to Supraphysiological Temperatures.* Journal of Biomechanical Engineering, vol. 101, pp. 213–217, 1979.

[114] H. A. Jung. *A Generalized Concept for Cell Killing by Heat.* Radiation Research, vol. 106, pp. 56–72, 1986.

[115] J. R. Oleson, T. V. Samulski, K. A. Leopold, S. T. Clegg, M. W. Dewhirst, R. K. Dodge, and S. L. George. *Sensitivity of Hyperthermia Trial Outcomes to Temperature and Time: Implications for Thermal Goals of Treatment.* International Journal of Radiation Oncology, Biology, Physics, vol. 25, pp. 289–297, 1992.

[116] S. L. Jacques, C. Newman, and X.-Y. He. *Thermal Coagulation of Tissues: Liver Studies Indicate a Distribution of Rate Paramters, Not a Single Rate Parameter, Describes the Coagulation Process.* In: *Proceedings of the 1991 Annual Winter Meeting of the American Society of Mechanical Engineers*, pp. 71–73, Atlanta, GA, USA, 1991.

[117] M. S. Kang, C. W. Song, and S. H. Levitt. *Role of Vascular Function in Response of Tumors in Vivo to Hyperthermia.* Cancer Research, vol. 40, pp. 1130–1135, 1980.

[118] T.-Y. Wang, Z. Xu, F. Winterroth, T. L. Hall, J. B. Fowlkes, E. D. Rothman, W. W. Roberts, and C. A. Cain. *Quantitative Ultrasound Backscatter Feedback for Pulsed Cavitational Ultrasound Therapy—Histotripsy.* IEEE Transactions on Ultrasonics, Ferroelectrics, and Frequency Control, vol. 56, no. 5, pp. 995–1005, May 2009.

[119] S. B. Barnett, H.-D. Rott, G. R. ter Haar, M. C. Ziskin, and K. Maedaii. *The Sensitivity of Biological Tissue to Ultrasound.* Ultrasound in Medicine and Biology, vol. 23, no. 6, pp. 805–812, 1997.

[120] K. G. Baker, V. J. Robertson, and F. A. Duck. *A Review of Therapeutic Ultrasound: Biophysical Effects.* Physical Therapy, vol. 81, no. 7, pp. 1351–1358, July 2001.

[121] G. R. Harris, B. A. Herman, and M. R. Myers. *A Comparison of the Thermal Dose Equation and the Intensity-Time Product for Predicting Tissue Damage Thresholds.* Ultrasound in Medicine and Biology, vol. 37, no. 4, pp. 580–586, 2011.

[122] H. H. Pennes. *Analysis of Tissue and Arterial Blood Temperatures in the Resting Human Forearm.* Journal of Applied Physiology, vol. 1, no. 2, pp. 93–122, August 1948.

[123] J. W. Durkee Jr., P. P. Antich, and C. E. Lee. *Exact Solutions to the Multiregion Time-Dependent Bioheat Equation. I: Solution Development.* Physics in Medicine and Biology, vol. 35, no. 7, pp. 847–867, 1990.

[124] J. W. Durkee Jr., P. P. Antich, and C. E. Lee. *Exact Solutions to the Multiregion Time-Dependent Bioheat Equation. II: Numerical Evaluation of the Solutions.* Physics in Medicine and Biology, vol. 35, no. 7, pp. 869–889, 1990.

[125] C. R. Hill, I. Rivens, M. G. Vaughan, and G. R. ter Haar. *Lesion Development in Focused Ultrasound Surgery: A General Model.* Ultrasound in Medicine and Biology, vol. 20, no. 3, pp. 259–269, 1994.

[126] R. M. Arthur, W. L. Straube, J. W. Trobaugh, and E. G. Moros. *Noninvasive Estimation of Hyperthermia Temperatures with Ultrasound*. International Journal of Hyperthermia, vol. 21, no. 6, pp. 589–600, 2005.

[127] R. Maass-Moreno, C. A. Damianou, and N. T. Sanghvi. *Noninvasive Temperature Estimation in Tissue via Ultrasound Echo-Shifts. Part II. In Vitro Study*. Journal of the Acoustical Society of America, vol. 100, no. 4, pp. 2522–2530, October 1996.

[128] C. Simon, P. VanBaren, and E. S. Ebbini. *Two-Dimensional Temperature Estimation Using Diagnostic Ultrasound*. IEEE Transactions on Ultrasonics, Ferroelectrics and Frequency Control, vol. 45, no. 4, pp. 1088–1099, July 1998.

[129] R. Seip and E. S. Ebbini. *Noninvasive Estimation of Tissue Temperature Response to Heating Fields Using Diagnostic Ultrasound*. IEEE Transactions on Biomedical Engineering, vol. 42, no. 8, pp. 828–839, August 1995.

[130] D. Liu and E. S. Ebbini. *Real-Time 2-D Temperature Imaging Using Ultrasound*. IEEE Transactions on Biomedical Engineering, vol. 57, no. 1, pp. 12–16, January 2010.

[131] H. E. Cline, K. Hynynen, C. J. Hardy, R. D. Watkins, J. F. Schenck, and F. A. Jolesz. *MR Temperature Mapping of Focused Ultrasound Surgery*. Magnetic Resonance in Medicine, vol. 31, pp. 628–636, 1994.

[132] N. J. McDannold. *Quantitative MRI-Based Temperature Mapping Based on the Proton Resonant Frequency Shift: Review of Validation Studies*. International Journal of Hyperthermia, vol. 21, no. 6, pp. 533–546, September 2005.

[133] B. D. de Senneville, C. Mougenot, B. Quesson, I. Dragonu, N. Grenier, and C. T. W. Moonen. *MR Thermometry for Monitoring Tumor Ablation*. European Radiology, vol. 17, pp. 2401–2410, 2007.

[134] J. D. Bancroft, H. C. Cook, and R. W. Stirling. *Manual of Histological Techniques and Their Diagnostic Applications*. Churchill Livingstone, London, UK, 1994.

[135] T. Wu, J. P. Felmlee, J. F. Greenleaf, S. J. Riederer, and R. L. Ehman. *Assessment of Thermal Tissue Ablation with MR Elastography*. Magnetic Resonance in Medicine, vol. 45, pp. 80–87, 2001.

[136] M. G. Skinner, S. Everts, A. D. Reid, I. A. Vitkin, L. Lilge, and M. D. Sherar. *Changes in Optical Properties of ex Vivo Rat Prostate due to Heating*. Physics in Medicine and Biology, vol. 45, pp. 1375–1386, 2000.

[137] M. R. Gertner, A. E. Worthington, B. C. Wilson, and M. D. Sherar. *Ultrasound Imaging of Thermal Therapy in in Vitro Liver*. Ultrasound in Medicine and Biology, vol. 24, no. 7, pp. 1023–1032, 1998.

[138] B. A. Rabkin, V. Zderic, and S. Vaezy. *Hyperecho in Ultrasound Images of HIFU Therapy: Involvement of Cavitation*. Ultrasound in Medicine and Biology, vol. 31, no. 7, pp. 947–956, June 2005.

[139] B. A. Rabkin, V. Zderic, L. A. Crum, and S. Vaezy. *Biological and Physical Mechanisms of HIFU-Induced Hyperecho in Ultrasound Images.* Ultrasound in Medicine and Biology, vol. 32, no. 11, pp. 1721–1729, November 2006.

[140] N. T. Sanghvi, F. J. Fry, R. Bihrle, R. S. Foster, M. H. Phillips, J. Syrus, A. V. Zaitsev, and C. W. Hennige. *Noninvasive Surgery of Prostate Tissue by High-Intensity Focused Ultrasound.* IEEE Transactions on Ultrasonics, Ferroelectrics, and Frequency Control, vol. 43, no. 6, pp. 1099–1110, November 1996.

[141] C.-C. Coussios, C. R. Thomas, R. O. Cleveland, R. G. Holt, and R. A. Roy. *Cavitation Detection During and Following HIFU Exposure in Vitro.* Journal of the Acoustical Society of America, vol. 115, no. 5, p. 2448, May 2004.

[142] M. R. Bailey, L. N. Couret, O. A. Sapozhnikov, V. A. Khokhlova, G. R. ter Haar, S. Vaezy, X. Shi, R. Martin, and L. A. Crum. *Use of Overpressure to Assess the Role of Bubbles in Focused Ultrasound Lesion Shape in Vitro.* Ultrasound in Medicine and Biology, vol. 27, no. 5, pp. 695–708, May 2001.

[143] A. E. Worthington and M. D. Sherar. *Changes in Ultrasound Properties of Porcine Kidney Tissue During Heating.* Ultrasound in Medicine and Biology, vol. 27, no. 5, pp. 673–682, 2001.

[144] A. E. Worthington, J. Trachtenberg, and M. D. Sherar. *Changes in Ultrasound Properties of Human Prostate Tissue During Heating.* Ultrasound in Medicine and Biology, vol. 28, no. 10, pp. 1311–1318, 2002.

[145] K. F. Bing, V. M. Rotemberg, M. L. Palmeri, and K. R. Nightingale. *Concurrent ARFI Imaging and HIFU Ablation Using a Diagnostic Transducer Array and Ultrasound System with Custom Beam Sequences.* In: *Proceedings of the 2009 IEEE International Ultrasonics Symposium*, pp. 65–68, 2009.

[146] J. Vappou, C. Maleke, and E. E. Konofagou. *Quantitative Viscoelastic Parameters Measured by Harmonic Motion Imaging.* Physics in Medicine and Biology, vol. 54, pp. 3579–3594, 2009.

[147] S. Chen, M. Fatemi, and J. F. Greenleaf. *Quantifying Elasticity and Viscosity from Measurement of Shear Wave Speed Dispersion.* Journal of the Acoustical Society of America, vol. 115, no. 6, pp. 2781–2785, June 2004.

[148] J. Bercoff, M. Tanter, and M. Fink. *Supersonic Shear Imaging: A New Technique for Soft Tissue Elasticity Mapping.* IEEE Transactions on Ultrasonics, Ferroelectrics, and Frequency Control, vol. 51, no. 4, pp. 396–409, April 2004.

[149] M. Fink and M. Tanter. *Multiwave Imaging and Super Resolution.* Physics Today, vol. 63, no. 2, pp. 28–33, February 2010.

[150] Y.-J. Hu, Y. Liu, J.-B. Wang, X.-H. Xiao, and S.-S. Qu. *Study of the Interaction Between Monoammonium Glycyrrhizinate and Bovine Serum Albumin.* Journal of Pharmaceutical and Biomedical Analysis, vol. 36, pp. 915–919, 2004.

[151] G. L. Friedli. *Interactions of Deamidated Soluble Wheat Protein (SWP) with Other Food Proteins and Metals*. PhD thesis, University of Surrey, Guildford, Surrey, UK, 1996.

[152] F.-L. Cui, J. Fan, J.-P. Li, and Z.-D. Hua. *Interactions Between 1-benzoyl-4-p-chlorophenyl Thiosemicarbazide and Serum Albumin: Investigation by Fluorescence Spectroscopy*. Bioorganic and Medicinal Chemistry, vol. 12, no. 1, pp. 151–157, 2004.

[153] A. Barth and C. Zscherp. *What Vibrations Tell us About Proteins*. Quarterly Reviews of Biophysics, vol. 35, no. 4, pp. 369–430, 2002.

[154] K. Hirayama, S. Akashi, M. Furuya, and K.-I. Fukuhara. *Rapid Confirmation and Revision of the Primary Structure of Bovine Serum Albumin by ESIMS and FRIT-FAB LC/MS*. Biochemical and Biophysical Research Communications, vol. 173, no. 2, pp. 639–646, December 1990.

[155] V. J. C. Lin and J. L. Koenig. *Raman Studies of Bovine Serum Albumin*. Biopolymers, vol. 15, no. 1, pp. 203–218, 1976.

[156] J. N. de Wit and G. Klarenbeek. *Effects of Various Heat Treatments on Structure and Solubility of Whey Proteins*. Journal of Dairy Science, vol. 67, no. 11, pp. 2701–2710, 1984.

[157] Thermo Fisher Scientific. *Limburg an der Lahn, Hessen, Germany*. World Wide Web (http://www.thermofisher.com), June 2011.

[158] J. O. Smith III. *Mathematics of the Discrete Fourier Transform (DFT), with Audio Applications*. W3K Publishing, 2nd edition, April 2007.

[159] L. Ljung. *System Identification: Theory for the User*. Prentice-Hall, Upper Saddle River, NJ, USA, 2nd edition, 1999.

[160] M. Gyöngy and C.-C. Coussios. *Passive Spatial Mapping of Inertial Cavitation During HIFU Exposure*. IEEE Transactions on Biomedical Engineering, vol. 57, no. 1, pp. 48–56, January 2010.

[161] J. McLaughlan, I. Rivens, T. G. Leighton, and G. R. ter Haar. *A Study of Bubble Activity Generated in ex Vivo Tissue by High Intensity Focused Ultrasound*. Ultrasound in Medicine and Biology, vol. 36, no. 8, pp. 1327–1344, 2010.

[162] J. McLaughlan, I. Rivens, and G. R. ter Haar. *Cavitation Detection in ex Vivo Bovine Liver Tissue Exposed to High Intensity Focused Ultrasound (HIFU)*. In: *Proceedings of the 4th IEEE International Symposium on Biomedical Imaging*, pp. 1124–1127. IEEE, 2007.

[163] J. E. Browne, K. V. Ramnarine, A. J. Watson, and P. R. Hoskins. *Assessment of the Acoustic Properties of Common Tissue-Mimicking Test Phantoms*. Ultrasound in Medicine and Biology, vol. 29, no. 7, pp. 1053–1060, July 2003.

[164] K. Zell, J. I. Sperl, M. W. Vogel, R. Niessner, and C. Haisch. *Acoustical Properties of Selected Tissue Phantom Materials for Ultrasound Imaging.* Physics in Medicine and Biology, vol. 52, no. 20, pp. N475–N484, October 2007.

[165] U. Techavipoo, T. Varghese, Q. Chen, T. A. Stiles, J. A. Zagzebski, and G. R. Frank. *Temperature Dependence of Ultrasonic Propagation Speed and Attenuation in Excised Canine Liver Tissue Measured Using Transmitted and Reflected Pulses.* Journal of the Acoustical Society of America, vol. 115, no. 6, pp. 2859–2865, June 2004.

[166] K. J. Parker. *Ultrasonic Attenuation and Absorption in Liver Tissue.* Ultrasound in Medicine and Biology, vol. 9, no. 4, pp. 363–369, 1983.